UNIVERSIDADE FEDERAL DE SÃO CARLOS

CENTRO DE CIÊNCIAS EXATAS E DE TECNOLOGIA

PROGRAMA DE PÓS-GRADUAÇÃO EM CIÊNCIA

E ENGENHARIA DE MATERIAIS

UNIVERSITE GRENOBLE ALPES - ÉCOLE DOCTORALE DE INGENIERIE - MATERIAUX, MECANIQUE, ENVIRONNEMENT, ENERGETIQUE, PROCEDES, PRODUCTION (IMEP2)

STUDY OF BIOACTIVITY, CORROSION RESISTANCE AND FATIGUE BEHAVIOR OF Ti-12Mo-6Zr-2Fe ALLOY AFTER DIFFERENT SURFACE TREATMENTS

Cesar Adolfo Escobar Claros

São Carlos

2020

UNIVERSIDADE FEDERAL DE SÃO CARLOS

CENTRO DE CIÊNCIAS EXATAS E DE TECNOLOGIA

PROGRAMA DE PÓS-GRADUAÇÃO EM CIÊNCIA

E ENGENHARIA DE MATERIAIS

UNIVERSITE GRENOBLE ALPES - ÉCOLE DOCTORALE DE INGENIERIE - MATERIAUX, MECANIQUE, ENVIRONNEMENT, ENERGETIQUE, PROCEDES, PRODUCTION (IMEP2)

STUDY OF BIOACTIVITY, CORROSION RESISTANCE AND FATIGUE BEHAVIOR OF TI-12Mo-6Zr-2Fe ALLOY AFTER DIFFERENT SURFACE TREATMENTS

Cesar Adolfo Escobar Claros

Tese apresentada ao Programa de Pós-Graduação em Ciência e Engenharia de Materiais como requisito parcial à obtenção do título de DOUTOR EM CIÊNCIA E ENGENHARIA DE MATERIAIS

Orientador brasileiro: Prof. Dr. Claudemiro Bolfarini
Orientador francês: Prof. Dr. Jean-Claude Leprêtre
Coorientador brasileiro: Dr. Leonardo Contri Campanelli
Coorientador francês: Prof. Dr. Virginie Roche
Agência Financiadora: CNPq process:141952/2019-9;
CAPES- COFECUB: 88887.185801/2018-00

São Carlos

2020

UNIVERSIDADE FEDERAL DE SÃO CARLOS

Centro de Ciências Exatas e de Tecnologia
Programa de Pós-Graduação em Ciência e Engenharia de Materiais

Folha de Aprovação

Defesa de Tese de Doutorado do candidato Cesar Adolfo Escobar Claros, realizada em 19/11/2020.

Comissão Julgadora:

Prof. Dr. Claudemiro Bolfarini (UFSCar)

Prof. Dr. Alberto Moreira Jorge Junior (UFSCar)

Prof. Dr. Dilermando Nagle Travessa (UNIFESP)

Prof. Dr. Rubens Caram Júnior (UNICAMP)

Prof. Dr. Jean-Claude Leprêtre (Grenoble INP)

Profa. Dra. Virginie Roche (Grenoble INP)

Prof. Dr. Nicolas Mary (INSA Lyon)

O presente trabalho foi realizado com apoio da Coordenação de Aperfeiçoamento de Pessoal de Nível Superior - Brasil (CAPES) - Código de Financiamento 001.
O Relatório de Defesa assinado pelos membros da Comissão Julgadora encontra-se arquivado junto ao Programa de Pós-Graduação em Ciência e Engenharia de Materiais.

ACKNOWLEDGMENTS

I want to thank Professor Claudemiro Bolfarini for this opportunity, for all the trust he gave me and advice during all these years. I would also express my gratitude to my supervisors in France, Virginie Roche and Jean Claude Leprêtre for their valued help and productive discussions.

I want to express my special thanks to my co-advisor, Dr. Leonardo C. Campanelli, and professors Paulo Sérgio Pereira da Silva and Alberto Moreira Jorge Júnior, for guiding me, the technical discussions and everything taught.

I am grateful for the supports of the Brazilian National Council for Scientific and Technological Development (CNPq) (grant n° 141952/2019-9), French Committee for the Evaluation of Academic and Scientific Cooperation with Brazil (COFECUB) and CAPES (process n° 88887.137755/2017-00) for funding the bilateral cooperation, and to the CNPq universal project (n° 403955/2016-5).

This study was financed in part by the Coordenação de Aperfeiçoamento de Pessoal de Nível Superior - Brasil (CAPES) - Finance Code 001

To the Postgraduate Program in Materials Science and Engineering (PPGCEM) at the Federal University of São Carlos and the entire professor's Council, for the knowledge shared that contributed to my academic training.

Thanks to the Laboratory of Structural Characterization (LCE/DEMa/UFSCar), *Centro de Caracterização e Desenvolvimento de Materiais* (CCDM/UFSCar), and the *Consortium des Moyens Technologiques Communs* (CMTC/UGA) for allowing me to use their facilities.

I also want to thank all my colleagues from PPGCEM and LEPMI for their discussions, suggestions, and help during these doctoral years.

I would like to express my special thanks to my friends Kathe, Brenda, Tales, Rodriguinho, Vero, Chris, and many others for the coffee and tea sections, their motivation and support, and the time we shared together during these years.

Especialmente dedico esta conquista a mi familia, mi mamá, mi abuelo, mis hermanos y a Daniela, por estar siempre ahí apoyándome, por todo su amor, compresión, apoyo y motivarme día a día. Sin ustedes esto no sería posible.

A todos muchísimas gracias por contribuir en esta experiencia.

ABSTRACT

Demand for new implants with improved bioactivity, corrosion resistance, and optimal mechanical properties has been increasing considerably. In this sense, different surface treatments are applied in titanium alloys to improve their osteointegration process. Nevertheless, the developments of new bioactive surfaces could cause a considerable reduction in fatigue and corrosion strength leading to catastrophic failures in clinical use. For these reasons, this work studied the biocompatibility, corrosion and fatigue performance of Ti-12Mo-6Zr-2Fe alloy treated with three different surface modifications, namely, chemical surface treatment (CST), nanotubes (Nt) and nanopores (NP). Samples were immersed in simulated body fluid (SBF) solution during different periods, 0, 1, 7, and 14 days. After 14 days immersed in SBF, samples with CST showed high hydroxyapatite (HAp) formation; Likewise, samples with Nt and NP exhibited lower and moderated HAP formation, respectively. In samples without surface treatment was not observed HAp formation. The electrochemical behavior was studied through polarization curves and electrochemical impedance spectroscopy (EIS). Samples with Nt and NP displayed higher corrosion resistance and lower passivation current (I_{pass}) compared with untreated samples, after 14 days of immersion in SBF; samples with CST showed the worst corrosion performance for all the surface conditions studied. Furthermore, within the framework of electrochemical investigations, EIS results of Nt and NP samples showed a characteristic behavior that could not be modeled by traditional equivalent circuits. Thus, it was proposed a two-channel transmission line model for analyzing this impedance results, leading to a successful fitting of the EIS data. Finally, was observed a reduction of the fatigue resistance in the samples treated with NP and CST, associated with hydrogen embrittlement processes, due to the pick-up of hydrogen during the respective surface treatments.

Keywords: Titanium alloy; Bioactivity; Corrosion resistance; Fatigue behavior; Hydrogen embrittlement.

1.1

RESUMO

ESTUDO DE BIOATIVIDADE, RESISTÊNCIA À CORROSÃO E COMPORTAMENTO EM FADIGA DA LIGA TI-12Mo-6Zr-2Fe APÓS DIFERENTES TRATAMENTOS DE SUPERFÍCIE

A demanda por novos implantes com melhor bioatividade, resistência à corrosão e ótimas propriedades mecânicas têm aumentado consideravelmente. Nesse sentido, diferentes tratamentos de superfície são aplicados em ligas de titânio para melhorar seu processo de osseointegração. No entanto, o desenvolvimento de novas superfícies bioativas pode causar uma redução considerável na fadiga e na resistência à corrosão, levando a falhas catastróficas no uso clínico. Por esses motivos, este trabalho estudou o desempenho em biocompatibilidade, corrosão e fadiga da liga Ti-12Mo-6Zr-2Fe tratada com três diferentes modificações de superfície, a saber: tratamento químico da superfície (CST), nanotubos (Nt) e nanoporos (NP). As amostras foram imersas em uma solução que simula o fluido corporal (SBF) durante diferentes períodos, 0, 1, 7 e 14 dias. Após 14 dias imersos em SBF, não foi observada formação de HAp nas amostras sem tratamento de superfície, porém amostras com CST mostraram alta formação de hidroxiapatita (HAp). Da mesma forma, amostras com Nt e NP exibiram baixa e moderada formação de HAp, respectivamente. O comportamento eletroquímico foi estudado através de curvas de polarização e espectroscopia de impedância eletroquímica (EIS). Amostras com Nt e NP apresentaram maior resistência à corrosão e menor corrente de passivação (I_{pass}) em comparação com amostras não tratadas, após 14 dias de imersão no SBF; amostras com CST apresentaram o pior desempenho à corrosão de todas as condições de superfície estudadas. Além disso, no âmbito de investigações eletroquímicas, os resultados de EIS das amostras de Nt e NP mostraram um comportamento característico que não foi possível modelar pelos circuitos equivalentes tradicionais. Assim, foi proposto um modelo de linha de transmissão de dois canais para analisar esses resultados de impedância, levando a um ajuste bem-sucedido dos dados de EIS. Por fim, observou-se uma redução da resistência à fadiga nas amostras tratadas com NP e CST, associadas aos processos de fragilização por hidrogênio, devido à captação de hidrogênio durante os respectivos tratamentos de superfície.

Palavras-chave: Liga de titânio; Bioatividade, Resistência à corrosão; Comportamento em fadiga; Fragilização por hidrogênio.

RÉSUMÉ

ÉTUDE DE BIOACTIVITÉ, RÉSISTANCE A LA CORROSION ET COMPORTEMENT EN FATIGUE DE L'ALLIAGE Ti-12Mo-6Zr-2Fe APRÈS DIFFÉRENTS TRAITEMENTS DE SURFACE

La demande de nouveaux implants avec une meilleure bioactivité, résistance à la corrosion et des propriétés mécaniques optimisées a augmenté considérablement. Différents traitements de surface sont appliqués sur des alliages de titane pour améliorer leur processus d'ostéo-intégration. Néanmoins, le développement de nouvelles surfaces bioactives pourrait causer une réduction considérable de la résistance à la fatigue et à la corrosion, ce qui peut entraîner des défaillances catastrophiques dans leurs utilisations cliniques. Ainsi, dans ce travail, la performance en biocompatibilité, en fatigue et en corrosion de l'alliage de Ti-12Mo-6Zr-2Fe (TMZF) a été étudié. Cet alliage a été soumis à trois modifications de surface différentes, à savoir le traitement chimique de surface (CST, en anglais, pour *Chemical Surface Treatment*), les nanotubes (Nt) et les nanopores (NP). Les échantillons ont été immergés dans une solution physiologique appelée SBF (en anglais, pour *Simulated Body Fluid*) avec des durées d'immersion différentes : 0, 1, 7, et 14 jours. Après 14 jours d'immersion dans SBF, les échantillons qui ont subi un traitement chimique de surface ont montré une formation importante d'hydroxyapatite (HAp), nécessaire pour assurer une bonne osseo-intégration de l'implant. De même, les échantillons avec des nanotubes et nanopores montrent une formation, respectivement, faible et modérée de HAp. Dans les échantillons sans traitement de surface, la formation de HAp n'a pas été observée. Le comportement électrochimique a été étudié par des courbes de polarisation et par spectroscopie d'impédance électrochimique (SIE, ou EIS en anglais, pour *Electrochemical Impedance Spectroscopy*). Les échantillons avec Nt et NP manifestent une meilleure résistance à la corrosion et un domaine de passivité (I_{pass}) plus faible, en comparaison avec les échantillons non traités après 14 jours d'immersion dans SBF. Les échantillons qui ont subi un traitement chimique de surface (CST) ont démontré une résistance à la corrosion faible par rapport aux autres surfaces étudiées. Par ailleurs, dans le contexte des investigations électrochimiques, les résultats de SIE d'échantillons NT et NP ont montré un comportement caractéristique qui ne pouvait pas être modélisé par les circuits équivalents traditionnels. Ainsi, un modèle de ligne de transmission de deux canaux a été proposé pour analyser ces résultats d'impédance, permettant un ajustement réussi des données de SIE. Finalement, une réduction de la résistance à la fatigue a été observée dans les échantillons traités avec NP et CST, via une fragilisation par l'hydrogène, en raison du captage d'hydrogène pendant les traitements de surface.

Mots clés: Alliage de titane; bioactivité; résistance à la corrosion; comportement à la fatigue; fragilisation par l'hydrogène.

x

PUBLICATIONS

- L.C. Campanelli, C. A. Escobar Claros, B. J.M. Freitas, D. Aparecida, P. Reis, A. Moreira, J. Jr, C. Bolfarini, Effect of hydrogen pick-up on the fatigue behavior of the b -type Ti-12Mo-6Zr-2Fe alloy with x -nanoprecipitation, Mater. Lett. 282 (2021) 128740. https://doi.org/10.1016/j.matlet.2020.128740.
- P.S.C.P. da Silva, L.C. Campanelli, C.A. Escobar Claros, T. Ferreira, D.P. Oliveira, C. Bolfarini, Prediction of the surface finishing roughness effect on the fatigue resistance of Ti-6Al-4V ELI for implants applications, Int. J. Fatigue. 103 (2017) 258–263. https://doi.org/10.1016/j.ijfatigue.2017.06.007.

TABLE OF CONTENTS

LIST OF TABLES

LIST OF FIGURES

LIST OF ABBREVIATIONS

ASTM	American Standard for Testing of Materials
C_{dl}	Double layer capacitance
CPE	Constant-Phase-Element
CST	Chemical surface treatment with HCl etching and NaOH alkaline solution
E_{corr}	Corrosion potential
EDS	Energy dispersive spectroscopy
EEC	Electrical equivalent circuit
EIS	Electrochemical impedance spectroscopy
H_3PO_4	Phosphoric acid
Hap	Hydroxyapatite
HCl	Hydrochloric acid
HE	Hydrogen Embrittlement
I_{pass}	Passivation current density
NaOH	Sodium hydroxide
NP	Nanopores
Nt	Nanotubes
OCP	Open circuit potential
Q	Pseudocapacitance ($\Omega s^{-\alpha}.cm^2$)
R_{ct}	Charge transfer resistance
R_e	Electrolyte resistance or Ohmic resistance ($\Omega \cdot cm^{-2}$)
R_p	Polarization resistance
SBF	Solution body fluid
SCE	Saturated calomel electrode
SEM	Scanning electron microscopy
TEM	Transmission electron microscopy
TMZF	Ti-12Mo-6Zr-2Fe, titanium alloy
TL	Transmission line
W	Warburg element
X_1	Impedance distributed in the liquid phase of the transmission line ($\Omega \cdot cm^{-1}$)
X_2	Impedance distributed in the solid phase of the transmission line ($\Omega \cdot cm^{-1}$)
XRD	X-ray diffraction
ZA	Boundary impedance at the interface electrolyte | top of the pores (Ω)
$Z_{A,B}$	Impedances of the boundary conditions of the transmission line

ZB	Boundary impedance at the interface electrolyte | substrate (Ω)
|Z|	Impedance modulus
α, n, d	CPE exponent
α_{eff}	Effective CPE exponent
β	body centered cubic phase of titanium
ξ	Interfacial impedance of the transmission line (Ω·cm)

1 INTRODUCTION

Metallic alloys for orthopedic implants have to show four essential characteristics: a) low stress-shielding effect, due to the elastic modulus incompatibility between bone and implant; b) biocompatibility avoiding toxic-elements; c) excellent fatigue performance for cyclically stressed implants, and d) high corrosion resistance [1].

Due to the presence of elements as Al and V, considered as cytotoxic and the high elastic modulus of the Ti–6Al–4V-ELI, (~110 GPa), new titanium alloys with no toxic elements and lower elastic modulus have been investigated. Metastable β-titanium alloys like Ti-12Mo-6Zr-2Fe alloy (TMZF) show high mechanical strength and lower elastic modulus than the Ti–6Al–4V-ELI [2].

Metallic materials as titanium and its alloys, stainless steel and cobalt-chromium alloys, are used under load-bearing conditions. However, the direct contact metal-bone does not imply the formation of a strong bond between them. Thus, it is necessary to develop more bioactive surfaces over these metals [3].

Some surface treatments are applied on titanium alloys to improve their osteointegration process. Previous studies have demonstrated that HCl etching plus NaOH treatment can be an effective way to develop nanometric features on the surface of Ti–6Al–4V-ELI (ELI for Extra Low Interstitial content) samples unchanging its static and cyclic mechanical properties [4].

An alternative to CST is the anodizing process; this procedure is widely used on pure titanium, creating TiO_2 nanotubes on the surface, maximizing the specific surface area of the material and obtaining better biocompatibility [5].

An indicator of the bone formation ability on metallic implants is the nucleation and growth of a hydroxyapatite (HAp) layer. This capacity can be measured through the specimen immersion in a simulated body fluid (SBF), whose ion concentrations nearly equal to those of human blood plasma [3, 6].

Thus, the main objective of this project is studying the biocompatibility and corrosion performance of Ti-12Mo-6Zr-2Fe samples with nanotubes, nanopores and chemical surface treatment (CST) immersed during various periods in SBF, as well as the fatigue resistance variation of these different surface conditions.

2 STATE OF THE ART

2.1 Metallic biomaterials

The first reports of titanium date from 1791 in England, when the amateur mineralogist William Gregor was able to remove iron from the "ilmenite" mineral consisting of iron, oxygen, and titanium (FeTiO3), and the remaining titanium oxide was called "Mechanite" , in reference to the place where it was found [7]. Then the chemist Martin Heinrich Klaproth isolated the metal from its oxide, naming it "Titanium" because of the difficulty of extracting it, associating it with the powerful titans of Greek mythology. And between 1937-1940, chemist Wilhelm Justin Kroll was able to optimize the industrial method of obtaining titanium, being the process hereinafter known as the "Kroll process"; this method is still the most used nowadays [8, 9].

The strong titanium affinity for oxygen makes it one of the most corrosion-resistant structural metals due to the thermodynamic stability of a protective oxide layer formed promptly in different harsh environments, especially in aqueous acid environments [9]. Due to its high resistance to density ratio, titanium is widely used in the aeronautical, chemical and biomaterials industries [10].

In the 1940s titanium and its alloys emerged commercially, developed for aerospace applications; However, in 1963 they began to be used as biomaterials due to the excellent combination of properties desired for this purpose. Branemark et al. (1964), were the first to successfully evaluate the phenomenon of human bone developing on the surface of titanium, a process they called osseointegration [11].

According to the World Health Organization, 30% of people aged 65-74 have no natural teeth, so titanium dental implants are a viable solution for replacing missing teeth [12]. Additionally, the number of total hip or knee arthroplasties has been increasing considerably, approximately 800,000 procedures are performed per year in the United States [13, 14]. It is estimated that by the year 2030 the increase in these procedures will be approximately 673% for total knee arthroplasty and 174% for total hip arthroplasty. Thus, the demand for new long-term implants is being required and the study of problems and defects arising from surface modifications may be effective to contribute to the knowledge and improvement of mechanical behavior of these materials which may favor the performance and reduce the risk of failure of these components [13, 14].

Orthopedic implants can be categorized into two main groups, temporary implants for fracture fixation and joint implants. The first group plays a structural role in a fractured bone segment until it consolidates, and can be surgically removed after the end of the process. The second group demands additional mechanical properties because the implant is subjected to cyclic stresses arising from human body movement and the transmission of loads, such as dental, hip, knee implants, etc. [15, 16], see examples in Figure 2.1. This work focuses on this second group.

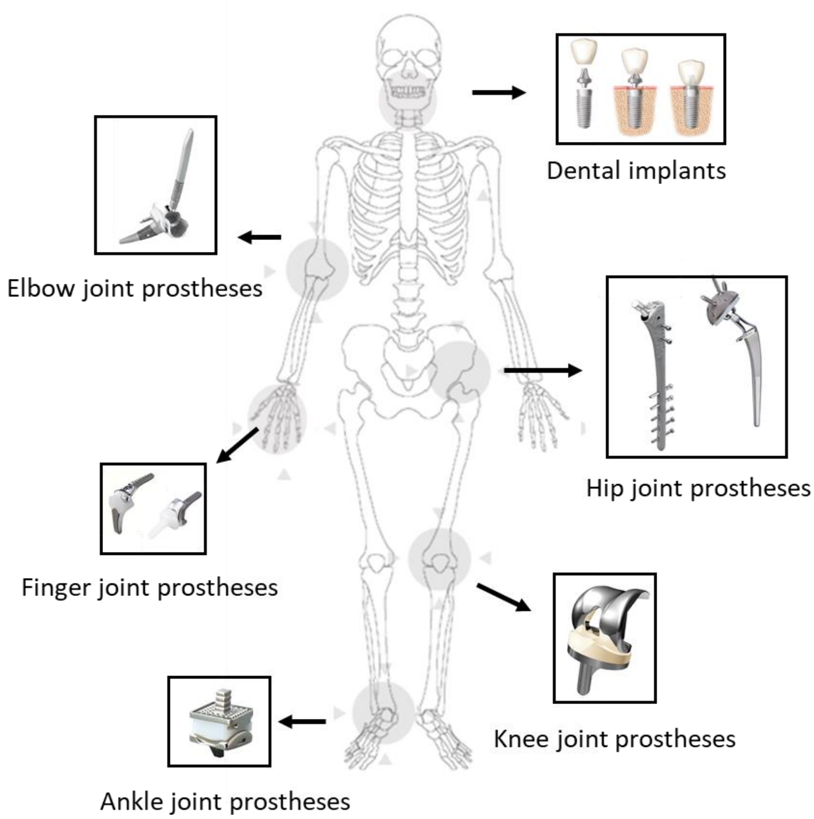

Figure 2.1 Metallic biomaterials for orthopedic and dental applications (provided by Nakashima Medical Co. Ltd Japan and Japan Medical Materials (JMM) Co.) [17].

2.2 Titanium alloys

Orthopedic implants require high mechanical properties, biocompatibility and osseointegration, high corrosion resistance, relatively low elastic modulus and high fatigue strength [14]. Titanium and its alloys have a high ability to become integrated with the bone. This property significantly improves the long-term behavior of implanted devices, reducing the risks of loosening and failure [18].

Titanium represents approximately 0.6% of the earth's crust, being the fourth most abundant structural metal, behind only aluminum, iron and magnesium [19]. Pure titanium exhibits allotropic phase transformation at 882 °C, moving from a high-temperature body centered cubic structure (β) to a compact hexagonal (α) at low temperatures (Figure 2.1). Conventionally commercial titanium alloys are classified into three categories, α, α + β and β alloys, according to the type and content of alloying elements. Substitutional elements such as Al, Sn, Ga, Zr and interstitial elements such as C, O and N dissolved in the titanium matrix are recognized as α stabilizers. Alloying elements, which decrease the phase transformation temperature, are known as β stabilizers. Generally stabilizing β elements are transition metals such as Mo, V, Ta, Fe, Mn, Cr, Ni and Nb. Additionally, some elements such as Zr, Hf and Sn behave neutrally, increasing or decreasing the transformation temperature α/β, depending on their concentrations [20–22].

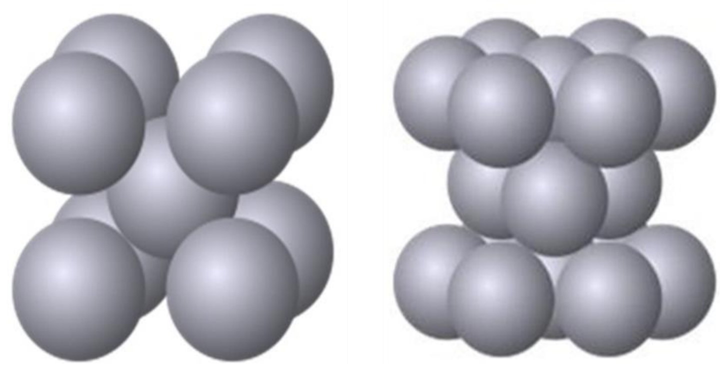

(a) **(b)**

Figure 2.1 Schematic illustration of the crystal structure of the major Titanium alloys for implants. a) Center-body cubed (α-Ti) and b) Compact hexagonal β-Ti.

2.2.1 Ti-12Mo-6Zr-2Fe

Some studies have indicated that aluminum and vanadium present in the most widely used Ti-6Al-4V alloy may be harmful to human health. Thus, there was a need to develop titanium alloys free of these elements with a desirable lower modulus of elasticity. In the mid-1950s the Ti-15Mo alloy was developed, in 1969 *Crucible* developed the Ti-11.5Mo-6Zr-4.5Sn (Beta III) alloy, which has similar phase transformations as the Ti-15Mo alloy. Finally, in the nineties *Howmedica* added iron to increase resistance to beta III alloy, thereby resulting in the Ti-12Mo-6Zr-2Fe alloy [7, 23].

Ti-12Mo-6Zr-2Fe alloy, also known as TMZF, has excellent mechanical properties among metastable β alloys. According to ASTM F1813, the microstructure of this alloy, in order to be used as a biomaterial, must have a recrystallized β phase, and the appearance of phases α and α´ is not allowed in a 100X magnification [24]. This provides an alloy with higher yield strength and better ductility than Ti-6Al-4V alloy, and a relatively low modulus of elasticity, lying in the range 74-85 GPa [25].

There are no surgical implant materials completely free of adverse reactions in the human body. However, the TMZF alloy has been tested “in vivo” in animals and has been used clinically for more than two decades. The results of these studies indicated a well-characterized level of local biological response that is equal to or less than that produced by the pure titanium used as reference material [24].

2.3 Fixation method

The fixation of the implant in the bone is very important and influences its useful life time. It can be of cemented or non-cemented type, in the first case there is cementation of the implant in the bone using a polymethyl methacrylate (PMMA) resin; in the second fixation method, a porous, bioactive surface is produced on the implant surface within which bone can grow [26].

Cemented implants are commonly used in elderly patients who do not have sufficient bone regeneration capacity to fix the implant through osseointegration. During use, small regions may lose adhesion without necessarily interfering with implant stability, in addition to the generation of PMMA and metallic debris that may result in adverse and inflammatory reactions [3].

The use of cementless prostheses increased in the 1980s due to its application in younger patients with a higher bone regeneration capacity. Currently, younger and more active patients requiring replacement surgery are treated with cementless prostheses [26]. This is because they have an adequate structure and surface composition to produce a durable mechanical anchor with the bone.

2.3.1 Surface modification of medical implants

Surface modifications are employed in metallic biomaterials to improve biological and mechanical compatibility to receive hard/soft tissues, resulting in the promotion of osseointegration; however, this should happens without impairing wear, corrosion, and fatigue resistance [26].

A schematic illustration of the regions formed at the titanium/bone interface is shown in Figure 2.2. From the left side of the figure, towards the right side, five distinct regions are highlighted. The first refers to the metallic titanium (region 1) covered by a layer of oxide (TiO2) forming region 2. This, in turn, after interaction with hydroxyl groups of water, forms a material with a gel consistency (region 3). At this stage, proteins present in body fluids adhere to the Ti-Gel layer (region 4) and the process continues by the adhesion of osteoblastic cells (region 5) towards the bone formation and osseointegration [27].

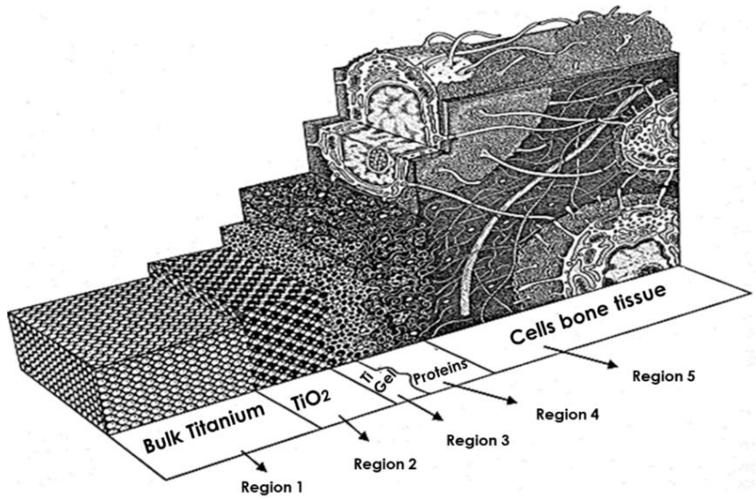

Figure 2.2 An artist's view of the titanium/tissue interface divided into five regions. The oxide of titanium is covered with a very thin layer of titanium peroxy compounds, which are in contact with the living bone (Adapted from [28]).

2.3.2 Chemical surface modification by acid etching and alkaline treatment

Several chemical modification methods make the implant surface more favorable for cell growth and adhesion. An example of chemical modification follows the principle of obtaining roughness through an acid attack with a subsequent alkaline treatment that generates a chemically biocompatible layer.

2.3.2.1 Acid etching

Acid attacks on titanium-based alloys are employed to remove oxidation and surface contaminants as a result of previously performed processing steps. Due to the reoxidation process that occurs, the acid attack also alters the roughness, surface composition and wettability [29].

The dual acid etching procedure, commonly described in the literature, consists of immersing the metal in a mixture of concentrated HCl and H_2SO_4 for a certain time at a temperature of 100ºC [30]. These studies suggest that there is greater apposition of osteogenic cells, when increasing the surface roughness of the material, also increasing the bone/implant contact. This type of surface promotes rapid osseointegration by improving osteoconductivity processes, resulting in bone formation directly on the implant surface favored by the topography generated on the titanium surface [3].

2.3.2.2 Alkaline treatment

Alkaline treatment imprints changes in chemical composition, roughness and topography on the treated surface by forming a layer of sodium titanate (in the case of titanium); this procedure makes materials bioactive , favoring, stimulating or catalyzing hydroxyapatite precipitation (Figure 2.3) [31, 32].

The passive oxide film spontaneously formed on the titanium metal initially suffers a degradation reaction during the acid etching, as follows:

$$TiO_2 + 4HCl \rightarrow TiCl_4 + 2H_2O \quad (2.1)$$

Simultaneously, titanium reacts with HCl:

$$2Ti + 6HCl \rightarrow 2TiCl_3 + 3H_2 \uparrow \quad (2.2)$$

$$Ti + H_2 \rightarrow TiH_2 \quad (2.3)$$

On the TiH_2 intermediate layer, a new passive oxide layer is formed and subsequently reacts with the NaOH solution. At first, the passive layer is partially dissolved to form $HTiO_3^-$:

$$TiO_2 + OH^- \rightarrow HTiO_3{}^- \quad (2.4)$$

At the same time, the metallic titanium is hydrated forming $HTiO_3^- \cdot nH_2O$:

$$Ti + 3OH^- \rightarrow Ti(OH)_3{}^+ + 4e^- \quad (2.5)$$

$$Ti(OH)_3^+ + e^- \rightarrow TiO_2 \,.\, H_2O + 0.5\, H_2 \uparrow \quad (2.6)$$

$$Ti(OH)_3^+ + OH^- \leftrightarrow Ti(OH)_4 \quad (2.7)$$

$$TiO_2.nH_2O + OH^- \leftrightarrow HTiO_3{}^- .nH_2O \quad (2.8)$$

Finally, positively charged alkali ions (Na+) react with negatively charged groups, to produce an alkali titanate hydrogel layer. Then, the samples treated in the alkaline medium can be immersed in a solution known as simulated body fluid (SBF), where apatite precipitation is stimulated (Figure 2.3) [3, 33].

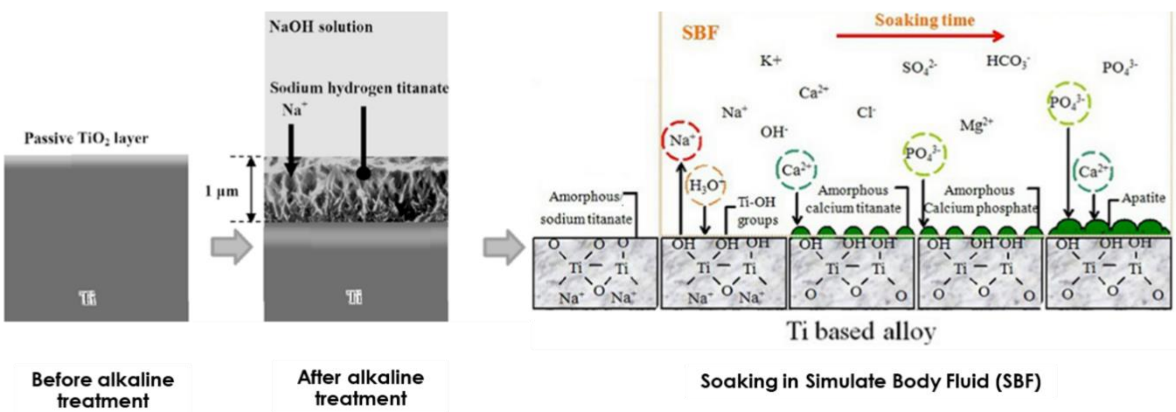

Figure 2.3 Schematic representation of the structural change in the surface of the metallic Titanium after the alkaline process and subsequent apatite formation on the treated surface (Adapted from ref. [3]).

In some cases, these attacks (acid etching and alkaline treatment) may cause a decrease in mechanical properties, especially its ductility and resistance to fatigue. Probably, due to surface irregularities that tend to be crack nucleation sites, besides the possible embrittlement caused by the absorption of hydrogen [34]. Therefore, another interesting surface modification could be the electrochemical anodization, in order to improve the biological, electrochemical and mechanical properties of the TMZF alloy avoiding hydrogen embrittlement.

2.3.3 Anodization process

Special attention has been paid over the last decades to the formation of TiO_2 nanotubes or nanopores, in particular by anodizing pure titanium. This method is a promising alternative to the deposition of hydroxyapatite, in particular because it allows to grow, simply, quickly, and at low cost, a layer of TiO_2 bioactive, directly connected to the titanium substrate, and therefore very adherent [14,15].

The presence of nanotubes on titanium surfaces changes the structural properties of the bulk titanium substrate, becoming a more attractive material for tissue engineering applications because of the higher porosity and increased surface area, improved cell attachment and tissue ingrowth, and therefore osseointegration. Figure 2.4 shows human osteoblast cell attachment on blank titanium and TiO_2 nanotubes after seven days of culture [35].

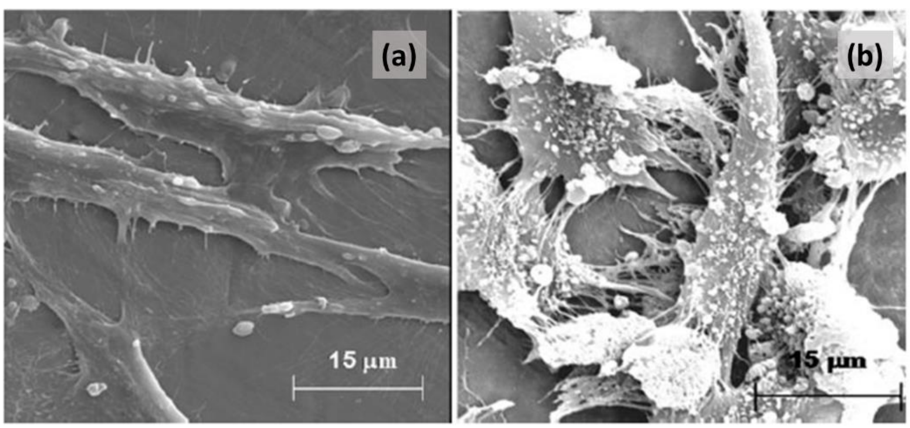

Figure 2.4 Human osteoblast cell attachment and proliferation on a) titanium and b) titanium with TiO_2 nanotubes [30].

Table 2.1 summarizes the anodization conditions, characteristics and cell response of TiO_2 nanotubes on titanium investigated by different research groups to date. It is possible to observe the diverse anodization processes and the different nanotubes characteristics obtained; the morphologic characteristics as diameter and lengths of the nanotubes could influence the cell response and therefore their osseointegration.

Nanotube diameter had a critical impact on cell response. Some studies claimed that 15 nm is the maximum permissible diameter prior to cell apoptosis for mesenchymal stem cells [31,32]. Nevertheless, reports also indicated nanotubes with diameters exceeding 100 nm favoring cell proliferation in case of osteoblast cells [36]. Thus, these contradictory results suggest that the interaction mechanism between cells and anodized surfaces is not yet clearly understood.

Table 2.1 Anodization parameters and cell response of Ti-based metallic implants

Material	Synthesis conditions of NTs			NTs dimensions		Cell response	Ref.
	Electrolyte	Applied Voltage (V)	Anodization Time (min)	Diameter (nm)	Length (nm)		
Ti	HF	20	60	70	250	Osteoblasts showed adhesion on TiO_2 Nt.	[37]
Ti	H_3PO_4+HF	1 - 20		10 - 15	600	Excellent biocompatibility for mesenchymal stem cells on 15 nm TiO_2 Nt, compared to cell apoptosis on 100 nm Nt.	[38]
Ti	H_3PO_4+HF	1 - 20	60	15 - 100		Osteoblast and osteoclast apoptosis when cultured on TiO_2 Nt of diameter 15 nm.	[39]
Ti	Acetic acid/HF	5 - 20	30	30 - 100		Human mesenchymal stem cell adhesion on Nt of both 30 and 100 nm diameter, with more cell proliferation, and migration, but also osteogenic differentiation on 30 nm Nt.	[40]
Ti	NH_4F + Ethylene glycol	30	180	100	4000	Osteoblast-like cells demonstrated high viability on Nt.	[41]
Ti	NH_4F + Ethylene Glycol/Glycerol	10-20	120	45 -130	360-4500	Crystallized and higher diameter NTs lead to better cellular activity than amorphous and/or smaller Nt.	[36]

2.3.3.1 Mechanisms of surface anodization

In the initial phase of the anodization process, when the titanium surface is exposed to sufficiently anodic voltage in an electrochemical configuration, an oxidation reaction occurs forming a compact oxide layer (Equations 2.9 – 2.12). These reactions are known as a field-assisted oxidation process and are the first step of the anodization process. At the anode oxidation of the metal takes place, which releases Ti^{4+} ions and electrons [42]:

$$Ti \rightarrow Ti^{4+} + 4e^{-} \tag{2.9}$$

$$Ti^{4+} + OH^{-} \rightarrow Ti(OH)_4 \tag{2.10}$$

$$Ti^{4+} + 2O^{2-} \rightarrow TiO_2 \tag{2.11}$$

$$Ti(OH)_4 \rightarrow TiO_2 + 2H_2O \tag{2.12}$$

Simultaneously, hydrogen evolution will take place at the cathode:

$$4H^{4+} + 4e^{-} \rightarrow 2H_2 \tag{2.13}$$

In the overall process the oxidized metal can be dissolved in the electrolyte or else form an oxide, according to equation [43]:

$$Ti + 2H_2O \leftrightarrow TiO_2 + 4H^{4+} + 4e^- \quad (2.14)$$

In the case of titanium anodization, the predominant phenomenon is the formation of an oxide on the surface. The presence of fluoride ions in the electrolytes will form fluoride water-soluble $[TiF_6]^{2-}$ species. The fluoride ions that are present in the electrolytes can react with Ti^{4+} or can chemically attack the formed TiO_2:

$$Ti^{4+} + 6F^- \rightarrow [TiF_6]^{2-} \quad (2.15)$$

$$TiO_2 + 6F^- + 4H^{4+} \rightarrow [TiF_6]^{2-} + 2H_2O \quad (2.16)$$

These fluoride ions will lead to the field-assisted chemical dissolution of TiO_2 (Equation 2.16) Small pits are formed due to the localized dissolution of the oxide, these pits acting as pore-forming centers.

Anodization processes with electrolyte containing species capable of dissolving the anodized oxide layer (F^-), show three characteristic stages. In the first stage, a barrier oxide layer is formed (a few tens of nm). Then, during stage two, the surface begins to be locally dissolved and the pores grow randomly. The initiation of these pores leads to an increase in the active area and therefore an increase in the current [44]. Consequently, the pores share the available current equitably, which leads to the formation of a network of vertically ordered nanotubes (stage three). In this phase the current becomes constant. More precisely, the steady-state is established when the growth rate of the oxide is equal to its rate of dissolution (Figure 2.5) [44].

During the anodization process it is possible to obtain nanotubes and nanopores surfaces according to the anodization parameters. Both nanotubes and nanopores are interesting and will be investigated in this project.

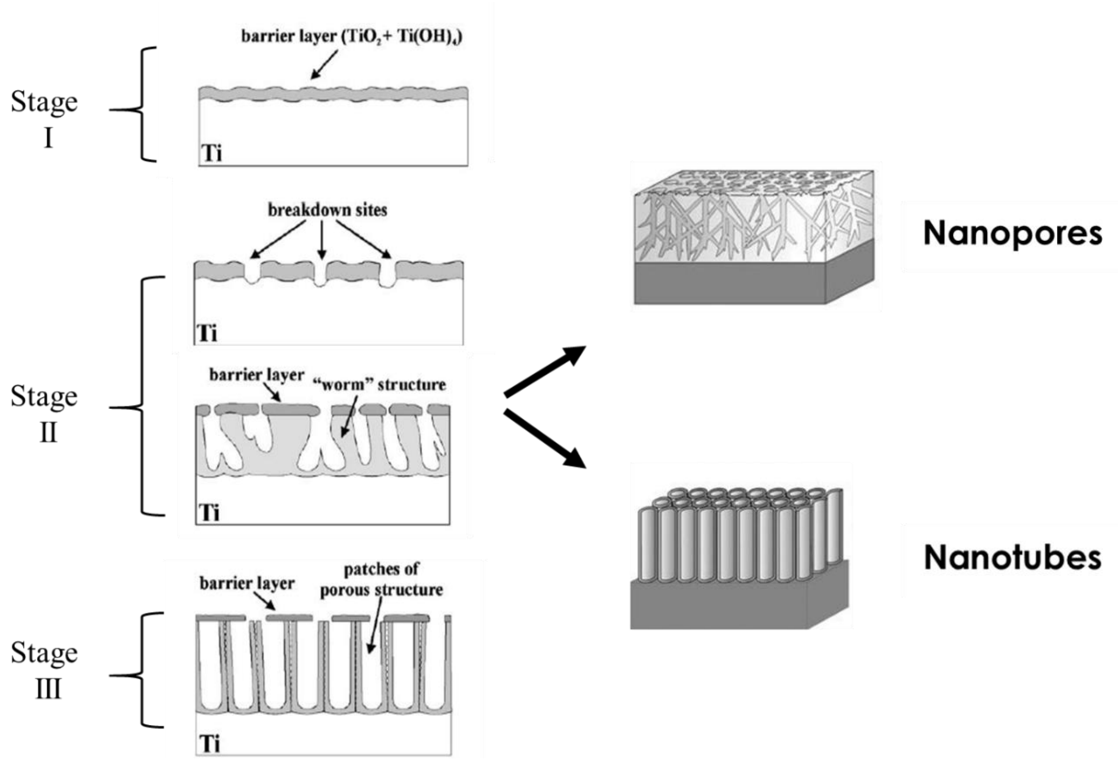

Figure 2.5 Schematic representations of the different stages of the anodization process: Stage I oxide layer formation; Stage II pores nucleation and dissolution of the TiO2 layer; in Stage III the steady-state is established.

After the anodization process, the samples are often subjected to an annealing treatment at high temperatures (400 to 600 °C) to transform the TiO_2 from an amorphous phase to a crystalline one [45]. Crystalline nanotubes possess a stronger adhesion to the titanium substrate and increased hydrophilicity [46]. Additionally, this thermal treatment decreases the amount of fluoride remaining in the anodized surface, which might be toxic to the cells, favoring the biological response [36, 47].

2.4 Corrosion of biomedical devices

Surface degradation on biomedical devices occurs due to the interfacial reaction between the passive film and the surrounding environment. Generally, surface modifications to improve the biological response, modify the surface area and the chemical characteristics of the surface, causing a decrease in the corrosion performance. High corrosion resistance is required to reduce the release of metallic ions to the body, which can be harmful to the organism. A very small amount of released metal ions may cause an allergic response and carcinogenesis in the human body [48, 49].

Corrosion of metallic biomaterials causes the loss of their structural integrity and surface function. It accelerates their fatigue, fretting fatigue and wear and, conversely, such damages accelerate the corrosion [49]. Due to these problems, electrochemical characterization is one of the most important mediators to evaluate new surface treatments for metallic biomaterials [48].

Generally, when a metallic material is immersed in an electrolyte, an infinite number of atomic-size anodes and cathodes are formed as shown in Figure 2.6. At this moment short-circuit current flows between local anodes and cathodes. The place of local anodes and cathodes changes every moment in the case of general corrosion. Moreover, the total anodic current is equivalent to the total cathodic current. As a result, the whole surface is uniformly attacked [49].

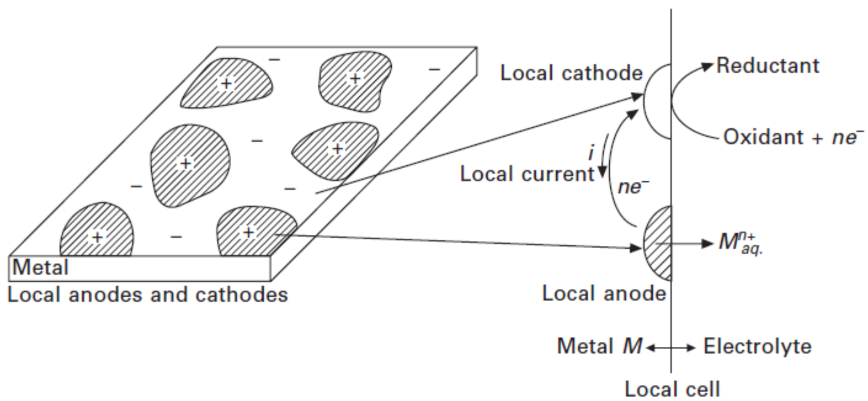

Figure 2.6 Schematic illustration of the local anodes and cathodes and the local cell formed between them [49].

2.4.1 Potentiodynamic polarization

Polarization is an electrochemical process induced by deviation of the electrochemical equilibrium potential (*Ecorr*), the potential at which anodic and cathodic reactions have an equal rate (net current is zero). The rate of the anodic partial reaction at the corrosion potential in Figure 2.7 is called corrosion current density (I_{corr}), which is proportional to the corrosion rate [49, 50].

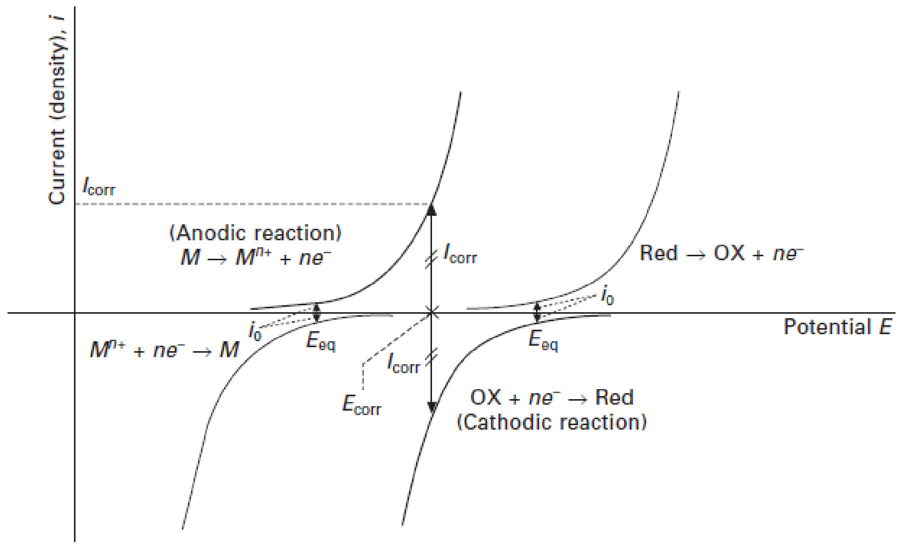

Figure 2.7 Schematic illustration of potential vs current density curves of a metallic electrode. E_{corr} = corrosion potential; E_{eq} = equilibrium potential; I_{corr} = corrosion current density; i_o= exchange current density [49].

Some metallic materials, such as stainless steel, aluminum, titanium and their alloys, can passivate as they spontaneously form a protective oxide layer on the surface. The anodic currents measured for these systems are then often very low and the shape of the current-voltage curve is modified as is possible to see in Figure 2.8 [51].

Figure 2.8a illustrates, for example, the characteristic shape of the anodic polarization curve of stainless steel in an acid electrolyte. In such an aggressive medium, this stainless steel loses its passive layer, and undergoes generalized corrosion, see "Active region", left part of the graph. With an increase in potential, the passive layer can reform, causing a decrease in the current density. For still slightly higher potentials, the current density stabilizes and we see a passive plateau appearing (*ipass*). In this area, the metal is protected by the spontaneous formation of the passive layer. Finally, for very high potentials, the passive layer can be destroyed; it is the domain of transpassivity, see right part of the graph [51].

Figure 2.8b illustrates the shape of the anodic polarization curve of a passivable metal in a non-aggressive medium. This is the case of titanium in a neutral medium, for which the passive layer is very stable over a wide range of potential; and this even in the presence of chlorides. Here, only the domain of passivity (*ipass*) is observed [36].

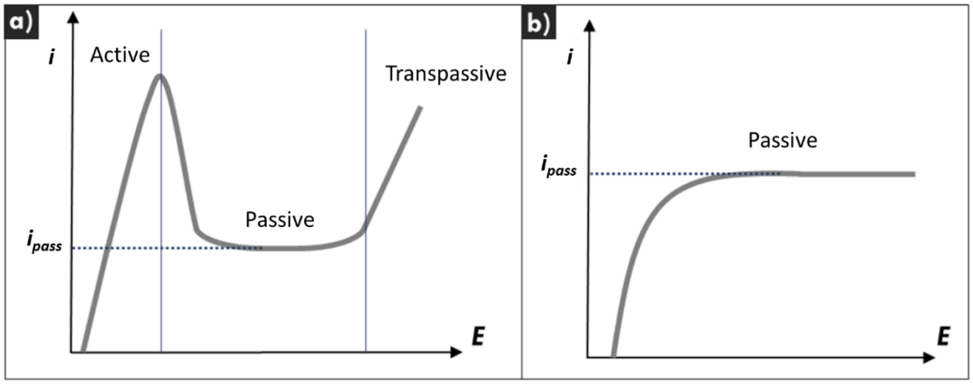

Figure 2.8 Schematic representation of the anodic part of the polarization curve (a) of a stainless steel in an acid medium (b) of a passive metal in a non-aggressive medium. Adapted from [36].

In Figure 2.9 is possible to observe the different characteristic polarization behavior for three different common metallic biomaterials, these anodic polarization curves were measured after one-week immersion in Hanks' solution. As examples, the curve of 316L stainless steel shows an abrupt increase in current density due to stable pitting corrosion that finishes the passive region, the cobalt-chromium alloy shows an increase in current density due to transpassive dissolution following the passive region whereas pure titanium shows a constant passive current density in the potential region of this study [52].

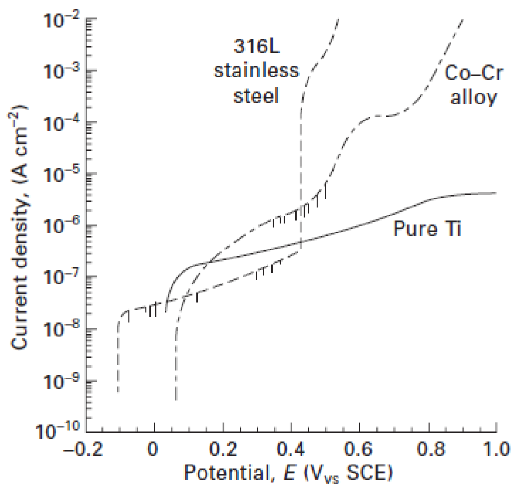

Figure 2.9 Anodic polarization curves of 316L stainless steel, cobalt-chromium alloy and pure Titanium immersed in Hanks solution [52].

Recently proposed works suggest the use of biomimetic materials in order to imitate the mechanical, physical, chemical and biological properties of the bones. An example consists in modifying titanium surface with a composite coating obtained by plasma electrolytic oxidation (PEO) with organic pore filler of integrin-active RGD.

This surface modification improved its biological properties. On the other hand, it reduced the corrosion resistance, showing higher corrosion current density values when compared with uncoated samples, CG-Ti and nano-Ti, see Figure 2.10. This behavior was attributed to the electrochemically active Ca and Na species contained in the coating layer and more defects in the layer [53].

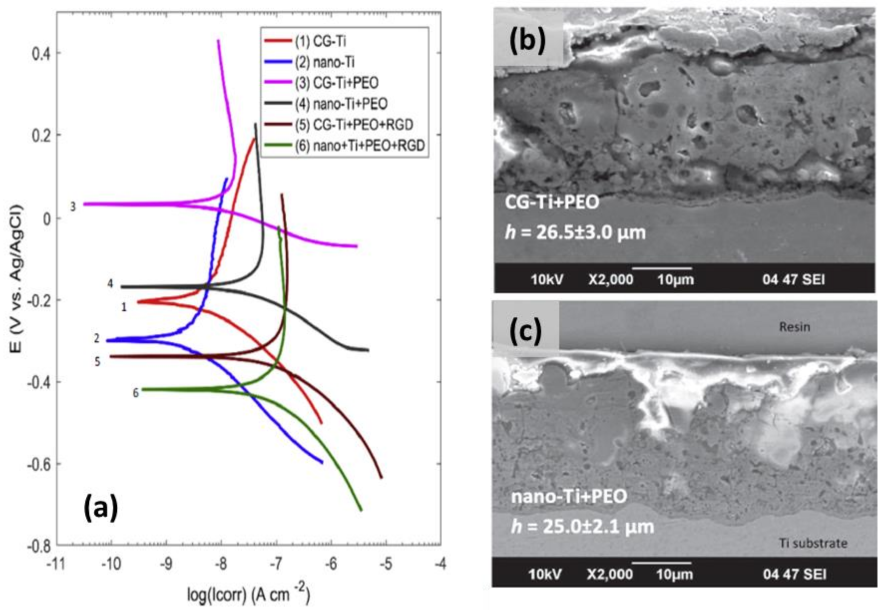

Figure 2.10 (a) Potentiodynamic polarization test results for CG and nanostructured titanium substrates, uncoated, PEO coated and RGD modified and PEO coating morphology for (b) coarse-grained and (c) nanostructured titanium substrates [53].

On the other hand, some surface modification processes as anodization of the commercial pure titanium have proven to be very interesting, forming a surface highly bioactive, and maintaining a high corrosion resistance compared with the untreated titanium, see Figure 2.11. The anodized surfaces showed a clear increase in the corrosion potential and lower values of the corrosion current density compared with untreated titanium. The authors attributed these results to an increase in the thickness of the oxide layer [54].

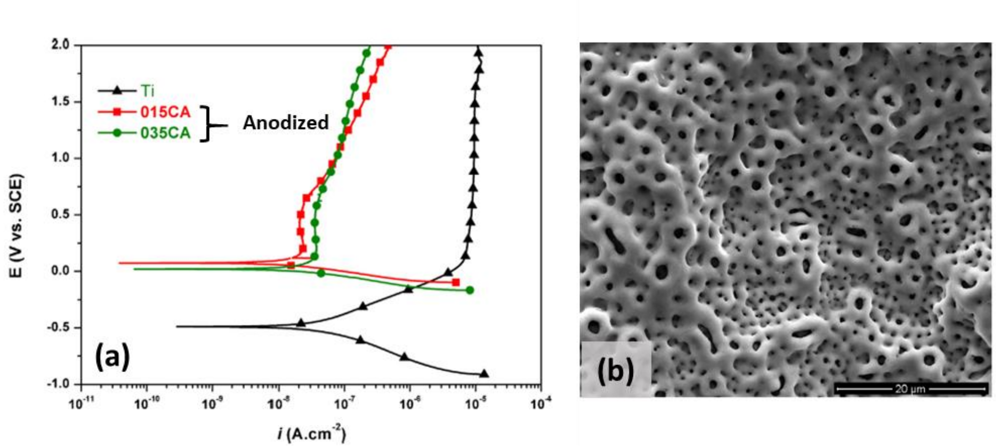

Figure 2.11 (a) Potentiodynamic polarization curves of the untreated and anodized titanium samples in NaCl (8 g/l); and (b) representative SEM image of the anodic treated titanium sample [54].

2.4.2 Electrochemical Impedance Spectroscopy (EIS)

Although rich in information the potentiodynamic polarization test is a destructive method and provides information about the slowest phenomena taking place on the surface of a material exposed to a corrosive environment [55]. On the other hand. the EIS is a non-destructive test and a very sensitive detection method of the coated metal condition. Hence, the EIS technique has been used to evaluate the corrosion state of different metallic biomaterials [53]. Contrary to the potentiodynamic polarization methods, which use direct current (DC), the EIS is based on the excitation of the interface by a low amplitude alternating current (AC). A small-amplitude sinusoidal potential perturbation is typically applied to the working electrode (5-10 mV) at a number of discrete frequencies. During the EIS test, a potential waveform of a few millivolts is applied across the circuit, and the current response to the frequency signal generates impedance data. Thus, the impedance data is related to a phase shift angle and a variation in potential and current amplitudes. (See Figure 2.12) [54].

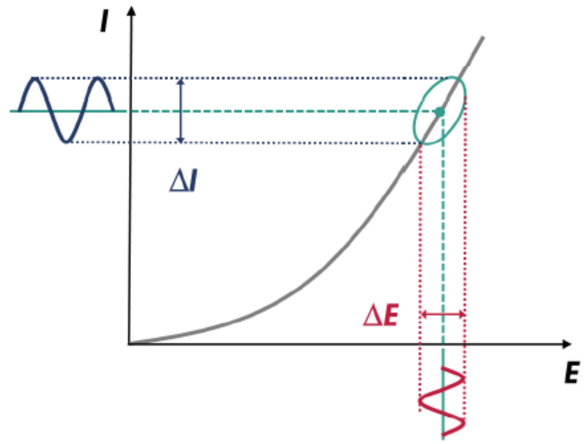

Figure 2.12 Schematic representation of the principle of measurements by EIS.

The impedance measurements are valid when the system is stationary or quasi-stationary, linear and time-invariant. The linearity is verified by the use of an input signal of low amplitude (typically 10 mV), the stationarity and the invariance are ensured by the measurement of the potential in open circuit (OCP) preceding the measurement of impedance [56]. Thus, the impedance of the system is defined by the ratio between the input signal and the output signal. This relationship can be written as:

$$Z(\omega) = \frac{E_0}{I_0}\exp(j\Phi) = |Z|\,(cos\Phi + jsin\Phi) = Z_r(\omega) + jZ_i(\omega) \tag{2.17}$$

Where E_0 is the amplitude of the excitation signal, I_0 is the amplitude of the output signal, ω is the angular frequency ($\omega = 2\pi f$ where f is the frequency in Hz) and Φ is the phase shift (in °) between the input signal and the output signal, Z_r is the real part of the impedance (in Ω or Ω cm²), Z_i the imaginary part (in Ω or Ω cm²) and |Z| the module or magnitude of the impedance vector (in Ω or Ω cm²) [57].

The magnitude of the impedance can be expressed in terms of the real and imaginary components as:

$$|Z(\omega)| = \sqrt{Z_r(\omega)^2 + Z_i(\omega)^2} \tag{2.18}$$

The phase angle can be obtained from:

$$\Phi(\omega) = tan^{-1}(\frac{Z_i(\omega)}{Z_r(\omega)}) \tag{2.19}$$

Two types of complementary graphic representations are used to analyze the impedance measurements. One of them is a complex plane plot called the Nyquist plot or complex plot. It is a curve of the imaginary part of the impedance (Z_i or Z´´) versus the real part of the impedance (Z_r or Z´) (Figure 2.13 (a)). In this plot, the imaginary impedance of the electrochemical systems is usually negative [58].

The second type is the Bode plots, divided in the impedance modulus (|Z|) or the phase angle (ϕ), versus the frequency (ω). This representation generally makes easier to count the interfacial phenomena involved in the impedance response. It also allows quick visualization of the value of the low-frequency module, which provides information on the corrosion resistance of the system [36].

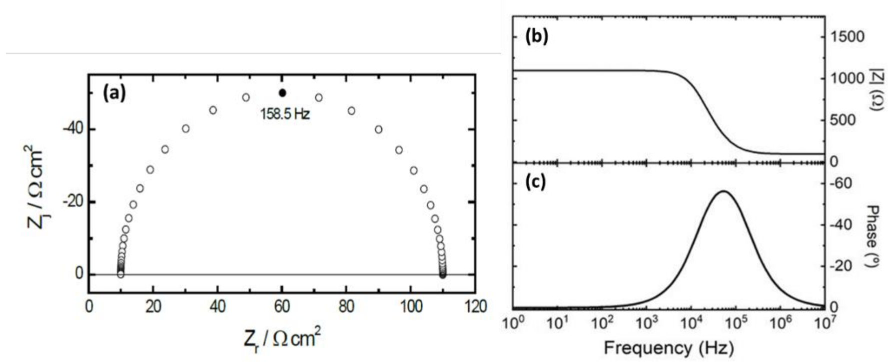

Figure 2.13 Schematic representation of the impedance results: a) Nyquist plot or complex plot; b) magnitude of the Bode plot and c) phase of the Bode plot.

The Bode representation shows some disadvantages in electrochemical systems due to the influence of electrolyte resistance (Re). For instance, in the traditional phase angle plots shows the current and potential in phase at high frequencies; however, in this region, the current and surface potential are exactly out of phase. This alteration is associated with the fact that at high frequencies, the impedance of the surface tends toward zero, and the Re dominates the impedance response. Thus, R_e obscures the behavior of the electrode surface in the phase angle plots [59].

It is possible to correct the influence of electrolyte resistance, according to:

$$|Z|_{corrected} = \sqrt{(Z_r - R_e)^2 + {Z_i}^2} \quad (2.20)$$

The phase angle can be obtained from:

$$\Phi_{corrected} = tan^{-1}(\frac{Z_i}{Z_r - R_e}) \quad (2.21)$$

Cordoba-Torres et al [60]. showed that in some systems the number of distributed processes involved in the impedance response can be determined using the corrected bode phase angle plots. This knowledge is a crucial point in the choice of the equivalent circuit if reliable results are desirable. The corrected Bode phase angle plot (Figure 2.14 b) shows three distributed processes involved, which are, however, hardly recognized in the Bode phase angle plot (Figure 2.14 a), using the same impedance data.

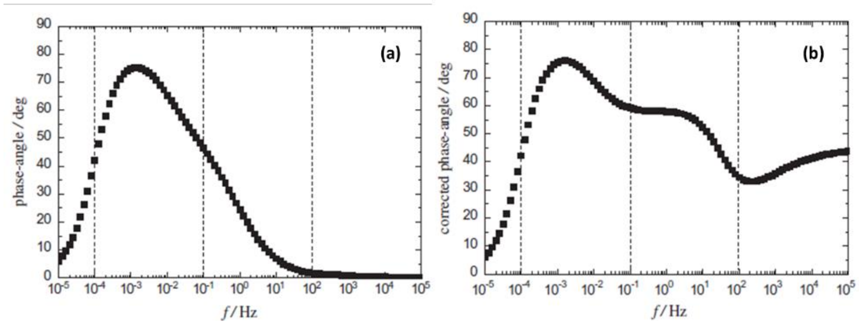

Figure 2.14 representations of synthetic impedance data in standard units: a) Bode phase-angle; (b) Corrected Bode phase-angle. (adapted from [60])

2.5 Fatigue in metallic biomaterials

Fatigue strength is one of the most important mechanical properties in implants exposed to cyclic loading conditions. When a specimen or component is subjected to repeated or fluctuating reproductions, it may break under a maximal acting stress lower than the strength limit of the material [61]. Final fatigue failure usually occurs suddenly (macroscopically) and catastrophically, after the generated fatigue crack grows over time to a critical value unsupported by the structure [62].

Crack nucleation in fatigue occurs due to localized submicroscopic damage, and the presence of any localized stress amplifier may favor the onset of premature damage, and, subsequently, the formation of a crack [63]. This stress amplifier is usually caused by a notch or a discontinuity present in the component. These defects can be introduced on purpose and are known as structural notches; examples are gear teeth, screw threads, or any general holes [63].

Surface topography in titanium alloys is very important due to the fact that it will determine the level of cell adhesion and growth on the implants [64, 65]. Thus, those processes that modify surfaces for better osseointegration may also cause changes in fatigue life behavior [66].

Leinembach et al [67] studied the fatigue performance of Ti-6Al-4V alloy after an Al_2O_3 particle blasting process, generating a Ra ≈ 4.6 µm roughness. In this α + β alloy, a 31% decrease in fatigue strength was observed when compared to polished surface, a result which was attributed to the concentration of surface stresses generated by the presence of the remaining blasting particles, as well as to the roughness generated. A different behavior was observed in the work of Pazos et al [66] when pure titanium was blasted with Al_2O_3 particles, resulting in fatigue strength similar to the condition of polished specimens.

Ti-6Al-7Nb specimens (α + β alloy) were treated by thermal and anodic oxidation, showing a roughness of 0.121 µm and 0.065 µm, respectively. The anodically oxidized samples showed a slight decrease in fatigue performance when compared to the polished ones, but showed a more positive response when compared to the thermally oxidized samples (Figure 2.16).This behavior was attributed to a more fragile characteristic of the oxide layer formed by heat treatment [68].

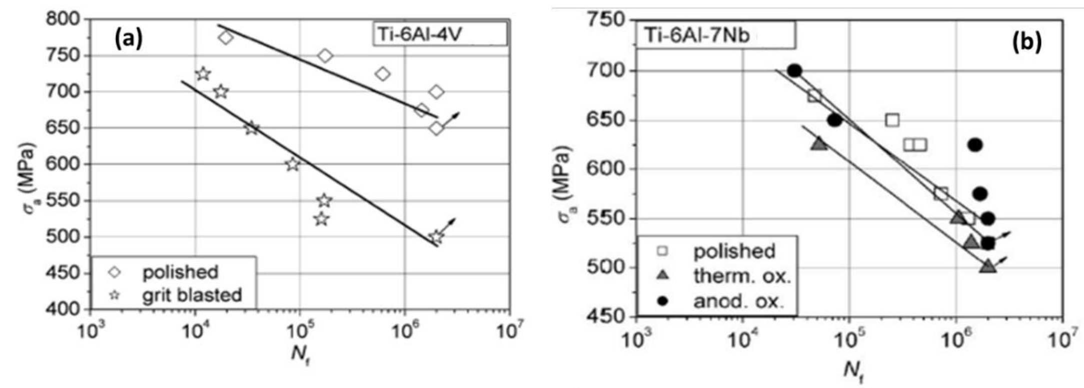

Figure 2.15 Axial loading S,N-curves in oxygen-saturated Ringer's solution: a) polished and grit blasted Ti-6Al-4V; b) polished, thermally and anodically oxidized Ti-6Al-7Nb (Adapted from [68])

Plasma electrolytic oxidation process was employed in order to produce porous oxide layers on the surface of Ti-6Al-7Nb and Ti-6Al-4V alloys, it was observed that this treatment markedly decreased the fatigue strength of these alloys, being between 17- 61%. This decrease can be attributed to two factors, the first being the formation of fragile TiO_2 layers that favor surface cracking, and the second to the propagation of pre-existing cracks and the accumulation of internal stresses during the oxidation process [69].

Due to the great variability in fatigue results for these titanium alloys used as biomaterials, P. S de Carvalho et al. [70] determined the notch sensitivity of Ti-6Al-4V-ELI alloy by calculating the critical value of roughness Rz_{cri} = 2.8 μm (Figure 2.16), which indicates that variations of the surface roughness above the critical value may result in a large reduction of the fatigue resistance of this alloy [70].

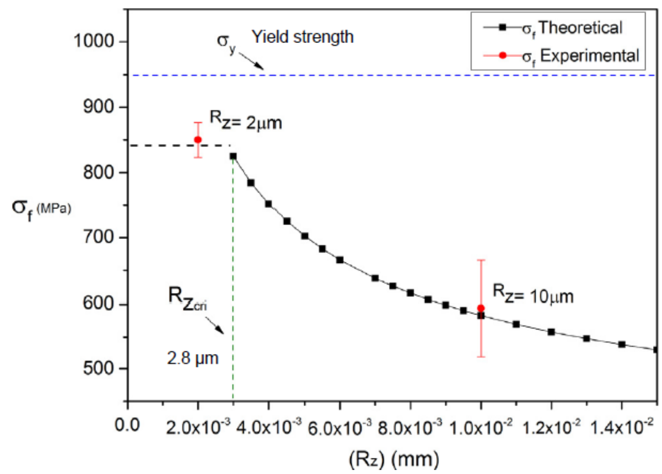

Figure 2.16 Plot of fatigue resistance (σ_f) in function of the Roughness (Rz)

Ordered arrays of TiO_2 nanotubes are considered as very promising to improve the osseointegration of titanium-based implants to living tissues. However, this improvement could be accompanied by an alteration in mechanical properties. An array of self-organized TiO_2 nanotubes with an amorphous structure was produced on the biomedical Ti-6Al-4V and Ti-6Al-7Nb alloys. This surface modification was not deleterious to the fatigue response of both α+β alloys mainly due to the nano-scale dimension of the nanotubes layer [71].

Some studies show a decrease in mechanical properties due to the incorporation of hydrogen inside titanium alloys after they are chemically treated in acidic solutions. During these processes, hydrogen ions are dissolved in the titanium matrix causing brittleness and degrading the mechanical properties. Just a small addition of hydrogen (40 ppm) can cause great harm in this TA15 titanium alloy (34% reduction of the number of cycles to failure) [72].

Other interesting studies appoint that increasing the volume fraction of β phase in α+β alloy could reduce the sensitivity of the hydrogen embrittlement due to higher solubility of this element in β phase, approximately 5 times higher than in α phase [66]. Nevertheless, some β titanium alloys as the Ti-5Al-5Mo-5V-3Cr with a microstructure consisting of a large volume fraction of fine secondary α in the β matrix, shows that a slight increase in hydrogen content produces a reduction in fracture toughness (38%) and fatigue resistance (Figure 2.17) [73]. These results show that the role of the β phase in the hydrogen embrittlement process of titanium alloys is still unclear.

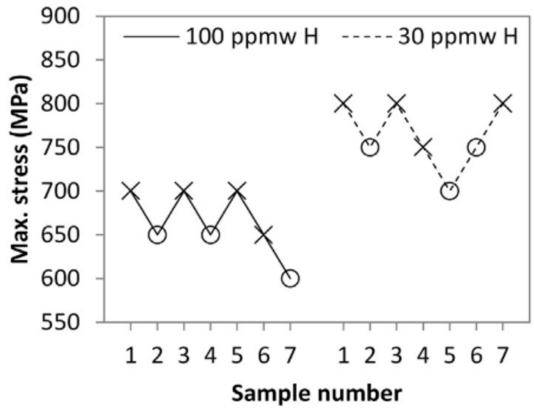

Figure 2.17 Staircase fatigue diagrams for 5×10^6 endurance limits. “X” means failure and “O” means survival to the run-out [73].

Summarizing, surface topography is very important in orthopedic and dental implants since it will determine the level of cell adhesion and osseointegration. Modifying the surface of the implant for better osseointegration may decrease its corrosion and fatigue performance. Therefore, finding a balance between biological, electrochemical and mechanical properties is a challenge in designing an implant device subjected to cyclic loadings. Thus, in this thesis the surface of the commercial β titanium alloy was modified by anodizing processes and acid etching together with an alkaline attack, to improve their bioactivity response. Then, the electrochemical and fatigue behavior of these samples were studied as will be detailed further in the manuscript.

3 MATERIALS AND METHODS

The main experimental procedures developed during this doctoral project are contained in the flowchart in Figure 3.1

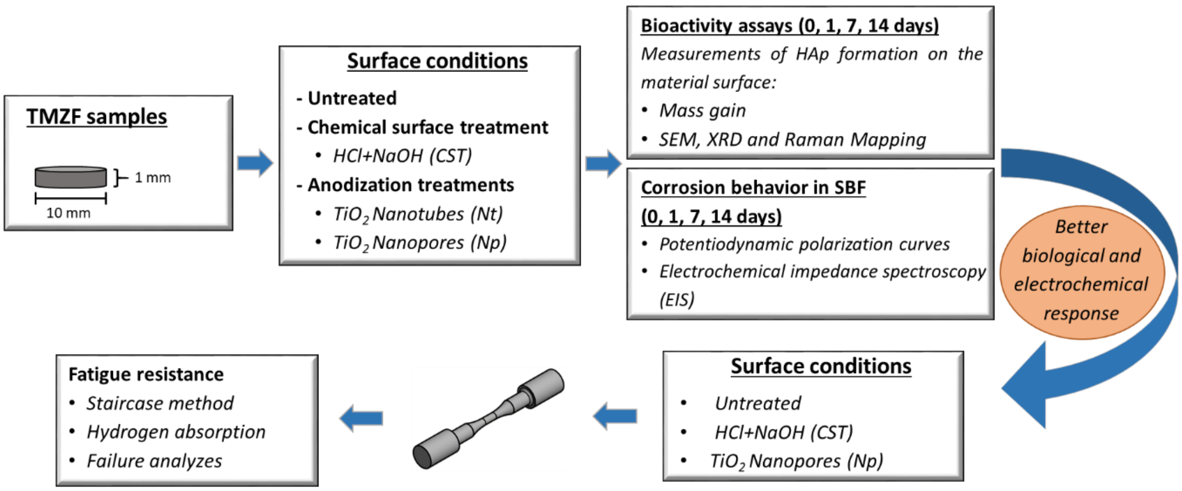

Figure 3.1 Flowchart of the experimental procedure developed in this doctoral thesis.

3.1 Materials and samples

The material used for this study was the β TMZF alloy. It is a commercial titanium alloy, purchased in the form of an ingot, and supplied by *Ercata GmbH*. The nominal composition of the alloy is shown in Table 3.1. Later, the material was submitted to the rotary swaging process in an open matrix, with repeated heating cycles in a muffle furnace to a temperature of 1000 °C, providing bars with a diameter of 11 mm.

Table 3.1 nominal composition of the TMZF alloy [2].

Material	Ti	Al	Mo	V	Cr	Zr	Fe	O
TMZF	Balance	-	10,0-13,0	-	-	5,0-7,0	1,5-2,5	0.008-0,28

For biomedical and corrosion tests the TMZF bars were cut into disks of 10 mm of diameter and 1 mm of thickness. For fatigue tests, the specimens were machined from the same TMZF bars, according to the dimensions illustrated in Figure 3. *2*, assuring the relationship between the dimensions according to the ASTM E466-07 standard [74]. All samples were heat-treated at 800 °C for two hours and then fast cooled in water to obtain a fully recrystallized beta phase structure [2].

Then, the elastic modulus was obtained employing the pulse excitation technique (ASTM E1876).

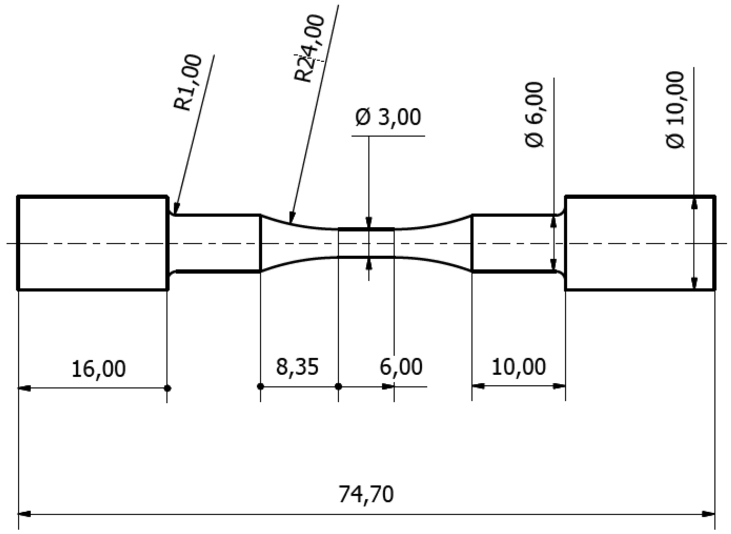

Figure 3. 2 Dimensions of specimens for fatigue tests (in mm).

3.2 Surface modification processes

Four different surface conditions were investigated on TMZF samples: untreated surface, surface treated with HCl etching and alkaline NaOH solution (CST), and two anodized condition – nanotubes (Nt) and nanopores (NP).

3.2.1 Surface preparation

In order to eliminate the machining marks, all specimens were successively grounded with 120, 240, 360, 400, 600 and 1200 grade silicon carbide papers and then polished with alumina of 3 and 1 μm. Then, they were cleaned ultrasonically into deionized water (Milli-Q®), acetone, and ethanol for 10 minutes in each case. Finally, the samples were rinsed with distilled water and dried with compressed air.

3.2.2 Chemical surface treatment

The surface modification of the specimens was carried out in two steps: initially with HCl, and subsequently with NaOH. The acid etching was carried out as a pre-treatment to remove surface oxidation and contaminants, and to generate a micro-rough and uniform surface. After the acid etching the specimens were treated with NaOH to generate submicron and nanometric changes, forming a bioactive sodium titanate layer on the treated surface.

For acid etching, samples were immersed into an HCl solution (37 wt.%) heated at 60 °C for 30 min. The alkali treatments were performed using polyethylene containers with 45 ml of NaOH 10 mol·L^{-1} for each sample, and a furnace with a digital controller was used to keep the alkaline medium at 60 °C for 24 h. The pH of the acid and alkaline solutions was <2 and >13, respectively. After the chemical modification, the samples were immersed into deionized water and sonicated for 10 min, followed by 10 min in acetone.

3.2.3 Anodization process

The TiO_2 nanostructures were obtained by anodization of the polished samples. The anodization processes were carried out in an electrochemical cell with a conventional two-electrode arrangement. The counter electrode (cathode) was a cylindrical platinum grid placed ~3 cm away from the polished disks, which were used as the working electrode (anode) in the case of bioactivity and corrosion test samples (Figure 3.3a). For the fatigue specimens (anodes), the counter electrode was a 304 stainless steel tube (Figure 3.3b).

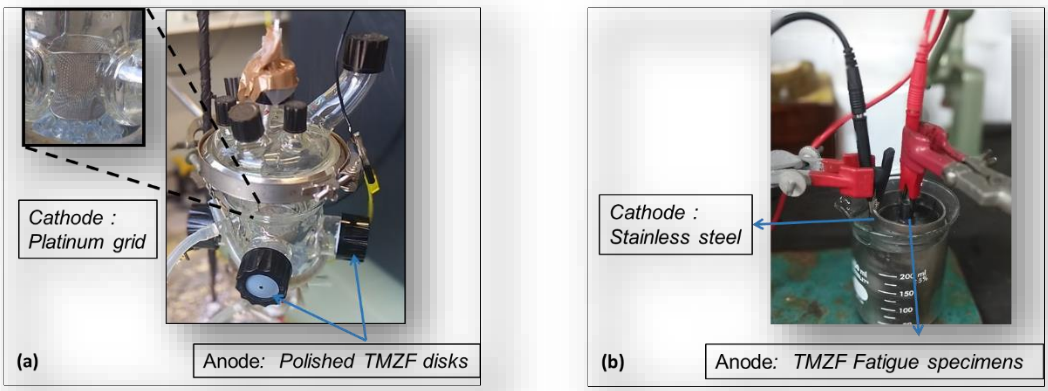

Figure 3.3 electrochemical cells used in this work for anodization experiments: a) assembly for polished disks and b) assembly for fatigue specimens.

The anodization experiments were performed at 25 °C, in an organic electrolyte consisting of glycerol, containing 25 vol% of water and 0.25M of NH_4F [75]. The DC constant potential applied to obtain nanotubes was 10V during 2h and 20V during 1h was employ to obtain nanopores.

After the anodization processes, the samples were rinsed with distilled water, then with acetone, and finally dried with compressed air.

Finally, the samples were annealed in air at 550 ºC for 2 h to crystallize the TiO_2 surface layer into a mix of anatase and rutile phases.

3.3 Bioactivity assay

Some bioactive materials bond to living bone through a layer of apatite. It has been shown that this apatite layer can be reproduced on the materials surfaces in an acellular and protein-free simulated body fluid (SBF) with ion concentrations nearly equal to those of human blood plasma (Figure 3.4.), and that apatite thus formed is similar to the bone mineral in its composition and structure [6].

In order to characterize the bioactivity of the four different surface modified conditions, it was measured the amount of apatite (Ap) spontaneously deposited on the different samples immersed into SBF. The bone-like apatite can biologically bond with living tissue, which can estimate the *in vivo* bone bioactivity of the surface.

The protocol followed in this study for carrying out bioactivity tests was proposed by Kokubo and Takadama [76] and in ISO 23317: 2014 [6]. In this protocol, the samples are placed in hermetically closed plastic containers with 50 ml of SBF solution at 37 °C and pH 7.4. It is important to place the active surface to be tested perpendicularly to the bottom part of the container, as shown in Figure 3.4. Indeed, the SBF solution being unstable, Ca / P compounds could precipitate and deposit on the surface of the sample, which would distort the evaluation of bioactivity [6, 76].

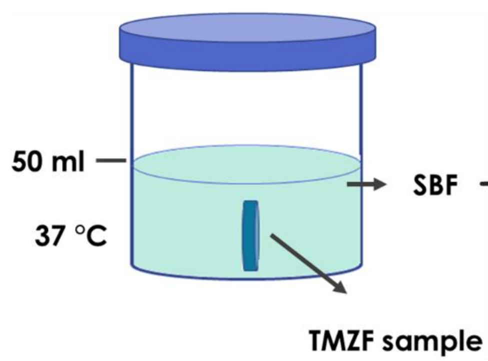

Ion	Concentration / mol·m^{-3} SBF	Human blood plasma
Na^+	142.0	142.0
K^+	5.0	5.0
Mg^{2+}	1.5	1.5
Ca^{2+}	2.5	2.5
Cl^-	147.8	103.0
HCO_3^-	4.2	27.0
HPO_4^{2-}	1.0	1.0
SO_4^{2-}	0.5	0.5

Figure 3.4 Schematic representation of the experimental assembly used to bioactivity assays and the ion concentrations of the simulated body fluid (SBF) [6].

After 1, 7 and 14 days of immersion, the samples were removed from the solution, gently rinsed and dried in a desiccator. Three samples per condition and soaking time were evaluated. Apatite formation was then evaluated by weighing the samples before and after immersion, and the morphology of each surface treatment was examined by Scanning Electron Microscopy (SEM), chemical analysis by energy dispersive spectroscopy (EDS), X-Ray diffraction (XRD) and Raman Mapping.

3.4 Electrochemical behavior

After the surface treatments, all specimens were air-aged at room temperature for 24 hours and then electrochemically tested. The electrochemical characterization was performed with a potentiostat (Gamry Instruments, Reference 600+), using SBF at 37°C and pH 7.40. A conventional three-electrode cell was used, where the TMZF samples were the working electrode with an exposed area of 0.283 cm^2, flat platinum mesh as the counter electrode, and a Saturated Calomel Electrode (SCE, 0.242 V vs. SHE at 25 ºC) as the reference electrode. The counter and the working electrodes were always kept at almost the same distance (~3 cm). In order to avoid any exchange of solutes between the reference electrode and the electrolyte, the SCE electrode was immersed into an extension tube containing a 1 mol·L^{-1} KNO_3 solution, positioned close to the work surface. In addition, the reference electrode was connected in parallel to a platinum wire connected to a capacitor of 1 µF. This device is used to avoid capacitive and inductive artifacts that can happen when recording the high-frequency impedance measurements [77]. A schematic representation of the experimental setup is provided in Figure 3.5.

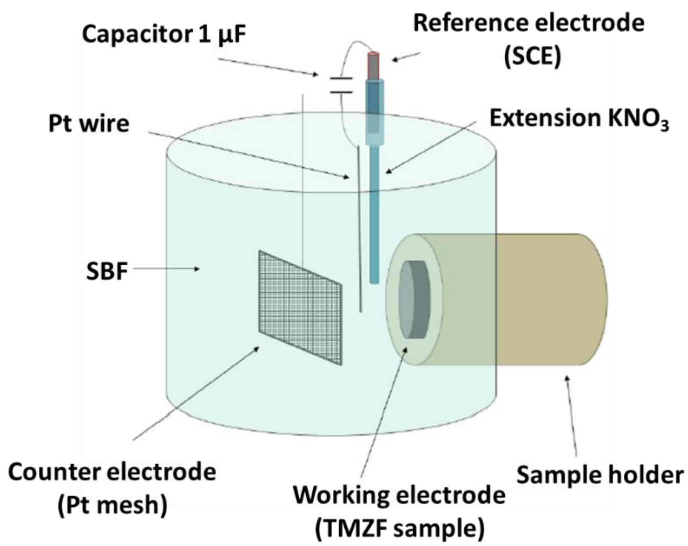

Figure 3.5 Schematic representation of the experimental assembly for the electrochemical characterization. (Adapted from [36])

The experimental assembly was placed inside a Faraday cage (steel box) connected to an Earth ground. It reduces current noise picked up by the working electrode and voltage noise picked up by the reference electrode. Additionally, the electrochemical characterizations were performed in dark environment, thus reproducing physiological conditions [36].

For the corrosion studies, three electrochemical techniques were employed. The characterization sequence firstly consisted of recording the evolution of the Open Circuit Potential (OCP) during 1 hour of immersion in the electrolyte to allow steady-state conditions to be reached. Subsequently, electrochemical impedance spectroscopy measurements (EIS) were recorded at the OCP with a frequency range of 10^{-2} - 10^{4} Hz with a sinusoidal perturbation signal of 10 mV_{rms} amplitude relative to the OCP (amplitude large enough for the output signal to be easily measured but which also allows the linearity criterion to be satisfied). Finally, the corrosion resistance was assessed through potentiodynamic polarization curves recorded over the potential range of -0.03 V/SCE to +1.2 V/SCE relative to the OCP, with a scan rate of 0.3 mVs^{-1}. These corrosion tests were performed over untreated samples, CST, Nt, and NP in four different immersion periods inside the SBF solution 0, 1, 7, and 14 days. Three samples were evaluated per condition and soaking time (different samples each time, but with the same surface treatment).

After performing the bioactivity and the electrochemical characterizations, the surface conditions that showed better results were evaluated to determine if these modifications affect the fatigue behavior.

3.5 Fatigue resistance

To accurately determine the effect of surface treatments on the fatigue response of the titanium alloy, a high cycle fatigue test called staircase (or *up and down*) was employed. This method was carried out according to ISO 12107 [78]. This is an incremental method in the sense that each test is established based on the result of the previous one. The method starts by subjecting the first specimen to a level close to the maximum stress value for a given number of cycles (typically N= $5x10^6$ cycles for implants). Sequentially, new specimens are then tested according to the following criteria: if the immediately previous test resisted to the established life, the next one is subjected to a higher stress level in a *d* value (step or fixed value of stress increase or decrease), while, if it didn't resist, it is tested at a lower level in *d*. In this way, seven specimens from each of the surface conditions (untreated, CST and Np specimens) were tested, promoting a confidence level of 50% and a probability of failure of 10%, being suitable for exploratory research. To determine the fatigue strength and standard deviation values, the Dixon and Mood statistical method was used [78].

The fracture surfaces of the different specimens were observed in the Scanning Electron Microscope in order to analyze the fracture mechanisms present.

3.6 Surface characterization

The specimens with the modified surfaces were analyzed morphologically and chemically via Scanning Electron Microscopy (SEM), chemical analysis by energy dispersive spectroscopy (EDS), crystalline apatite formation by X-Ray diffraction (XRD) and Raman Mapping.

Raman characterization was performed using a Renishaw InVia Raman spectrometer equipped with dielectric filters (InVia) to remove the Rayleigh line. Raman photons were collected with a cooled CCD. In all cases, the excitation light was the green line of an Ar laser (514.53 nm). The scanning area was 4 x 4 cm 2D map with a step size of 100 µm. Spectra were recorded at the wavelength range between 900-1000 cm^{-1}, following the characteristic peak of Hydroxiapatite at 962cm^{-1}.

3.6.1 Roughness Measurements

The roughness measurements were performed with the help of an Olympus LEXT OLS4100 LASER confocal microscope with 50X and 100X objective lenses. The Olympus Stream image analysis software was employed to perform a qualitative and quantitative analysis of the generated surfaces. Additionally, it was possible to produce a 3D image of the surface of the samples.

3.6.2 Hydrogen absorption

A LECO ONH836 element analyser was used to determine the amount of hydrogen present in the material before and after chemical treatments. Initially, disc samples were cut into small pieces. They were weighed (~ 20 mg) and deposited in a graphite container, after which the material was heated until it released the hydrogen as a gas, which is detected using non-dispersive infrared cells. The hydrogen concentration was determined relatively using calibration standards. Additionally, to determine the possibility of hydrides formation was employed a Transmission Electron Microscopy (TEM) equipped with an orientation-phase mapping precession unit NanoMEGAS (model ASTAR) and with a DigiSTAR P1000 unit.

4 RESULTS AND DISCUSSION

4.1 Bioactivity and electrochemical behavior of TMZF samples treated with CST, nanopores and nanotubes

The biological and electrochemical response of the commercially pure titanium and the Ti-6Al-4V ELI alloy treated with chemical and electrochemical processes has been extensively studied. However, the need for the use of β titanium alloys with low elastic modulus makes interesting the study of these treatments on commercial β-Ti alloys such as Ti-12Mo-6Zr-2Fe (TMZF).

In the present chapter, Hydroxyapatite (HAp) mass gain test was carried out as an indicator of the osseointegration behavior of the different surface treatments obtained over the TMZF samples surface. Additionally, the HAp growth resulting from soaked specimens in SBF solution was confirmed by SEM, EDS, XRD and Raman mapping.

Corrosion of metallic prosthesis modify their structural integrity and can cause alterations of the surrounding environment, such as changes in pH, and decrease of dissolved oxygen. Furthermore, the metal ions released may cause an allergic response and can be harmful to the patient. For these reasons, the study of the corrosion process is critical and necessary for metallic biomaterials. In this way, was studied the electrochemical behavior of the surface treated with CST, nanopores, and nanotubes through potentiodynamic polarization curves.

The microstructure of swaged and heat-treated materials consisted of equiaxed grains with grain size of 80-100 μm, as presented in Figure 4.1 (a). The evaluation of the microstructure through XRD suggested the existence of recrystallized β phase (Figure 4.1 b). which met the requirements of the standard ASTM F1813. This microstructure provides an alloy with an intermediate modulus of elasticity ~ 90±6 GPa, measured by the impulse excitation technique.

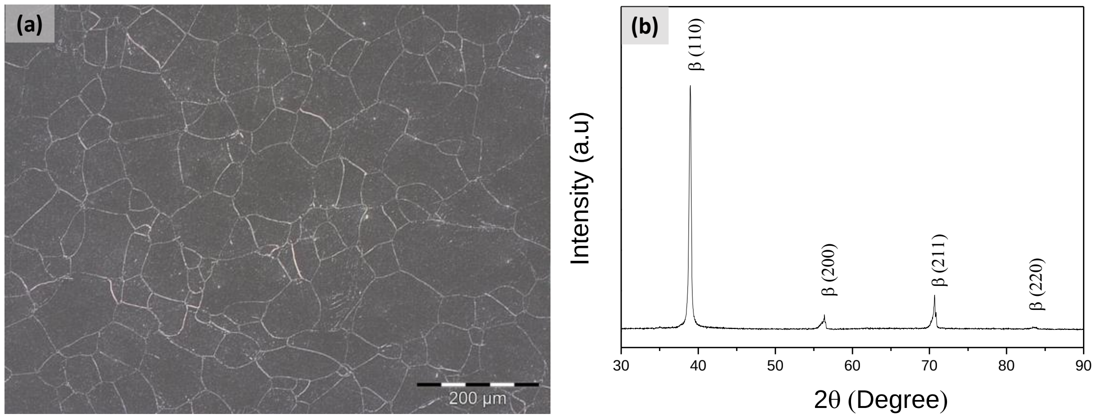

Figure 4.1 (a) Microstructure and (b) XRD spectrum of the TMZF alloy.

Figure 4.2 shows the surface of the untreated TMZF sample after the polishing process. Here, a soft topography is noted with the presence of small marks or scratches, due to the abrasion during grinding and subsequent polishing processes. This surface will be used as the reference one for the different bioactivity, electrochemical, and fatigue tests.

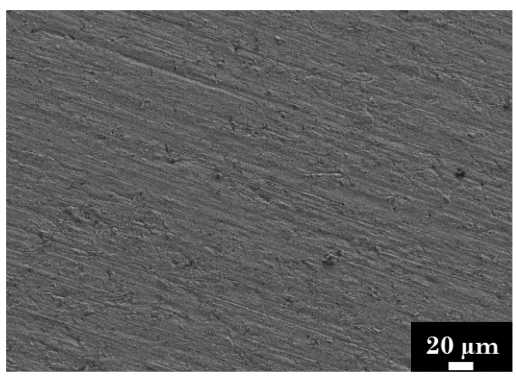

Figure 4.2 SEM image of the untreated samples after the grinded and polished processes.

The images in Figure 4.3 refer to the sample treated with hydrochloric (HCl) acid and sodium hydroxide (NaOH); it is possible to observe the effect of the attack on the entire polished surface, changing the initial, smooth morphology, by a surface with micropores uniformly distributed and reveling the grain boundaries. A higher magnification (Figure 4.3 b), was used to evaluate the presence of nanometric characteristics on the sample surface, confirming the effect of the NaOH. Here, it is possible to observe coral-like structures in the submicrometric and nanometric scale formed during the alkaline treatment.

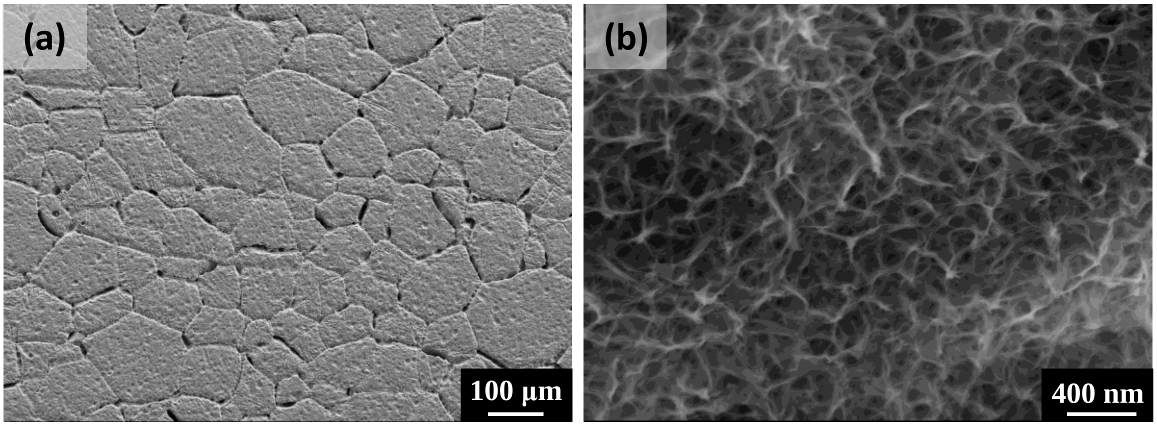

Figure 4.3 SEM images of TMZF alloy, chemically treated by HCl 37% at 60 °C and NaOH 10 mol·L^{-1} at 60 °C for 24 h.

To find the synthesis parameter for nanotubes was a little more time-demanding than expected, because the traditional parameters used for pure titanium, does not produce nanotubes in this β titanium alloy. After several try-outs varying time and voltage, it was possible to see that reducing the potential to values close or lower than 15V favors the formation of nanotubes homogeneously distributed on the TMZF surface (see Figure 4.4). Additionally, during these try-outs were found the anodization parameters for another attractive surface referred as nanopores surface.

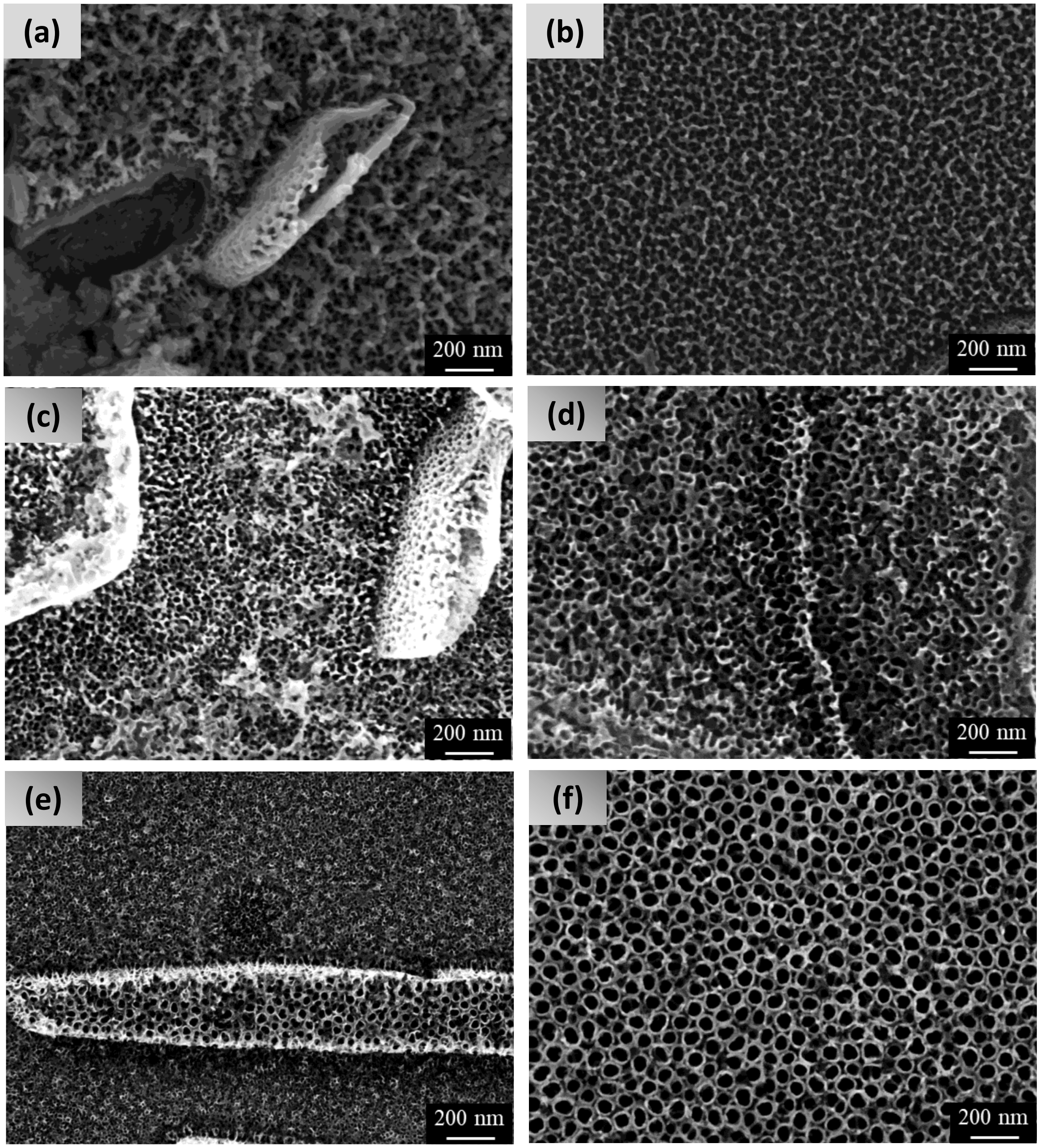

Figure 4.4 SEM images of anodized surfaces for different preliminary anodization parameter, varying the applied potential and the anodization time: a) 60V-1h, b) 40V-1h, c) 40V-2h, d) 20V-2h, e) 15V-2h and f) 10V-2h.

High-resolution SEM image in Figure 4.5 shows the final surface condition of the two different anodized systems studied in this work. Figure 4.5 (a) shows the formation of a network of vertically self-organized tubes uniformly distributed over the entire surface, while Figure 4.5 (b) shows a nanometric and disordered worm-like structure; this later mesopores surface was named as nanopores.

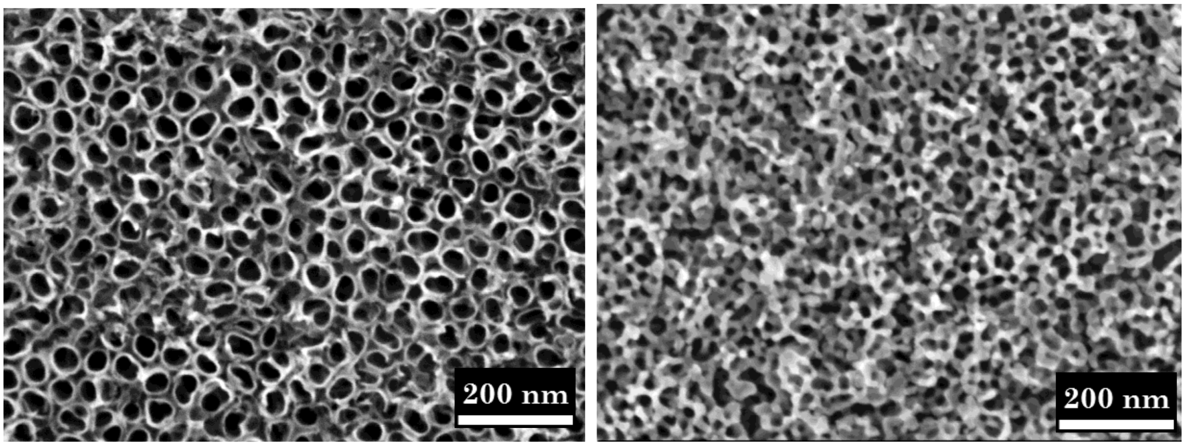

Figure 4.5 High-resolution SEM image of anodized samples: a) Nanotubes and b) Nanopores.

4.1.1 Hydroxyapatite formation test

The bioactivity assays were performed on TMZF disks untreated, with CST, nanotubes and nanopores conditions. Three samples for each condition were immersed in 50 ml of classic SBF solution at 37 °C for different periods (1, 7 and 14 days) and it was measured the amount of hydroxyapatite (HAp) spontaneously deposited on the sample surface [6].

Figure 4.6 summarizes the average value of the mass gain for three samples of each surface condition during the different periods. It is possible to see that there is no apatite deposit on the untreated TMZF alloy and nanotubes. In contrast, nanopores samples showed a moderate HAp formation after 14 days of immersion (mass gain higher than 0.5 mg).

On the other hand, CST samples show a better bone-bonding ability compared to the anodized and untreated samples. After 7 days soaking, this surface evidenced a significant apatite formation with a mass gain higher than 0.8 mg; this nucleation and growth process is maintained, showing the highest mass gain value around 1.8 mg after 14 days.

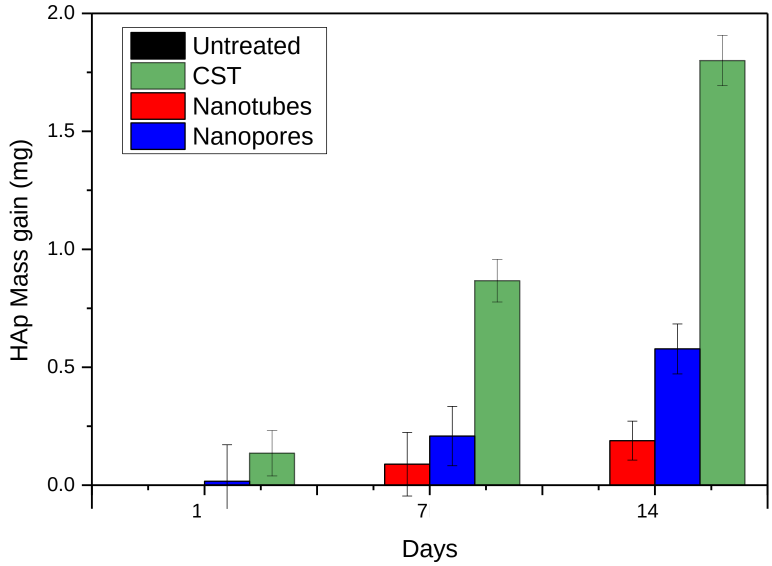

Figure 4.6 Quantitative evaluation by apatite mass gain of untreated, CST, nanotubes and nanopores samples after different immersion times in SBF.

SEM images in Figure 4.7 reveal that even after 14 days of immersion in the physiological solution, none or slight traces of HAp are detected on untreated, nanotubes and nanopores surfaces. Nevertheless, it was possible to observe HAp spheres on the CST sample after the same 14 days in SBF (Figure 4.7 d). This visual information corroborates the mass gain values obtained for the different surface treatments after soaking times.

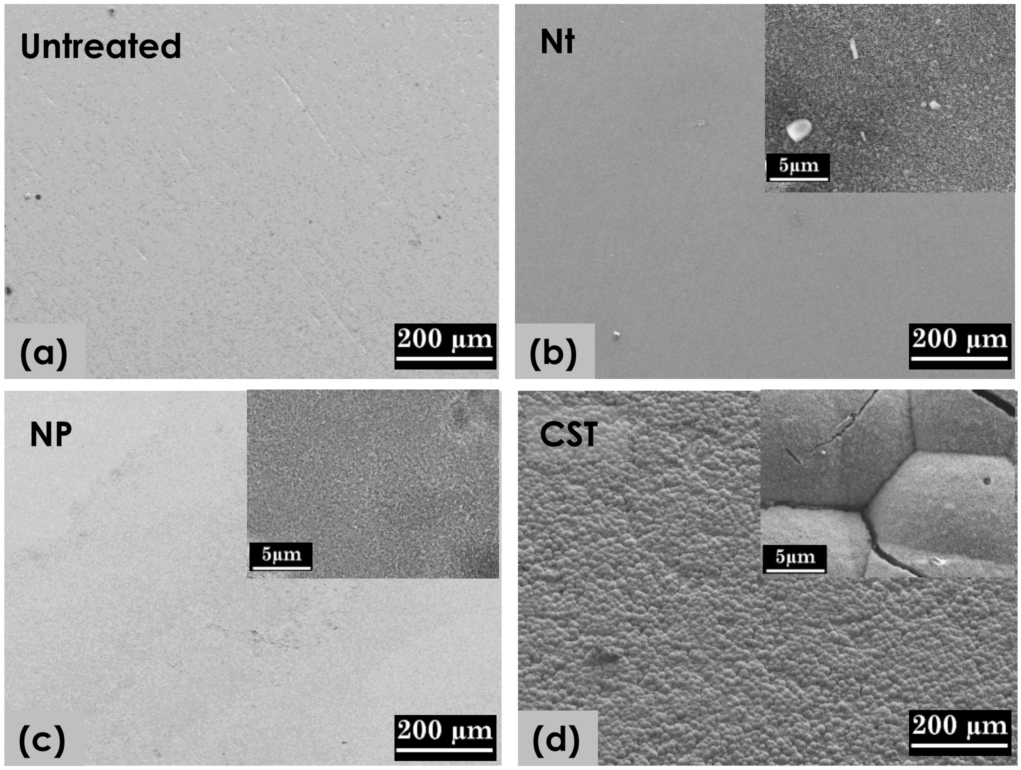

Figure 4.7 SEM images for samples of TMZF alloy subjected to the bioactivity tests after 14 days immersed in SBF. a) Untreated; b) Nanotubes; c) Nanopores and d) CST samples.

Table 4.1 shows the EDS results performed on untreated, CST, nanotubes and nanopores samples after 14 days of immersion. Only on CST and nanopores surfaces were detected the presence of calcium, phosphorus and oxygen elements that are characteristic of the hydroxyapatite present in the human body [79]. This result is corroborated by XRD patterns in Figure 4.8, where is possible to see the diffraction peaks of the crystalline HAp phase solely in the samples with CST after 14 days of immersion.

Table 4.1 Quantitative chemical EDS analysis of untreated, nanotubes, nanopores, and CST samples. After 14 days of immersion in SBF solution.

Chemical element (% at.)							
Condition	Ti	Mo	Zr	Fe	O	Ca	P
Untreated	67.32	3.79	2.15	1.94	22.75	-	-
Nanotubes	57.65	3.64	1.97	-	35.36	-	-
Nanpores	46.28	3.10	1.60	-	48.89	0.60	0.40
CST	11.88	0.54	0.24	-	59.06	16.97	9.34

In a physiological fluid, for instance SBF solution, OH- groups are adsorbed to the surface of TiO_2 to form Ti-OH bonds. Since these hydroxyl groups are slightly negatively charged, the result is an electrostatic attraction of the calcium cations, thus forming amorphous calcium titanate [75]. With the immersion time, this calcium titanate interacts with the PO_4^{3-} phosphate ions of the SBF solution to form an amorphous calcium phosphate compound [26, 79, 80]. Then, since hydroxyapatite is the most stable calcium phosphate compound in aqueous medium at pH 7.4, the surface deposit crystallizes in this form. Once formed, the crystalline apatite layer consumes the calcium and phosphate ions from the SBF solution [79].

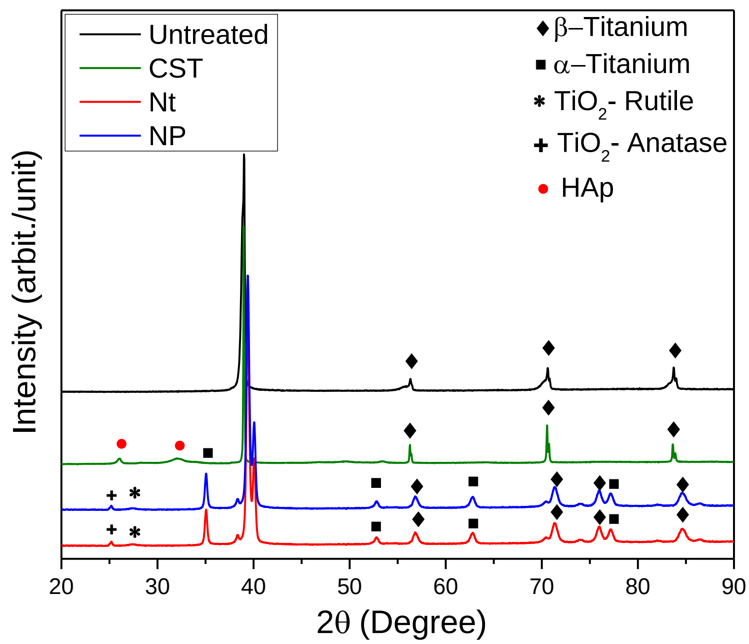

Figure 4.8 XRD patterns of untreated, CST, nanotubes and nanopores samples after 14 days of immersion in SBF.

Another complementary test to know if we have the crystalline form of the calcium phosphate (Hap) deposited on the surfaces treated, is the Raman spectral mapping. For this test was employed the wavenumber characteristic of HAp, 961cm^{-1}. In this qualitative result, the HAp formation is determined through the red color intensity; higher intensity zones mean more precipitation of this compound.

Figure 4.9 shows the difference between the different treated samples after 7 and 14 days of immersion in SBF. Independent of the immersion time, nanotubes samples showed maps with low Raman intensity, indicating low HAp formation even after 14 of immersion. In the case of nanopores samples the results are slightly better, showing different zone with precipitates of HAp after 14 days of immersion in SBF.

On the other hand, CST samples showed the best bioactivity behavior. As a result, was observed a greater amount of crystalline calcium phosphate precipitated along the entire surface of the material, even just after 7 days of immersion, indicating more favorable surface conditions for osseointegration.

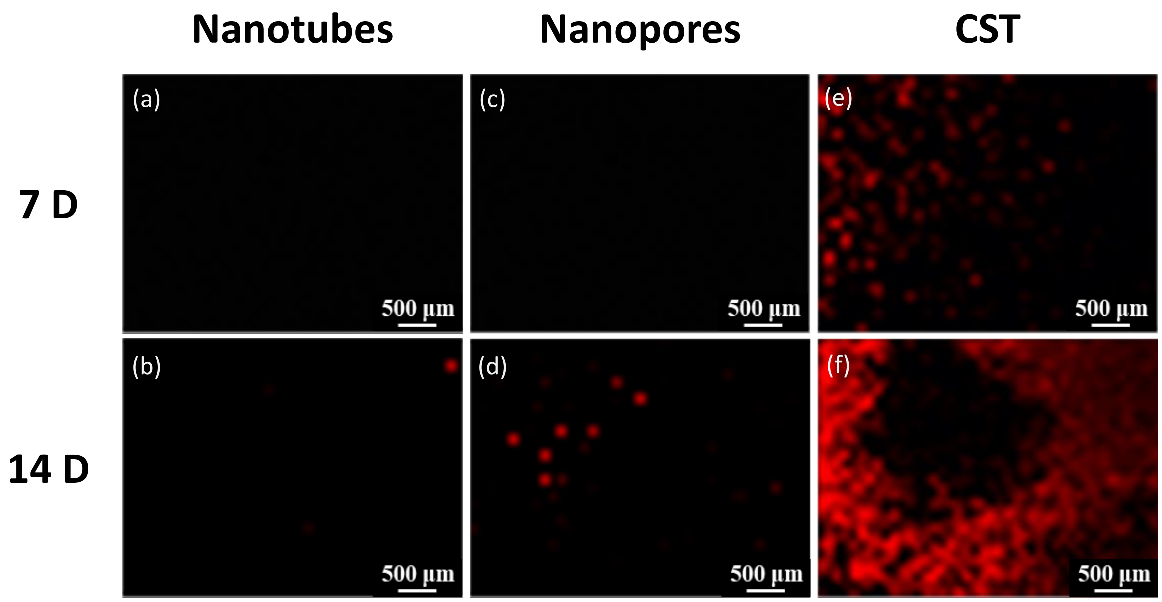

Figure 4.9 Raman spectral mapping of nanotubes, nanopores and CST samples soaked during 7 and 14 days in SBF.

The large area developed by the nanotubes and nanopores allows the formation of a significant number of -OH bonds and thus increase the number of nucleation zones responsible for the initiation of the apatite layer [81]. However, surface contamination by other oxides of metallic elements present in the alloy as Mo, Zr, and Fe, could decrease this surface potential, decelerating the apatite nucleation [82].

4.1.2 Electrochemistry characterization

Figure 4.10 compare typical potentiodynamic polarization curves of a representative sample for each surface condition and immersion time. From these curves, was calculated the corrosion potential (E_{corr}) corresponding to the position where the net current is zero and is indicated as the "peak" directed downwards on the polarization curves.

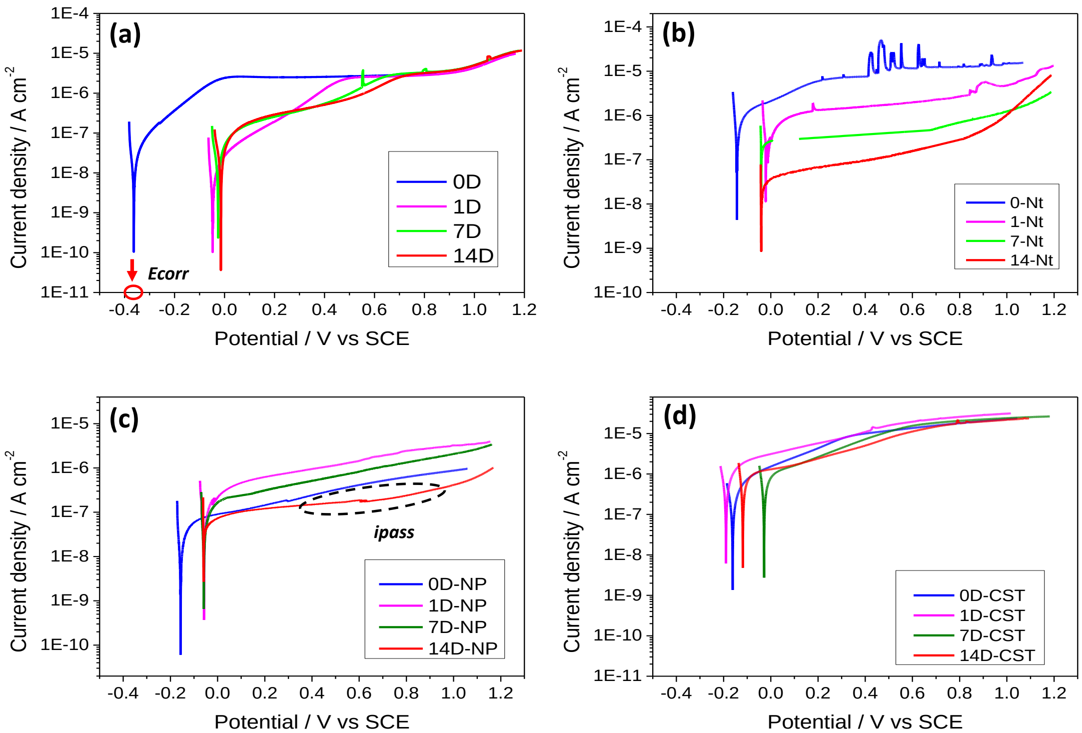

Figure 4.10 Anodic polarization curves, for the TMZF alloy in SBF electrolyte at 37 °C: a) Untreated; b) nanotubes; c) nanopores and d) CST.

The nature of the polarization curves indicated stable passive behavior for all the surface conditions and immersion periods. However, in the nanotubes sample at 0 days is observed fluctuations in the passivity domain due to the creation of a localized aggressive environment that breaks down the passivation layer [83]. These kinds of oscillations can be attributed to the competition between the formation and dissolution of the passive film. Remain fluoride ions trapped into the tubes from the anodization process could favor this phenomenon [84].

The values of E_{corr} for the four different surface treatments are summarized in Figure 4.11. These values are comparable with the potential obtained for each condition after one hour of OCP. Untreated samples show, initially, a low corrosion potential close to -0.370 V_{SCE}, but this value increases considerably after 1 day of immersion and remains almost constant at -0.050 V_{SCE} until 14 days in SBF solution.

Furthermore, nanotubes, nanopores and CST samples showed a nobler behavior (-0.072, -0.115 and -0.190 V_{SCE}, respectively) compared to untreated samples at 0 day. After 1 day of immersion in SBF solution, all of them exhibited a tendency to higher potential values close to -0.050 V_{SCE}, this behavior was less pronounced for the samples treated with HCl etching plus alkaline treatment, indicating a lower corrosion protection than the anodized samples (Figure 4.11).

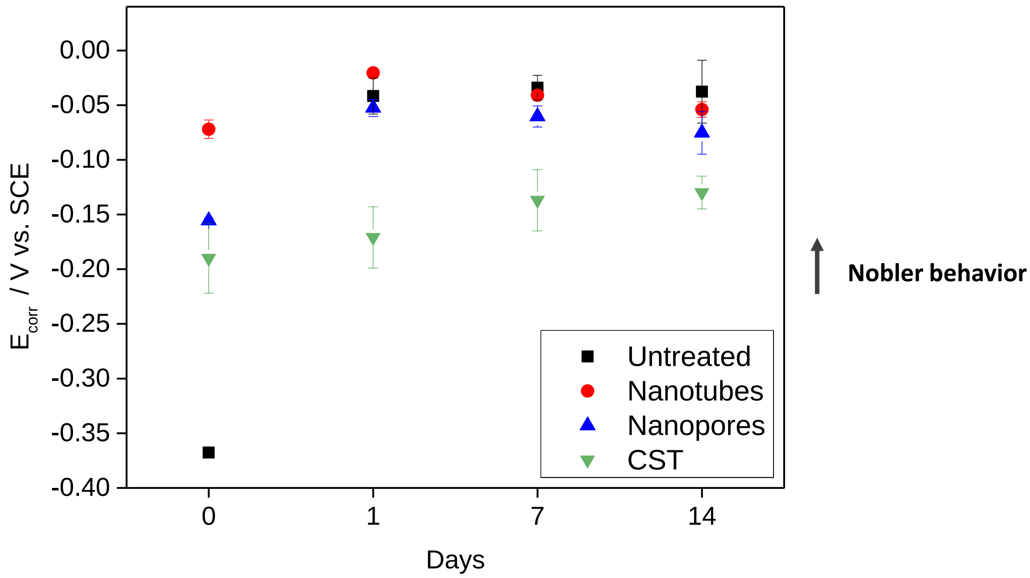

Figure 4.11 Electrochemical measurements of corrosion potential (E_{corr}) of TMZF alloy untreated and treated with nanotubes, nanopores, and CST for different immersion times in SBF at 37°C.

As part of this study, the current density of the passivation plate (i_{pass}) was chosen instead of the current density of corrosion (i_{corr}) in order to establish a better comparison between the different surfaces obtained, which are prone to passivation. However, in some passivating materials exposed to physiological environments, the current density is not independent of the potential in the passive state. One reason is the dynamic nature of the test; the changes of the film with the potential are very slow to remain stable with the scan. Another possibility is that the changes in the passive layer are uncompensated for the increased oxidative driving force during the test [83].

In practice, the shapes of the anodic branches are not identical for all the samples, and the determination of i_{pass} can be non-trivial (Figure 4.10), for these reasons the method for the determination of i_{pass}, consisted of calculating, for each sample, the average of the current densities measured in the range of potentials between +0.4 V_{SCE} and +1 V_{SCE} relative to the OCP [5].

Metallic implants are deemed to be corrosion resistant, and the rate of ion transfer establishes the effectiveness of their passive layer. In this way, TMZF alloys in a physiological environment with i_{pass} lower than 12.5 μA.cm^{-2} or corrosion rate lower than 10^{-1} mm/year are considered belonging to the “Stable” corrosion resistance category and lower than 1.25 μA.cm^{-2} or 10^{-2} mm/year are placed in the “Very stable” resistance class [85].

Figure 4.12 shows the i_{pass} values and the corrosion resistance category for the different surface treatments in different immersion time. Untreated specimens show moderate-low and stable results with i_{pass} closer to 2.0 μA.cm^{-2}, during the different periods analyzed, due to the presence of a homogenous and thin passive layer on the alloy´s surface.

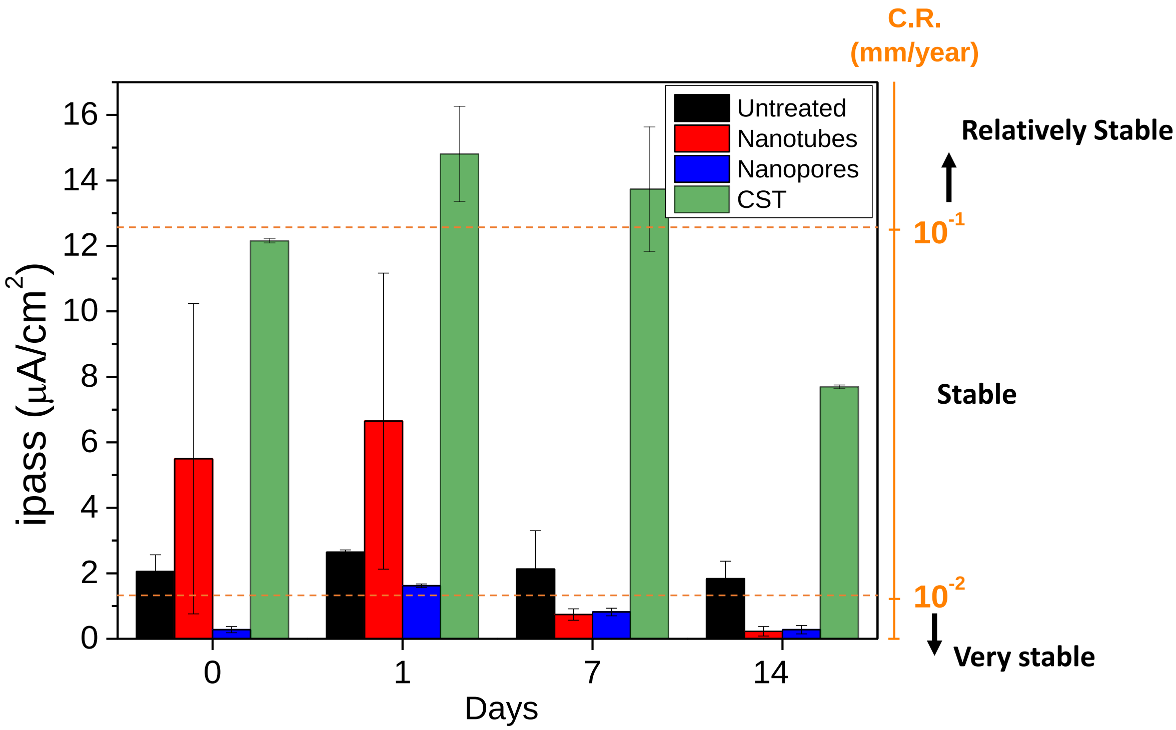

Figure 4.12 Electrochemical measurements of passivation current density (i_{pass}) and corrosion rate (C.R.) of TMZF alloy untreated and treated with nanotubes, nanopores, and CST in different immersion time in SBF at 37°C.

Initially, for 0 and 1 day of immersion, nanotubes samples showed high i_{pass} values, around 5.0 μA.cm^{-2}. This behavior could be attributed to surface heterogeneities created during the anodization process. Nonetheless, after 7 and 14 days, the i_{pass} values were lower than 0.8 μA.cm^{-2}. Initially, ordered nanotubes offered a free path for ion diffusion between the bulk electrolyte and the electrode, after a few days of immersion these channels begin to close by the deposition of calcium phosphate on the outer and bottom part of the nanotubes, with additional growth of the inner passive film [86], which could have hindered the transfer of ions through these channels. This discussion will be taken again in section 4.3.3.

Nanopores samples exhibited good electrochemical behavior with low and stable i_{pass} values during all immersion periods, with i_{pass} values lower than 0.3 μA.cm^{-2} after 14 days soaked in SBF. This performance is due to its homogeneous passive layer; this layer is thicker than the passive layer for the untreated samples.

From an electrochemical point of view, samples with CST showed the least corrosion resistance among the four systems studied for the different immersion times, showing i_{pass} values higher than 12 μA.cm^{-2} for 0, 1 and 7 days of immersion in SBF. However, after 14 days, it was possible to see a reduction in its i_{pass} value (~8.0 μA.cm^{-2}) positioning it in the "Stable" resistance category. This chemical treatment produces micro, submicron and nanometer features on the titanium sample. These fine network structures are favorable for accelerating apatite nucleation due to the formation of a sponge-like structure, but consequently, this structure facilitates the diffusion and charge transfer between the electrolyte and the TMZF substrate [87].

The hydroxyapatite formation and electrochemical behavior investigated through potentiodynamic polarization curves of TMZF samples untreated and treated with CST, nanopores and nanotubes, has been studied and the conclusions are summarized in the following paragraphs:

- Surface treatments as nanotubes, nanopores and chemical surface treatment on β-TMZF alloy were successfully obtained.
- Nanotubes and nanopores show a lower and moderate apatite formation (respectively) when compared with CST samples. This behavior could be associated with the reduction of the surface potential due to the formation of oxides of metallic elements present in the alloy as Mo, Zr, and Fe. Thus, decelerating the apatite nucleation.
- On the other hand, CST samples showed the best bioactivity behavior attributed to the high electrostatic interaction between the functional groups on the surface and the ions in the fluid.
- E_{corr} values reveal that nanotubes and nanopores show a nobler behavior than untreated and CST samples, indicating a more stable and protective surface.
- Although nanotubes and nanopores surfaces showed moderate passivation currents values in the early stages of immersion (0 and 1 day), densification processes of the oxide film and deposition of calcium phosphates improve their corrosion resistance, reducing the i_{pass} values, close to 0.2 μA.cm^{-2} after 14 days immersed in SBF.

4.2 Analysis and modeling of the impedance spectra for the different surface conditions obtained

In recent years, Electrochemical Impedance Spectroscopy (EIS) has been successfully applied to corrosion systems. EIS has been used effectively to measure the polarization resistance and determinate the corrosion mechanisms in different systems. Passive, oxide and porous layers show complex impedance responses and the interpretation of their impedance behavior is not trivial.

Traditionally, the impedance test results are modeled by electrical circuits, through the combination of electrical components such as resistors, capacitors, and inductors; however, it is essential to remark that the way to use these elements must have a physical and electrochemical meaning [88].

More specifically, the objective in this chapter is to study the impedance spectra response for the different surface treatments studied in this thesis, via Electrical Equivalent Circuit (EEC), in order to go further in understanding their electrochemical behavior in physiological medium.

Initially, throughout this chapter, some generalities on the principle of modeling the impedance measurements will be presented. Then, different equivalent circuits proposed in the literature will be reviewed and applied for the EIS data of the untreated and CST samples. Finally, a new model will be developed for the anodized samples and its applicability will be evaluated.

The program used in this study to perform the simulations and adjustments of the impedance parameters is the *Simad* software. It was developed at the Laboratoire Interfaces et Systèmes Electrochimiques (LISE) at Pierre et Marie Curie University (UPMC).

4.2.1 EIS measurements over untreated TMZF samples

In order to complete the electrochemical characterization discussed in Chapter III of the surfaces selected for this study, additional information is obtained from EIS measurements and the interpretation of their data. Figure 4.13 shows the evolution of the Nyquist plots and the Bode diagrams with immersion time in SBF solution of untreated TMZF samples (polished samples); replicate specimens show similar results but are not plotted for better visualization of the diagrams (reproducibility was checked).

Nyquist and Bode representations of impedance measurements of samples without surface treatments are shown in Figure 4.13 (b-d). The data plotted in the figures of this chapter have been corrected by the geometric area (0.283 cm^2) exposed to the electrolyte. Graphics of Figure 4.13b and 5.13d have been corrected for the ohmic resistance or electrolyte resistance (R_e), estimated between 20-30 $\Omega.cm^2$, which was deduced from the high-frequency limit (f = 10^4 Hz).

Nyquist diagram for untreated samples in Figure 4.13c reflected the typical response of a capacitive-resistive or pseudocapacitive system independent of the immersion time. It means that the charge transfer, and therefore the reactions are limited due to the protective behavior of the passive oxide layer [36, 89].

The continuous increase of the impedance modulus |Z| throughout the immersion time suggests that the first two weeks in SBF enhances the corrosion resistance of the untreated samples (Figure 4.13d). This observation is consistent with the E_{corr} measurements (Figure 4.11), which shows a significant increase from the first day of immersion and remains almost constant until 14 days.

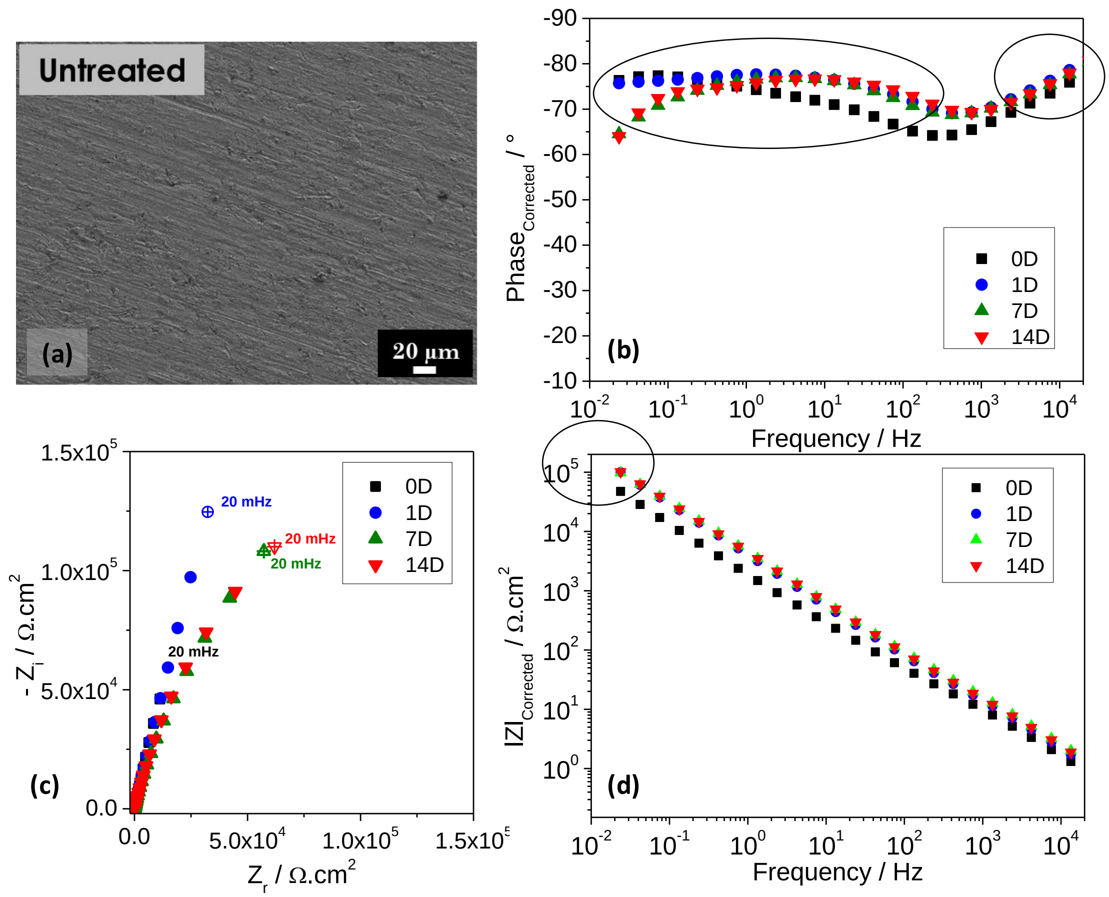

Figure 4.13 a) SEM micrograph of untreated TMZF sample before the immersion period; Iimpedance results for untreated samples immersed in SBF at 37 °C: b) Corrected-phase angle; c) Nyquist plot and d) Corrected-magnitude of the impedance for the different immersion time (0, 1, 7, and 14 days denoted as 0D, 1D, 7D and 14D respectively).

The impedance responses of electrochemical systems can be modeled by analytical expressions and also by EEC. The construction of these circuits consists of combining in series and/or in parallel electrical elements such as resistor (R), capacitors (C) or inductors (L). Note that the element L is indicated here but will not be mentioned again because this phenomenon was not encountered in this study. When the electrochemical responses are not ideal and cannot be represented by a connection of simple R-C-L elements, a Constant Phase Element (CPE) is used. This CPE element indicated the non-ideal capacitive behavior and model the presence of distributed processes [90–92]. The combination and use of these elements depend strictly on the physical aspects of the interface, considering what could happen at this interface.

The most common EEC for the metal /solution interface is the Randles circuit in Figure 4.a, which consists of three elements: a resistor representing the electrolyte resistance, R_e, in series with the parallel combination of a capacitor representing the double layer capacitance, C_{dl}, and a resistor indicating the charge transfer resistance R_{ct} or the polarization resistance R_p in metals that form protective passive layers [50]

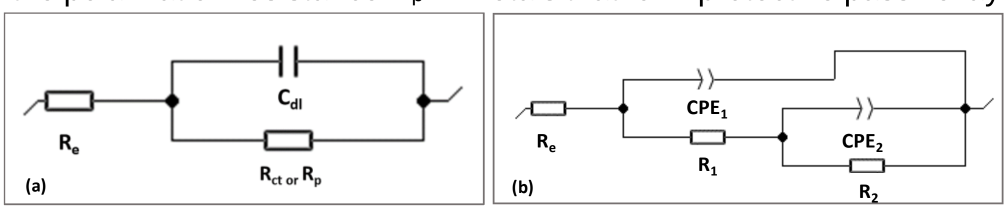

Figure 4.14 Schematic electrochemical impedance circuits: a) Randles circuit and b) porous passive layer circuit.

Another interesting model is shown in Figure 4.14b, for an electrode with a protective porous layer [93]. This circuit uses two times constant, one for the high frequency that characterizes the electrode/coating system and another at low frequencies that characterizes the electrode/aqueous medium system. It is a consequence of the coating having pores or defects through which the electrolyte accesses the electrode base.

To determine suitable results from the impedance analysis is necessary to understand how many processes are happening on the studied surface during the test and then define the adequate model. In this way, using alternative graphical representations of the impedance results as the corrected Bode plots help to define the appropriate EEC [94].

Traditionally, the Bode plot has been particularly useful in recognizing the number of time constants of the system to check the validity of an EEC. These curves are more sensitive to modelling parameters than other traditional impedance plots. Nevertheless, the presence of the electrolyte resistance or ohmic resistance covers the real behavior at high frequencies. For this reason, modified Bode curves corrected from ohmic resistance is used as a reliable option when the solution resistance is not negligible [94]. Therefore, all Bode diagrams in this work were corrected from the electrolyte resistance using Equations 2.20 and 2.21 (Chapter 2).

Over the untreated TMZF surface is expected the formation of a passive bi-layer which has been observed in similar titanium alloys containing zirconium and molybdenum [95]. This passive bi-layer would be composed by an external porous layer and inner barrier layer; thus, it is expected to found two relaxation processes or time constants in the impedance results.

The corrected Bode representations for the untreated TMZF sample are shown in Figure 4.13b and 4.13d. Using the corrected-phase plot, it is possible to observe two time constants present during the impedance test. One of them is in the range of 10^{-2} Hz to 10^{2} Hz and the second one in high frequency around 10^{4} Hz, confirming the theory of the porous passive layer formation indicated above. Thus, the most appropriate EEC for modeling the impedance results obtained for the samples without treatments is the model shows in Figure 4.b.

The principal disadvantage of the corrected Bode phase plot is the need for a precise estimation of the electrolyte resistance. Inaccurate estimations could provide the wrong idea of an additional time constant at high frequencies. Besides that, the corrected curves are very sensitive to the data noise at high frequencies [60]. For these reasons, a complementary curve for the corrected Bode plots is the graphical representation of the effective CPE exponent (α_{eff}), extracted from the imaginary part of the impedance (Z_i) according to [60]:

$$\alpha_{eff}(f) = \left| \frac{dlog\ |Z_i(f)|}{dlogf} \right| \tag{4.1}$$

Traditionally, in the curve of α_{eff}, the CPE elements are associated with plateaus extended during various levels of frequencies. However, these regions can decrease to form bumps or smooth peaks due to the interaction of events with close relaxation processes [60]. In this sense, Figure 4.1515 clearly shows two time constants for all samples, and thus modeled by two CPE, one of them in the range of 10^{-2} Hz to 10^{2} Hz and the second one in high frequency around to 10^{4} Hz.

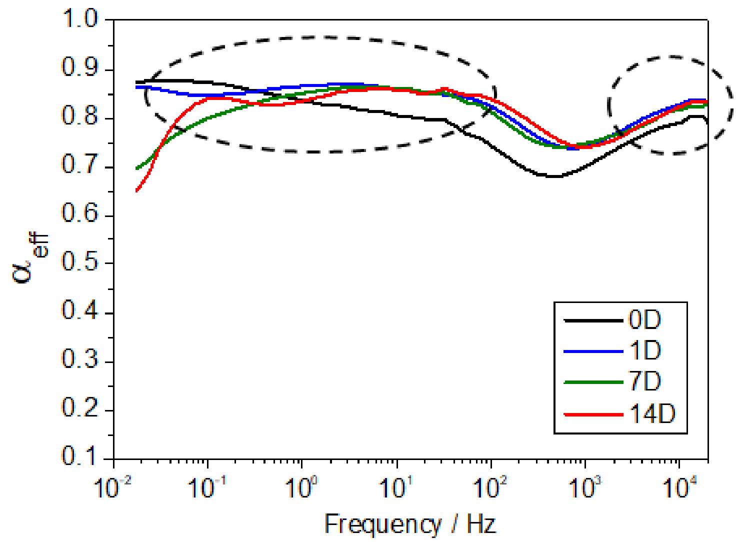

Figure 4.15 Evolution of α_{eff} versus frequency, of the TMZF untreated samples for the different immersion periods (0, 1, 7, and 14 days denoted as 0D, 1D, 7D and 14D respectively).in SBF at 37 °C.

According to the information obtained through the Bode phase and the α_{eff} plots (Figure 4.14b and Figure 4.15), the EEC for the untreated sample will be composed of two relaxation processes, a similar configuration as the EEC shown in Figure *4.*14b. Such characteristic phase pattern may be related to a bi-layered microstructure of the passive films formed on the titanium alloys surface [93, 95].

In this electrical circuit (Figure 4.16), R_e denotes the resistance of the SBF solution, between the working electrode and the reference electrode. The suffix B and OP are associated with the elements that represent the inner barrier layer and the outer porous oxide layer, respectively. The use of a CPE, instead of a pure capacitor was considered due to the assumption of a heterogeneous distribution of charge on the sample surface [59, 95].

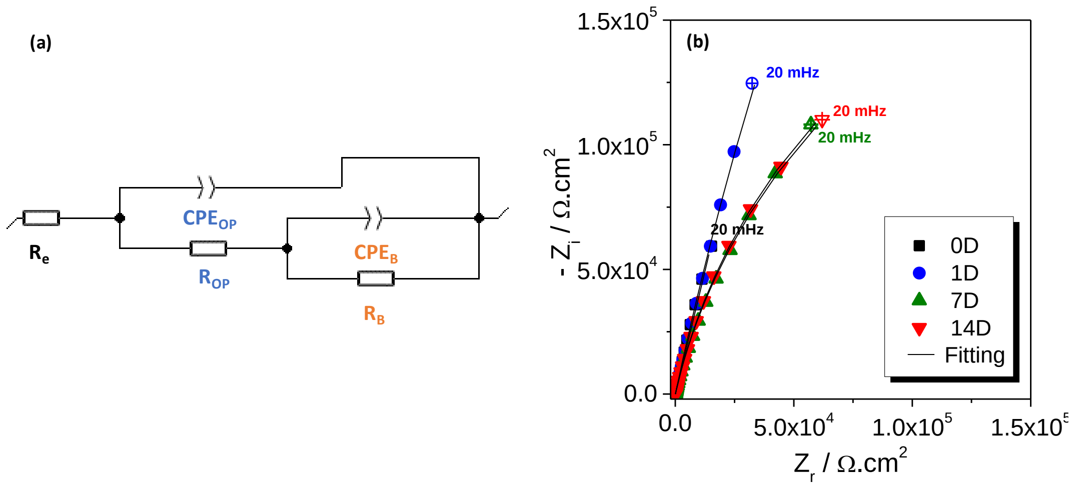

Figure 4.16 Electrical equivalent circuit for untreated samples and b) Nyquist plots of experimental and simulated results obtained through the Simad software, for the different immersion periods (0, 1, 7, and 14 days denoted as 0D, 1D, 7D and 14D respectively) in SBF at 37 °C. The error coefficient was lower than 1% for all the curves.

The impedance of a phase element is defined as $Z_{CPE} = [Q(j\omega)^{\alpha}]^{-1}$. The value of α is related to the heterogeneous distribution of current as a result of the non-uniform surface. The capacitance is Q, while j and ω are the current and frequency, respectively. The resistance, capacitance and α values of the porous and barrier layers, obtained by adjusting the experimental data using the EEC are given in Table 4.2 Electrical parameters obtained by fitting the experimental results of impedance for untreated samples at 37 °C in SBF solution.. The α values of around 0.9 suggest that the behavior of such passive layer approached that of an ideal capacitor, independent of the immersion time [59].

Table 4.2 Electrical parameters obtained by fitting the experimental results of impedance for untreated samples at 37 °C in SBF solution.

Immersion Days	R_e (Ω-cm^2)	Q_{OP} (Ωs$^{-\alpha}$.cm^2)	α_{OP}	R_{OP} (Ω-cm^2)	Q_B (Ωs$^{-\alpha}$.cm^2)	α_B	R_B (10^{5}Ω-cm^2)	*X* (%)
0	23	1.74E-05	0.85	94	1.37E-05	0.83	2.83	0.45
1	20	8.35E-06	0.88	63	6.02E-06	0.84	2.90	0.23
7	21	4.80E-06	0.92	49	8.55E-06	0.81	4.64	0.22
14	20	1.04E-05	0.84	77	2.95E-06	0.88	4.60	0.77

The resistance values, R_B, associated with the inner barrier layer, increases with the immersion days and are significantly larger than the values associated with the outer porous layer, R_{OP}, which remains nearly constant, as Table 4.2 shows. These results indicate that the protection provided by the passive layer is predominantly due to the inner barrier layer, as also observed in other titanium alloys [93, 95, 96].

The Ohmic resistance (R_e), estimated from the proposed model, varies between 20-23 $\Omega.cm^2$ during the immersion days, and is in a good agreement with the one deduced from the high-frequency limit (20-30 $\Omega.cm^2$) from the Bode diagrams (Figure 4.13).

From the values of CPE (Q and α), R_e, and R_{OP}, R_B and using the Brug equation (Equation 2.2), it is possible to obtain the values of the effective capacitance of the passive layer, considering the titanium surface composed by an outer porous layer and an inner compact layer.

$$C_{eff} = Q^{1/\alpha}({R_e}^{-1} + {R_{OP,B}}^{-1})^{(\alpha-1)/\alpha} \tag{4.2}$$

The C_{eff} calculated from the values listed in Table 4.2 for the different immersion periods are ranged from 18 to 9 μF.cm^{-2} for the porous layer and from 12 to 3 μF.cm^{-2} for the inner compact layer, values similar to the observed in the AISI 316L stainless steel immersed in physiological solutions [97, 98]. This capacitance reduction is associated with an increase in the passive layer thickness [75, 99]. Traditionally, low capacitance values are associated with nobler electrochemical behavior [75, 93, 99].

The passive film thickness of the inner compact layer can be calculated from Equation 4.3, which is valid for the parallel-plate capacitor model of a homogeneous oxide layer, associating the overall effective capacitance to the protective oxide layer:

$$d_{ox} = \frac{\varepsilon_r \varepsilon_0}{C_{ox}} \tag{4.3}$$

Where ε_0 is the vacuum permittivity (8.85x10^{-14} F.cm^{-1}) and ε_r is the relative dielectric constant of the material (taken as ε_r = 100, the dielectric constant of TiO_2 [75]). Using this information, it was possible to obtain an approximation of the passive layer thickness for the different immersion days. The passive layer grew with the increase of the immersion days, initially, from 7 nm for non-immersed samples, to 27 nm after 14 days (Figure 4.17).

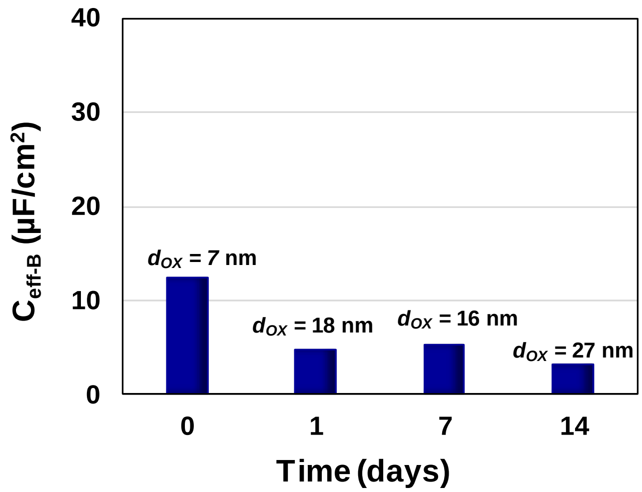

Figure 4.17 Effective capacitances and thickness evolution of the passive inner layer for untreated TMZF samples during different immersion days in SBF solution at 37 °C.

The agreement between experimental and simulated results indicates that the experimental results are well fitted by the proposed equivalent circuit. Error values (X) lower than 1% were found during these EIS data treatments, indicating a satisfactory fitting level (Table 4.2) [75].

4.2.2 EIS measurements over TMZF samples treated with HCl and NaOH

A similar study to that conducted in section 4.1 was carried out on the CST samples. Electrochemical impedance spectroscopic measurements were employed to investigate the changes on the chemically treated surface after different immersion time in SBF solution (0, 1, 7 and 14 days).

The effect of the immersion periods through impedance curves for the acid and alkali treated samples is presented in Figure 4.18. The evolution of the overall impedance in the Nyquist plots displays semicircles arc flattened at low frequencies. The radius of these arcs decreases with the increase of immersion time (Figure 4.18c).

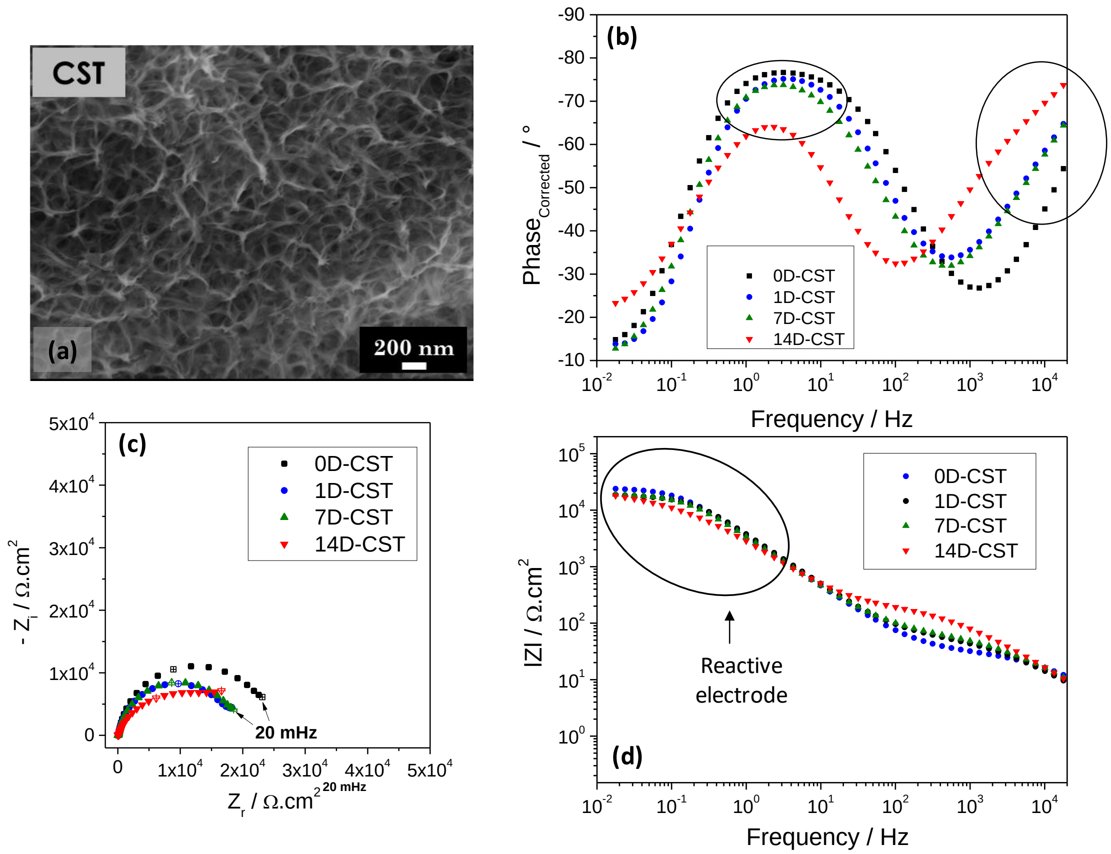

Figure 4.18 a) SEM micrographs of CST TMZF samples before the immersion periods; Schematic representation of the impedance results for CST samples immersed in SBF at 37 °C during the different periods (0, 1, 7, and 14 days denoted as 0D, 1D, 7D and 14D respectively): b) Corrected-phase angle; c) Nyquist plot and d) Corrected-magnitude of the impedance.

Figure 4.18 (b and d) shows the Bode curves of treated TMZF samples soaked in SBF for different immersion times. Samples without previous immersion or on zero days (0D), exhibit a progressive increase of the phase angle from high to middle frequencies, with a variation of the phase angle from -54° to -27°. After that, the phase achieved a minimum value of -74° in the frequencies between 10^0 Hz – 10^1 Hz and remained approximately constant. The behavior mentioned above can be associated with the sodium titanate layer formed on the substrate during the CST; this layer is considered low capacitive owing to its porous constitution. Then, reducing ever more the frequencies is possible to observe a new increment of the phase angle until reaching a value of approximately -15°.

A uniform variation in the phase angle curves is observed with the increase of immersion periods. At intermediate frequencies, it was observed a slightly reduction in the phase angle in samples 1 and 7 days of immersion, compared with samples without previous immersion. This behavior was associated with the precipitation and growth of the first nucleus of calcium phosphate on the sample surface. In the same region, after 14 days of immersion, the plateau appeared in a higher phase angle around -62°. After 1 and 7 days of immersion, the phase angle increase with the reduction in frequency attaining a value around -12° at the lowest frequency. Similar to the behavior observed in 0 days. However, after 14 days the angle achieved a lower value, -23°, at the same frequency.

Similar behavior to the above mentioned has been attributed to the presence of a porous layer accompanied by the formation of a new layer. The porous layer can be associated with the gel sodium titanate layer, and the formation of the new layer, to the hydroxyapatite layer grown [84].

Hodgson et al. [100] associated the interaction between the ions present in the physiological solution and the electrode surface with a change in the phase angle at the frequencies region in the Bode curves. Relating these variations to a physical change in the sodium titanate layer present on the CST samples.

As shown in Figure 4.13d, untreated TMZF samples exhibited a performance similar to a blocking electrode, characterized by a slope value of -1 at all frequency. However, independent of the immersion period, the CST samples behave differently and show plots with magnitude smaller than unity at the lower frequency region (Figure 4.d). Indicating a behavior typical of a more reactive electrode [59].

The modified Bode representations for the CST sample are shown in Figure 4.b and d, Using the corrected-phase plot (Figure 4.b), two relaxation processes or time constants present during the impedance test are possible to be determined. It can be observed that the two constant phase angle regions for the chemically treated samples are smaller compared to the constant region of the untreated titanium alloy. This short distribution of the time constants indicates a less protective and homogeneous surface.

Effective CPE exponent (α_{eff}) plot is used for a better characterization of the relaxation process occurring over the surface of chemically treated samples. Figure *4.*19 shows a similar behavior at high and intermediated frequencies on the corrected-phase plot. Nevertheless, this plot shows an additional bump at low frequencies (10^{-2} Hz to 10^{-1} Hz), This interesting behavior was associated with an extra relaxation process.

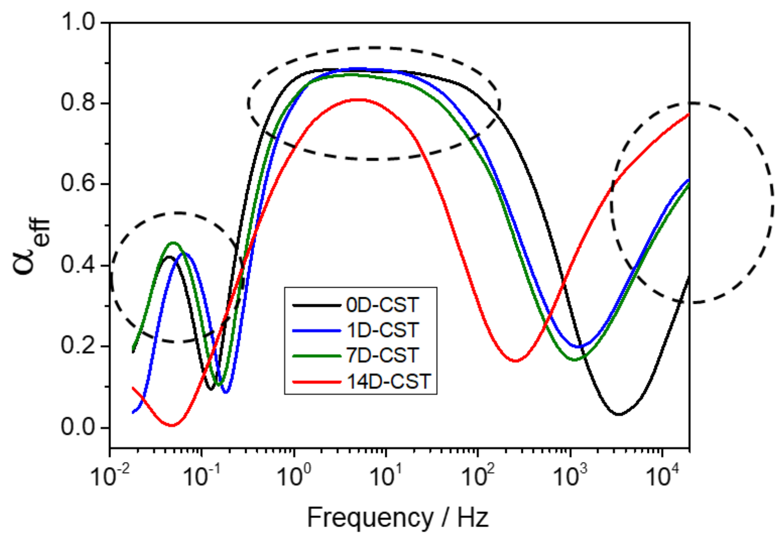

Figure 4.19 Evolution of α_{eff} versus frequency, of the CST TMZF samples for the different immersion periods (0, 1, 7, and 14 days denoted as 0D, 1D, 7D and 14D respectively) in SBF solution at 37 °C.

According to the information obtained from the α_{eff} plot, this third relaxation process is attributed to a diffusion phenomenon, which is typically revealed during low-frequency disturbances during the impedance measurements [101]. Initially, it was thought to use a Warburg element to model this phenomenon, due to values of the effective alpha close to 0.5, However, the values of the obtained parameters were outliers and the results were not satisfactory due to high fitting errors. Therefore, an extra CPE element was indicated, related to a general diffusion element.

Over the CST is expected to find three relaxation processes acting during the impedance test, one more than the two found in the untreated samples, and it is associated with the external sodium titanate layer created during the chemical treatment with HCl and NaOH.

As mentioned above and confirmed by the information obtained from the Bode phase and the α_{eff} plots, the EEC for the CST TMZF samples shall be composed of three relaxation processes. The circuit is shown in Figure 4. and provides a good representation for systems with a compact inner layer, an intermediate porous oxide layer and an outer gel sodium titanate layer.

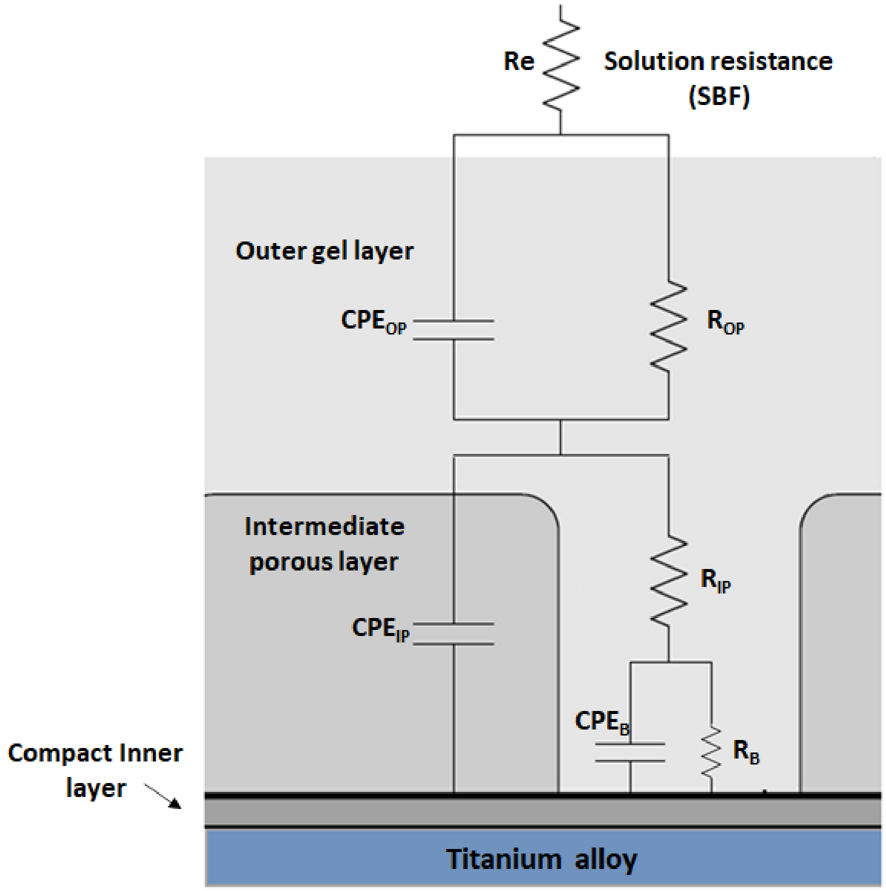

Figure 4.20 Equivalent circuit for CST TMZF samples (Adapted from [59]).

In the electrical circuit of Figure 4.20, R_e represents the electrolyte resistance (SBF solution), R_{OP} and CPE_{OP} represent the resistances and the capacitances of the outer porous layer, associated with the gel sodium titanate layer dissolution and the HAp growth. R_{IP} and R_B are the resistances of the intermediate porous oxide layer and the inner barrier layers, and the CPE_{IP} and CPE_B are used to designate the capacitances of the outer porous layer and the compact inner layer, respectively.

The Nyquist representation of the fitting EIS data for CST samples is shown in Figure 4., and the simulated curves were modeled through of the EEC presented in Figure 4.20. The errors measured (X) for the experimental and simulated data were lower than 1% independently of the immersion period, indicating a satisfactory fitting level.

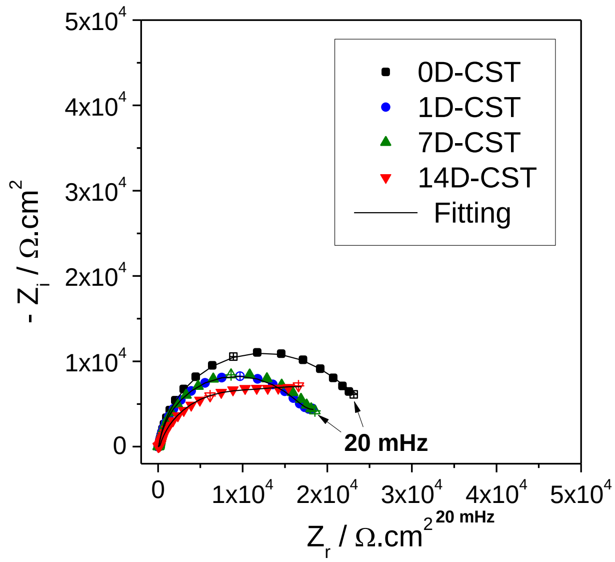

Figure 4.21 Nyquist plots of experimental and simulated results obtained through the Simad software, for the CST samples immersed in SBF at 37 °C during the different periods (0, 1, 7, and 14 days denoted as 0D, 1D, 7D and 14D respectively).

The electrochemical impedance parameters as resistance, capacitance and α values of the porous and barrier layers obtained from the equivalent circuit are displayed in Table 4.3.

Table 4.3 Electrical impedance parameters obtained by fitting the experimental results of CST samples immersed in SBF at 37 °C for the different periods 0, 1, 7 and 14 days.

Immersion Days	R_e (Ω.cm²)	Q_{OP} (Ωs$^{-α}$.cm²)	$α_{OP}$	R_{OP} (Ω.cm²)	Q_{IP} (Ωs$^{-α}$.cm²)	$α_{IP}$	R_{IP} (Ω.cm²)	Q_B (Ωs$^{-α}$.cm²)	$α_B$	R_B (Ω.cm²)	C_{effB} (μF/cm²)	*X* (%)
0	25	8.61 E-04	0.57	35.05	3.31 E-06	0.71	819	1.69 E-05	0.91	48562	32	0.39
1	21	2.79 E-04	0.55	50.14	6.66 E-06	0.72	283	1.39 E-05	0.95	16366	29	0.26
7	24	3.30 E-04	0.53	112.33	9.28 E-06	0.60	283	2.46 E-05	0.84	11916	22	0.71
14	23	1.45 E-04	0.80	178.97	4.08 E-06	0.76	155	1.81 E-05	0.85	11513	18	0.82

With the increase of the immersion days from 0 to 7 days, the Q_{OP} values decreased showing a dissolution process of the gel sodium titanate layer. This might be associated with the interaction between the ions present in the physiological solution and the ions in the titanate layer [86].

Between 7 and 14 days in the SBF a mature HAp layer arises from the complete dissolution of the sodium titanate layer, which acts as a diffusion barrier corroborate by the higher $α_{OP}$ value at 14 days. This behavior is confirmed in the

Nyquist spectrum at 14 days of immersion (Figure 4.21), where it is possible to see a semicircle arc smoothed at low frequencies [86].

The resistance R_B decreased continuously, and at the same time, the R_{OP} increased with the immersion days, attaining a constant value between 7 and 14 days. This behavior can be associated with the continuous dissolution and formation processes of the barrier layer and the HAp layer, respectively [86].

Previous investigations employing Auger emission spectroscopy confirmed the presence of an oxide film between the sodium titanate layer and the titanium surface [102, 103]. Through the impedance results and employing the Equation 4.2 and the fitting results C_{effB} from Table 4.3, it is possible to calculate an approximation value of the titanium oxide inner layer thickness, whose values are summarized in Figure *4.*.

CST samples without immersion in SBF showed a thinner compact layer compared with the untreated samples in the same condition. During acid etching with HCl, the thin passive titanium oxide layer dissolves to form TiH_2; immediately after, in contact with air moisture, a new titanium oxide layer is formed. However, this layer is thinner than the initial one [31, 104, 105]. Similar to the untreated samples, the passive layer on the CST samples grew with the increase of the immersion days (Figure 4.).

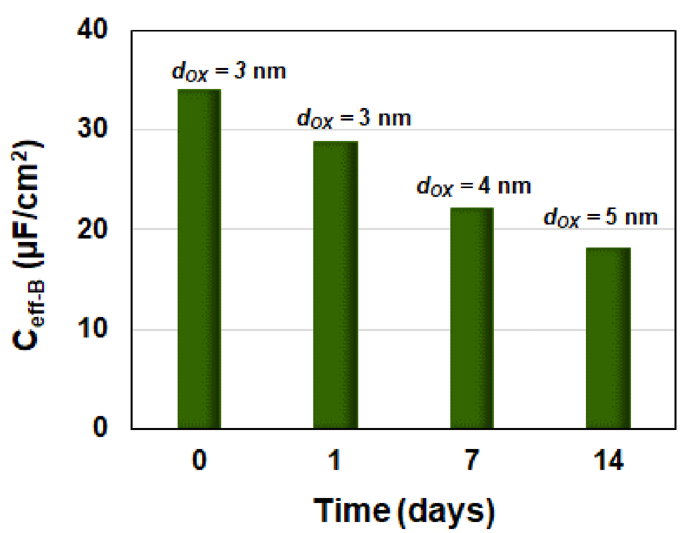

Figure 4.22 Effective capacitance and thickness evolution of the passive inner layer for CST TMZF samples during different immersion days at 37 °C in SBF solution.

4.2.3 EIS measurements over anodized TMZF samples

Electrochemical impedance spectroscopic results were employed to investigate the changes in two different anodized systems (nanotubes and nanopores surfaces) after different immersion periods in SBF solution (0, 1, 7 and 14 days).

High-resolution SEM image in Figure 4. shows the surface condition of the TMZF samples with nanotubes before the immersion periods. Initially, it was analyzed the electrochemical evolution of the nanotube samples through the Nyquist plots and the Bode diagrams shown in Figure 4. (b-d).

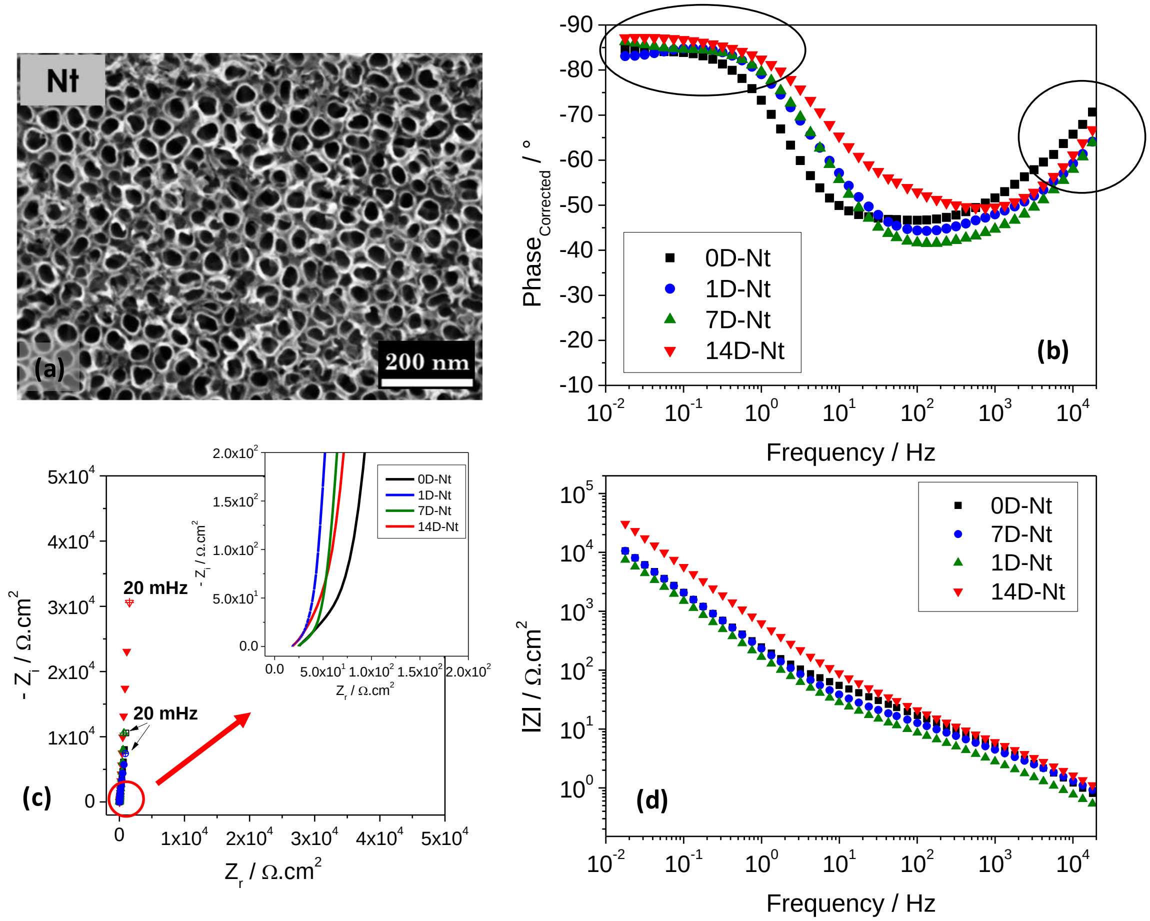

Figure 4.23 a) SEM micrographs of nanotubes TMZF sample before the immersion periods; impedance results for nanotubes samples immersed in SBF at 37 °C for the different periods (0, 1, 7, and 14 days denoted as 0D, 1D, 7D and 14D respectively): b) Corrected-phase angle; c) Nyquist plot and d) Corrected-magnitude of the impedance.

Observation of the Nyquist diagrams reveals that regardless of the immersion time studied, the shape of the CST impedance spectra (arc) is typical of a reactive system (section 4.2), whereas in Figure 4.(c) the samples with nanotubes are apparently rather purely capacitive (straight line), or at least pseudocapacitive (inclined straight line). This means that the faradaic reactions are very limited [59].

These anodized samples showed a particular behavior in the Nyquist diagram, observing an inclined straight line or an arc at high frequencies range (Enlarged region Figure 4.23c) and a capacitive or pseudocapacitive branch at low frequencies. This is a typical characteristic of a porous electrode, as will be demonstrated in section 4.2.3.3.

The corrected Bode phase angle plots of TMZF samples with nanotubes immersed in SBF are shown in Figure 4.(b). At low and middle frequencies (10^{-2} Hz to 10^{1} Hz), the phase angle remains almost constant, presented with values approaching -90° which is the typical capacitive behavior of a compact oxide film. The protective character of this film seemed to be enhanced with increased immersion, indicating a more protective behavior after 14 days.

With the further increase in frequency, the phase angle progressively increased to the highest value close to -45° and decreased again at the higher frequencies zone. Thus, two relaxation processes or time constants were identified from the Bode phase angle plot. One of them is in the range of 10^{-2} Hz to 10^{1} Hz and the second one at a high frequency around to 10^{4} Hz Figure 4.(b).

Figure 4.(d), shows the modulus of impedance for nanotubes samples, showing a similar behavior for all the immersion days, separated by two distinct zones. Between low and middle-frequency (10^{-2} Hz – 10^{1} Hz), the curves exhibited a constant linear slope close -1, less inclined than the slope at high-frequency, around to -0.5. This behavior is characteristic of capacitive surfaces [84].

Figure 4. shows the evolution of the Nyquist plots and the Bode diagrams with immersion time in the SBF solution, for the TMZF samples with nanopores. Additionally, in Figure 4. (a) is possible to see the surface condition of the nanopores TMZF samples before the immersion periods.

Similar to the nanotubes, nanopores specimens show a capacitive or pseudocapacitive behavior, which was observed in the Nyquist diagram independently of the immersion time studied (Figure 4.(c)). These curves are typically observed in low reactive porous systems.

Observing the enlarged region in Figure 4.(c), the nanopores samples showed the same behavior of a porous film over a conductive substrate [106], with a straight line at ~ 45°at high frequencies, with a capacitive straight line corresponding to the capacitance of the pore wall [107].

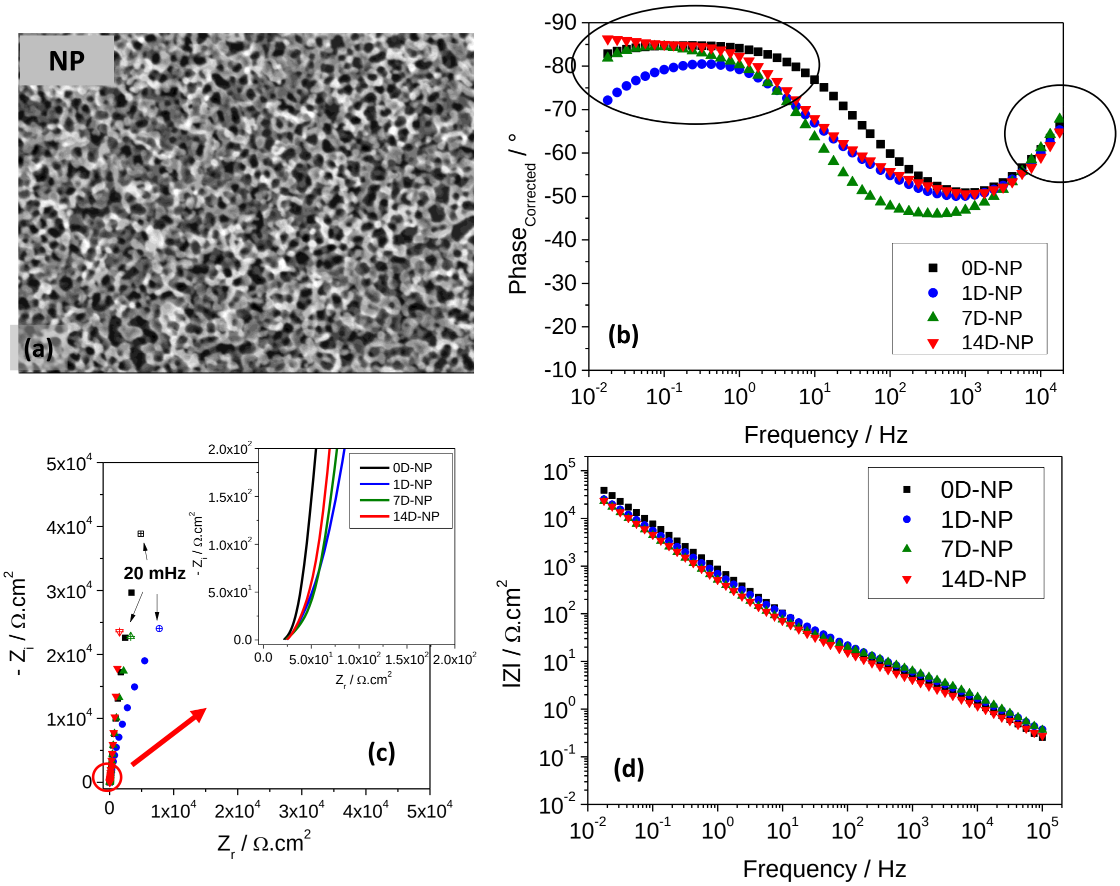

Figure 4.24 a) SEM micrographs of nanopores TMZF sample before the immersion periods; Schematic representation of the impedance results for untreated samples immersed in SBF at 37 °C during the different periods (0, 1, 7, and 14 days denoted as 0D, 1D, 7D and 14D respectively): b) Corrected-phase angle; c) Nyquist plot and d) Corrected-magnitude of the impedance.

The corrected Bode phase representations of nanopores TMZF samples immersed in SBF are shown in Figure 4. (b). Here, two relaxation processes are present during the impedance test. One of them in the range of 10^{-2} Hz to 10^{1} Hz in values approaching -90°and the second one in high frequency around to 10^{4} Hz.

Figure 4.24 (d) shows the Bode impedance plot of TMZF samples anodized with nanopores and after immersion periods in the SBF solution. Independent of the soaking time, all samples showed a stable behavior, characterized by two slopes with a slight tilt between them. One of them, is at the low-intermediary frequency region (10^{-2} Hz to 10^{1} Hz) and the second one, between the intermediary and high frequency (10^{1} Hz – 10^{4} Hz). This behavior is similar to the one observed by nanotubes.

Graphical representations of the α_{eff} (Figure 4.25) were built to determine the number of time constants present during the impedance tests to help us choose the more appropriate EEC system to fit the result of the anodized samples (Nt and NP). Figure 4.25 shows two-time constants for the Nt and NP samples whatever the immersion time.

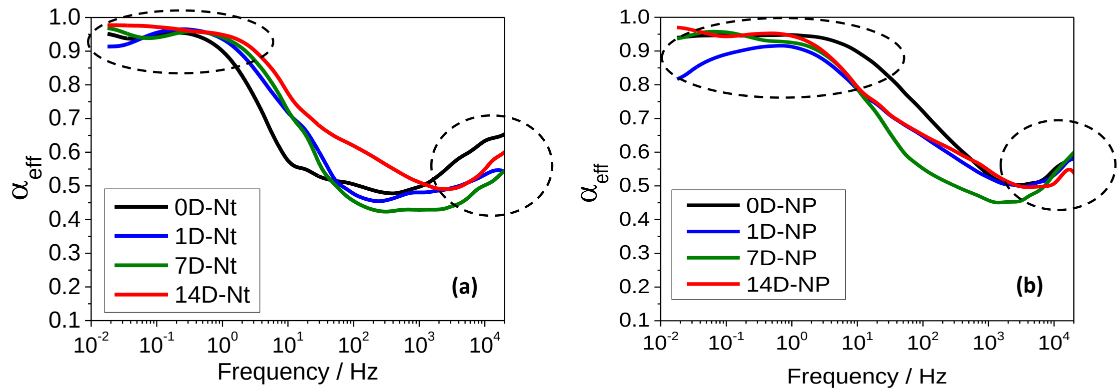

Figure 4.25 Evolution of α_{eff} with the frequency of the anodized TMZF samples for the different immersion periods (0, 1, 7, and 14 days denoted as 0D, 1D, 7D and 14D respectively) in SBF at 37 °C: a) nanotubes and b) nanopores.

According to the information obtained through the Bode phase and the α_{eff} plots, initially, the anodized samples were fitted considering a similar electrical circuit as the one used for untreated samples, Figure 4.14b, which is related to passive film with bi-layered microstructure. However the fitting results for both anodized conditions were not satisfactory as already mentioned in different works [75, 108]; the adjustment errors are large and the values of the parameters obtained are outliers.

4.2.3.1 Analysis of the electrical models proposed in the literature

Various equivalent electrical circuits have been suggested to model the impedance response of anodized titanium surfaces [60, 109–113]. The first explanation for this may lie in the diversity of experimental conditions, for example, the temperature, the position of the electrodes, the nature of the electrolyte, etc. In the case of anodized samples, the measurement can also be very sensitive to the topography and the crystal structure of the surface, and also to the ambient luminosity. Indeed, TiO_2 being a photosensitive semiconductor, its electrical response depends greatly on light [114]. As mentioned in Chapter II, in this thesis, the impedance measurements were conducted in a dark environment to reproduce the conditions of the human body.

Figure 4.26 presents the electrical circuits with two relaxation processes most frequently found in the literature to model the impedance response of the anodized titanium surfaces. Model (a) shows a circuit with two time constants in series widely used. In this model, R_o and Q_o are respectively attributed to the resistance and the pseudo-capacity of the external porous layer while the elements R_b and Q_b model the internal barrier layer [110, 111].

On the other hand, a model with three time constants combining cascade and parallel sequences is introduced [60, 109], where Q_o represents the capacitive contribution of the nanotubes walls, R_{ep} is the resistance of the electrolyte in the pore, R_i and Q_i are associated with the interface at the bottom of the pore and finally Q_b and R_b model the barrier layer (Figure 4.26 b).

Finally, some authors have also proposed to introduce an element of Warburg (W) into their electrical circuits associating it with a diffusion impedance as reported in the models (c) and (d) [112, 113]; however, the experimental impedance results for nanotubes and nanopores samples analyzed in the present thesis did not show characteristics of a Warburg element.

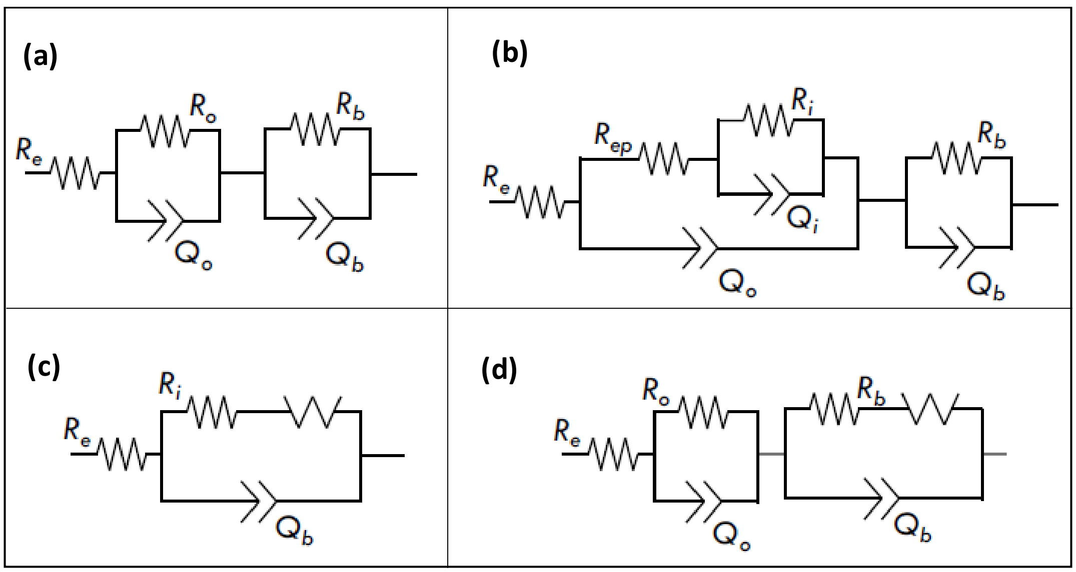

Figure 4.26 Graphical representation of the EEC most frequently used for modeling the impedance results of anodized titanium samples.

In most of the publications cited above, the Nyquist representation presents spectrum in the form of a semicircle (or flattened semicircle, or portion of a semicircle), which is the typical signature of EEC based on R/Q or R/C arrangements. Therefore, this observation justifies the use of EEC like those presented in Figure 4.26 to model the experimental results of the anodized samples.

However, in this thesis work, the Nyquist representations of nanotubes and nanopores are not characterized by semicircles but rather by a line inclined at low frequencies which tends towards infinity and a portion distorted to high frequencies inclined by almost 45 ° (as presented in Figure 4.23 and Figure 4.24).

Therefore, modeling the impedance results of this work with classical equivalent circuits as those mentioned above does not seem relevant. Moreover, the preliminary adjustment tests carried out with the circuits presented in Figure 4.26 were unsatisfactory; the adjustment errors were large (higher than 10% in some cases) and the values of the parameters obtained were atypical.

Thereby, a new model based on a non-classical theory is employed to model the impedance response of anodized TMZF samples in SBF. As mentioned in the Nyquist representations for nanotubes and nanopores samples, these surfaces show similar behavior as the porous electrodes. Similar behavior was described by De Levie [115, 116]. This author modeled the impedance results of a porous electrode through an alternative model describe as the Transmission Line (TL) model.

After the theory described by De Levie, some authors as Bisquert et al. have already shown the TL applicability for the modeling of porous TiO_2 deposits made for solar applications [117, 118]. The model has also been used by other groups to analyze porous film impedance measurements of TiO_2 for photosensitive pigment solar cells [119, 120].

Recently anodized titanium surfaces have been studied through impedance using transmission line models [36, 108]. These studies have shown excellent compatibility between experimental and modeling results, as well as, consistency in the values of the parameters obtained. In this way, the rest of this chapter will be dedicated to the study of the porous electrodes using the TL model, applied to nanotubes and nanopores in a physiological environment.

4.2.3.2 Porous electrode model and transmission line

TL models owe their origin and name to the development of mathematical theory for the performance of submarine telegraph lines. William Thompson showed that an impulse would broaden by the time it reached the other end of the cable, requiring a significant reduction in transmission speed to resolve the pulses. He considered that, because the capacitive coupling would be to the seawater adjacent to the cable, the advent of submarine cables required a more careful analysis of the problem [59].

Thomson modeled a submerged telegraph line as a conducting wire of radius r_1 separated from a conductive ocean by an insulating concentric cylinder of radius r_2 (Figure 4.27), and expressed the capacitance per unit length of the coated wire by:

$$C_{wire} = \frac{2\pi\varepsilon\varepsilon_0}{\ln{(r_2/r_1)}} \tag{4.4}$$

Where ε is the dielectric constant, and ε_0 is the permittivity of vacuum with a value of $\varepsilon_0 = 8.8542 \times 10^{-14}$ F/cm.

Heaviside extended the theory for telegraphy expressing the problem in frequency rather than time domain and including the effect of inductance per unit length of the cable. He later generalized this analysis in terms of transmission lines [59].

An equivalent circuit of a transmission line is given in Figure 4.27 (b), where Z_1 represents the resistance of the wire with units Ω.cm and Z_2 represents the capacitive coupling through the insulating material and the seawater. It is an impedance by a unit length, with unit Ω/cm.

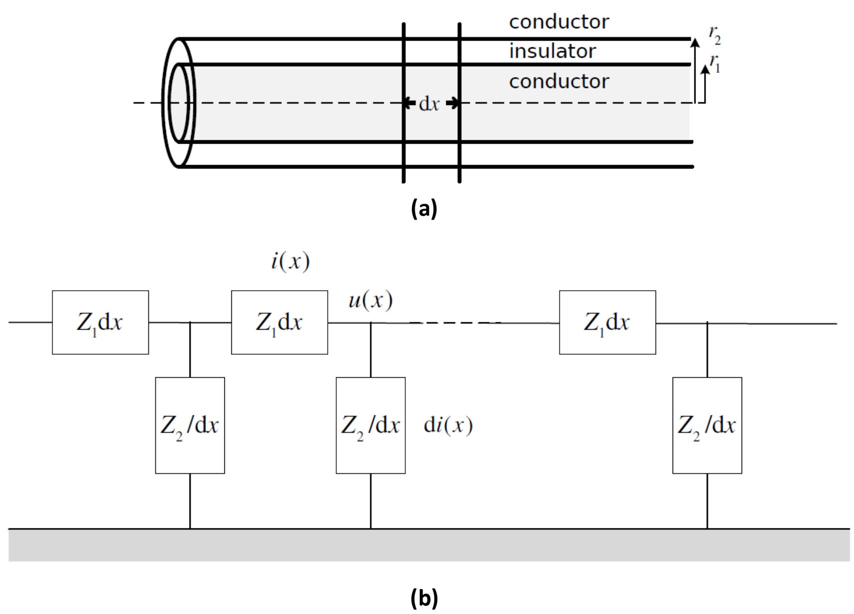

Figure 4.27 Schematic representation of the telegraph cable considered by Thomson and Heaviside: a) representation showing a differential element with length dx and b) elementary components of a transmission line. For system shown in a, $Z_1 = R_0$ and $Z_2 = 1/jwC_{wire}$ [59].

Porous electrodes are used in numerous industrial applications because they have the advantage of an increased effective active area. Figure 4.28 (a) illustrates the random structure of the porous electrode. However, the porous electrode is usually represented by the simplified single-pore model shown in Figure 4.28 (b), in which pores are assumed to have a cylindrical shape with a length ℓ and a radius *r*.

Figure 4.28 (b) displays a graphical representation of the transmission line model, where R_0 is the solution resistance for the pore length, with units of $\Omega.cm^{-1}$,

Z_0 is the interfacial impedance along of the pore length, with units of Ω.cm, expressed in function of the pore radius as:

$$R_0 = \frac{\rho}{\pi r^2} \tag{4.5}$$

And

$$Z_0 = \frac{Z_{eq}}{2\pi r} \tag{4.6}$$

Z_{eq} is the interfacial impedance, and ρ is the electrolyte resistivity. With the restrictive assumption that Z_0 and R_0 are independent of the distance x, de Levie calculated analytically the impedance of one pore to be [121]:

$$Z_{pore} = (R_0 Z_0)^{1/2} \coth(\ell \sqrt{\frac{R_0}{Z_0}}) \tag{4.7}$$

Finally, The impedance of the overall electrode is obtained by accounting for the ensemble of n pores and for the electrolyte resistance outside the pore, i.e.,

$$Z = R_e + \frac{Z_{pore}}{n} \tag{4.8}$$

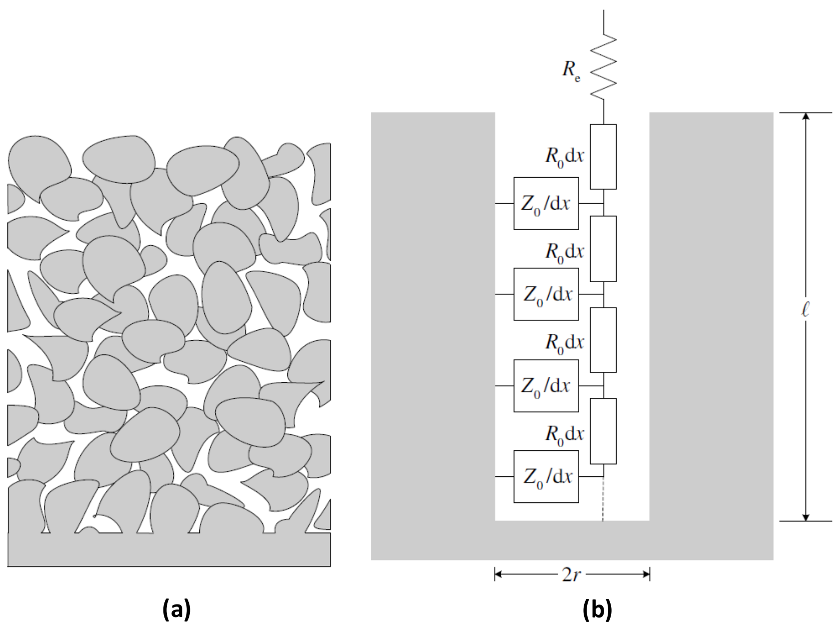

Figure 4.28 Schematic representations of a porous electrode: a) porous electrode with irregular channels between particles of electrode material and b) transmission line inside a cylindrical pore [59].

Subsequently, to explain the impedance behavior of non-ideal porous electrodes Bisquert [106] studied and developed a generalized model involving the concept of the transmission line, using as an important reference point, the work developed by De Levie [121]. Bisquert assumed a configuration that consists of a porous electroactive film deposited on a conducting substrate and dipped in an electrolyte, as is represented in Figure 4.2929.

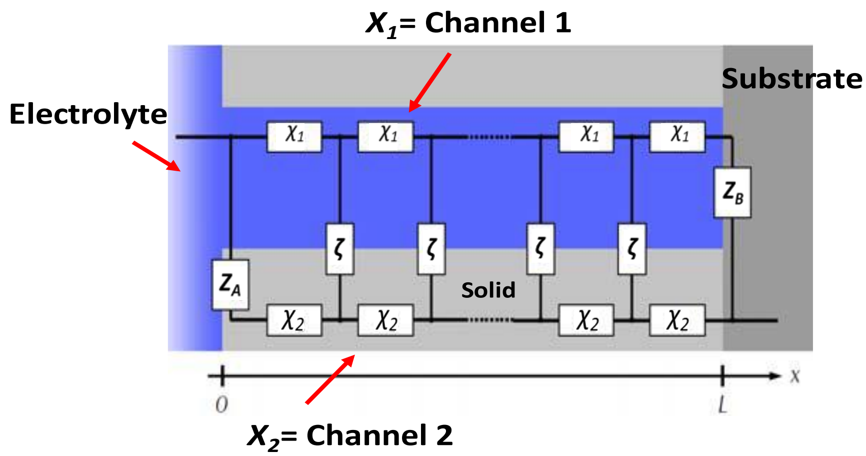

Figure 4.29 Schematic illustration of the inner region (*0* < x < *L*) of a porous electrode divide by a porous film deposited on a conductive substrate. ζ represents the interfacial impedance disposed over the entire porous surface, Z_A is correlated with the impedance of the interface external solution | solid and Z_B is used to describe the interface internal solution | substrate. (adapted from [106]).

Thus, the electrode region is viewed as a mixture of two phases that conduct different species, electronic and ionic, and where the macroscopic boundaries are impermeable to different species. As the porous structure implies a distribution of the current in different directions of space [117], it cannot be modeled by a classic arrangement in series or in parallel of R-L-C elements. The equivalent type of circuit that may apply in this case is a transmission line, as shown in Figure 4.2929.

This TL model is described in Figure 4.2929, with the equivalent circuit modeling the ac behavior of the film. It is considered that exists a freely ionic exchanged between the species into the pores and the bulk solution at the top of the pores (X = 0). Besides, the electronic charge carrier in the nanotubes walls can be interchanged freely at the interface with the titanium substrate (X = L).

In this model, faradaic currents and polarization may occur at the inner surface separating the two phases. Additionally, it is assumed that the elements in the distributed equivalent circuit are homogeneous, independent of the position normal to the plane of the electrode.

Elements X_1 and X_2 describe the local ohmic drop at each point of the transport channels, depending on media conductivity and more generally on transport properties. The element ζ represents the interfacial impedance (internal solution | porous solid). Z_A and Z_B are associated with boundary conditions, more precisely, Z_A is the impedance coming from the interface, external solution | porous solid, while Z_B describes the interface, internal solution | substrate at the bottom of the pores.

The quantities X1 and X2 are impedances per unit length ($\Omega.cm^{-1}$) corresponding to the whole electrode area, and ζ is an impedance-length (Ω.cm) also for the whole electrode area. The full analytical expression for such a transmission line is [106]:

$$Z = \frac{1}{X_1+X_2}\left[\lambda(X_1+X_2)S_\lambda + (Z_A+Z_B)C_\lambda + \frac{1}{\lambda(X_1+X_2)}Z_A Z_B \lambda\right]^{-1}.\Big(L\lambda X_1 X_2 (X_1 + X_2)S_\lambda + X_1[\lambda X_1 S_\lambda + L X_2 C_\lambda]Z_A + X_2[\lambda X_2 S_\lambda + L X_1 C_\lambda]Z_B + \frac{1}{X_1+X_2}\Big[2X_1X_2 + (X_1{}^2 + X_2{}^2)C_\lambda + \frac{L}{\lambda}X_1X_2S_\lambda\Big]Z_A Z_B\Big) \tag{4.9}$$

Where the notations $C_\lambda = cosh(L/\lambda)$, $S_\lambda = sinh(L/\lambda)$, and $\lambda = [\zeta/(X_1+X_2)]^{1/2}$ have been used.

This model is very versatile and, depending on the particular case, can be adapted to attend and simulated the different surface conditions. In this way, the TL model for anodized TMZF samples will be described below.

4.2.3.3 Employment of the transmission line model to the case of anodized TMZF samples in SBF

The TL model suggested in this study to describe the impedance behavior of anodized titanium samples in SBF was applied to two different surface topographies, nanotubes and nanopores.

The TL model illustrated in Figure 4.2929 can be useful for modeling different microstructures and geometries regarding different types of hypotheses. For instance, the geometry indicated above of long cylinders over the substrate or permeable film with irregular geometries or even fine semiconducting particles embedded in a matrix [117]. Additionally, it is necessary to remark that this model involves the volume processes distributed over the whole electrode surface.

Hereafter, it is assumed that quantities X_1, X_2, and ζ are independent of position, meaning that these quantities are only functions of frequency. Additionally, a limit condition for the charge carriers was established, for example, when the electrons reach the external edge of the solid part at x = 0, and when the ions find a wall at x = L. Typically, those hypotheses are defined by the premise that the electric current disappears at the outer part of the porous layer and the ionic current at the end of the liquid channel. This restriction provides a considerable simplification of analysis.

The analysis of the Nyquist diagrams in Figure 4.23 (c) and Figure 4.24 (c) reveals that the two morphologies, nanotubes and nanopores, present a distorted branch at high frequencies and an inclined line at low frequencies. The high-frequency distortion could come from the presence of an influent Z_B pore bottom impedance at the end of a shorted channel or an anomalous transport phenomenon in the resistive channel, e.g., the semiconductor behavior of the TiO_2 layer [117].

In order to build a model in agreement with these observations three hypotheses were defined. The first, consists of admitting that the electrolyte contained in the pores is represented by the resistive channel, X_1, which is modeled by a distributed resistance:

$$X_1 = R_1 \tag{4.10}$$

And thus, the total resistance (Ω.cm) distributed in the resistive channel and normalized by the area is given by:

$$R_1 = L.r_1 \tag{4.11}$$

In the second hypothesis was adopted the anomalous transport formalism to model the channel 2 (solid phase of TiO_2). Thus, X_2 is represented by a parallel arrangement of r_2 and q_2. Indeed, TiO_2 in the anatase form can be assimilated to a moderately doped semiconductor [122]. It is then expected that its crossover frequency be lower than the range of frequencies investigated by impedance in this work. The expression of impedance that describes this behavior is:

$$X_2 = \frac{1}{1 + r_2\, q_2\, (iw)^{\beta}} \tag{4.12}$$

It is pointed out that Equation (4.12) represents an unique transport mechanism taking place in the channel 2 and not the association of a charge transfer phenomenon in parallel with a capacitive phenomenon, as it is normally the case during analysis of impedance results [75, 123].

In the transition region between the internal solution and the pore wall, a potential difference is maintained and is modeled by an interfacial capacitance. Therefore, the third hypothesis proposed that the capacitance of the polarizable interface depends on the frequency and is modeled by a constant phase element or CPE [124, 125].

$$\zeta = \frac{1}{q_3}(iw)^{-n} \tag{4.13}$$

Where q_3 is a constant with dimension F s^{n-1} and the exponent n can be any number in the range $0 < n < 1$. The impedance of Equation 4.13 consists on a tilted straight line in the complex plot, and the total pseudocapacitance (Q_3) describing the interface is defined by:

$$Q_3 = L.q_3 \tag{4.14}$$

Where L is the length of the pores (in cm), associated with the thickness of the nanotubes and nanopores layers (Figure 4.30).

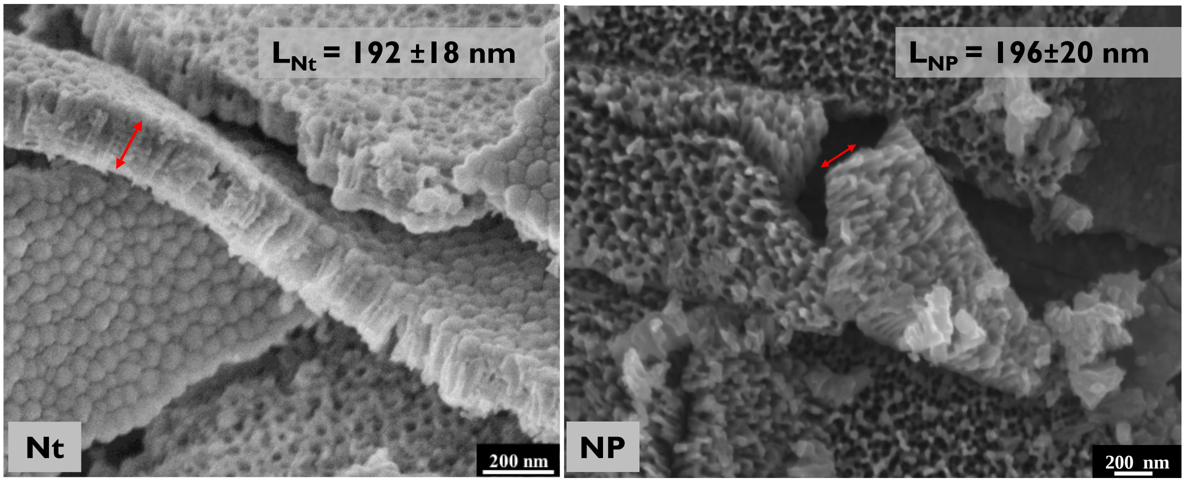

Figure 4.30 Representative SEM images indicating the procedure to obtain the layer thickness of: a) Nanotubes and b) Nanopores.

When the slope at high frequencies is not equal to 1 and 0.5 at low frequencies, the impedance of the boundary condition Z_B (Interface electrolyte/substrate) has to be consider and modeled by a CPE (Q_B). Similar to the capacitive contribution of the ζ.

$$Z_B = \frac{1}{Q_B}(iw)^{-\beta} \tag{4.15}$$

Finally, the last hypothesis assumes that the boundary impedance Z_A (Electrolyte / top of the pores) is modeled by an impedance consisting of a resistance (R_A).

According to the hypothesis established, it was proposed a transmission line model to describe the impedance response of the anodized TMZF samples immersed in SBF at 37 °C during different periods. Figure 4.31 shows a schematic representation of the model. Channel 1 is represented as a distributed resistance, transport in channel 2 is considered anomalous, that is to say, the impedance X_2 is equivalent to a parallel arrangement of a CPE (Q_2) and a resistance (R_2). The interfacial impedance ζ is considered pseudocapacitive (Q_3) and in the limits an impedance Z_B (Q_B) and a resistance Z_A (R_A).

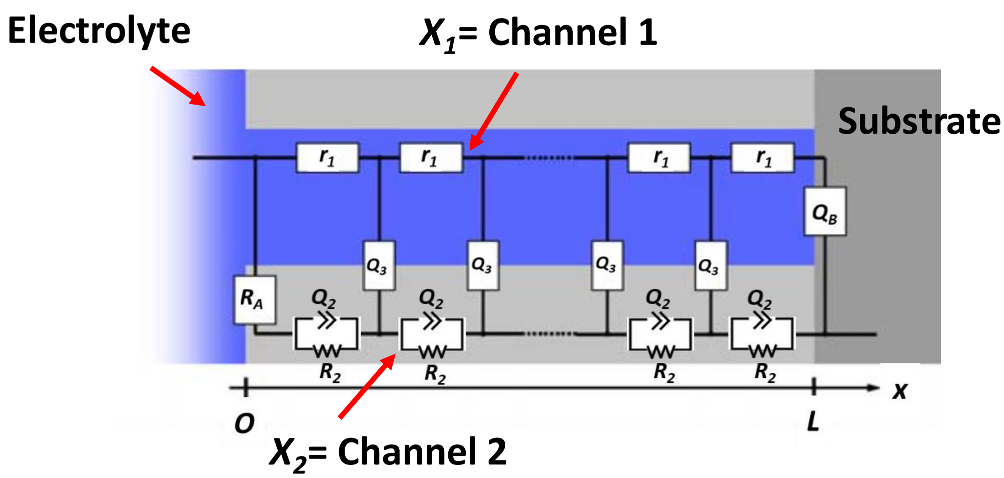

Figure 4.31 The transmission line model proposed to describe the impedance response of the anodized TMZF samples immersed in SBF at 37 °C during the different periods evaluated.

Equation 4.16 shows the solution of the TL employed in this work to model the impedance results:

$$Z = \frac{1}{X_1+X_2}\left[\lambda(X_1+X_2)S_\lambda + (Z_A+Z_B)C_\lambda + \frac{1}{\lambda(X_1+X_2)}Z_A Z_B \lambda\right]^{-1} . \Big(L\lambda X_1 X_2 (X_1 + X_2)S_\lambda + X_1[\lambda X_1 S_\lambda + LX_2 C_\lambda]Z_A + X_2[\lambda X_2 S_\lambda + LX_1 C_\lambda]Z_B + \frac{1}{X_1+X_2}\Big[2X_1X_2 + ({X_1}^2 + {X_2}^2)C_\lambda + \frac{L}{\lambda}X_1 X_2 S_\lambda\Big] Z_A Z_B\Big) \tag{4.16}$$

Where $X_1 = r_1$; $X_2 = \frac{1}{1+ r_2\, q_2\, (iw)^\beta}$; $\zeta = \frac{1}{q_3}(iw)^{-\beta}$; $Z_A = R_A$; $Z_B = \frac{1}{Q_B}(iw)^{-\beta}$

$C_\lambda = cosh(L/\lambda)$, $S_\lambda = sinh(L/\lambda)$, and $\lambda = [\zeta/(X_1+X_2)]^{1/2}$.

Figure 4.32 shows the adjustment results (indicated by a solid line) of the experimental measurements of anodized samples with nanotubes and nanopores using the model proposed in Equation 4.16 and illustrated in Figure 4.31. The TL model is composed of 10 parameters that satisfactorily describes the behavior of the interface. The error between the experimental points and the simulation was lower than 1.0 % independently of anodized morphology and immersion time. Only the nanotube condition after 14 days showed a higher value (1.7%), which is quite reasonable.

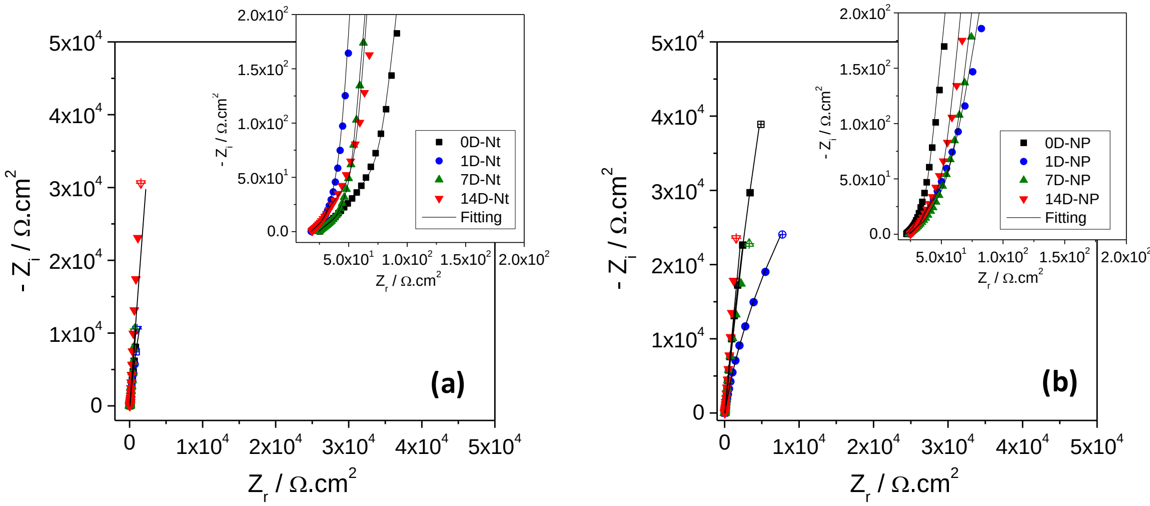

Figure 4.32 Nyquist plots of experimental and simulated results acquired from *Simad* software for the anodized specimens immersed in SBF at 37 °C during different periods (0, 1, 7, and 14 days denoted as 0D, 1D, 7D and 14D respectively): a) Nanotubes and b) Nanopores.

Table 4.4 shows the electrochemical impedance parameters obtained by adjusting the experimental results of nanotubes samples for the different immersion days. Additionally, the values of the crossover frequency (ω_c) that represent the transport mechanism through the channel 2 (X_2) were calculated using 4.17 and showed in Table 4.4.

$$\omega_c = \frac{1}{r_2\, q_2\, (iw)^{1/\beta}} \tag{4.17}$$

Table 4.4 Electrical impedance parameters obtained by adjusting the experimental results of Nt samples.

Days	**X1**	**X2**			**ζ**		**ZA**	**ZB**		**L (cm)**	**ωc (Hz)**	***X* (%)**
	R_1 (Ω.cm)	**R_2 (Ω.cm^2)**	**Q_2 (Ωs^{-e}.cm^2)**	**e**	**Q_3 (Ωs^{-b}.cm)**	**b**	**R_A (Ω.cm^2)**	**Q_B (Ωs^{-n}.cm^2)**	**n**			
0	827	217	6.53 E-07	0.96	1.63 E-04	0.96	7.22 E+06	3.69 E-05	0.91	2.0 E-05	0.035	0.77
1	956	222	4.55 E-07	0.76	2.96 E-04	0.96	2.99 E+05	1.69 E-05	0.84	2.0 E-05	0.023	0.48
7	938	209	6.06 E-07	0.78	3.91 E-04	0.95	4.90 E+08	5.58 E-06	0.92	2.0 E-05	0.019	0.43
14	860	145	2.81 E-06	0.72	9.96 E-05	0.96	5.25 E+09	7.80 E-06	0.89	2.0 E-05	0.003	1.70

The pseudocapacitance values Q_3 varies as the immersion time increases; this could indicate the processes of formation and dissolution of small nuclei of calcium phosphates on the nanotubes walls. Between days 7 and 14, the nucleation process is favored, showing an evident decrease in the interface impedance. Besides, the coefficient b is close to 1, showing homogeneity and stability of the pore walls, independently of the immersion time.

Figure 4.33 was graphed to understand the behavior of the endpoints of the line (Z_A and Z_B) during the immersion days, represented by resistance and capacitance of R_A and Q_B, respectively. The values of R_A and Q_B were obtained from Table 4.4.

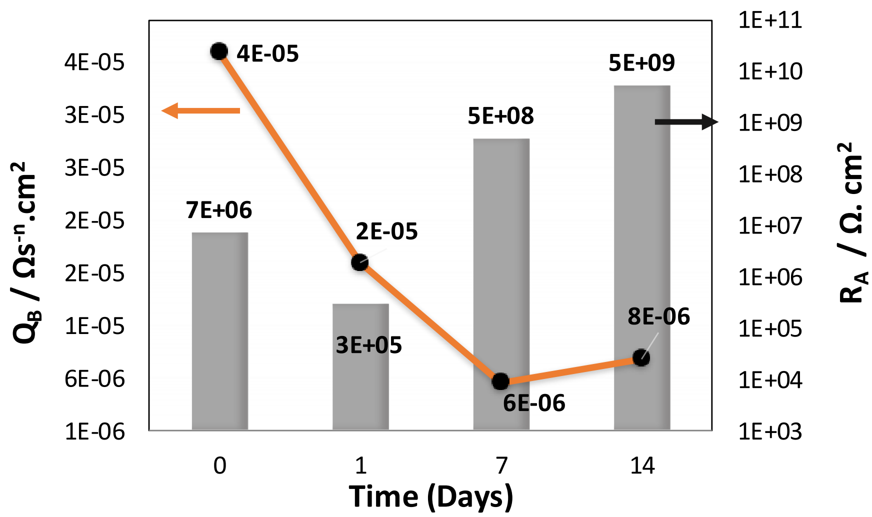

Figure 4.33 Endpoints parameters, R_A and Q_B, obtained from the transmission line model used in nanotubes samples after different immersion periods in SBF.

During the immersion time in SBF, the resistance R_A gradually increases and the Q_B decrease. This behavior could be associated with the formation and growth of calcium phosphate nuclei (Initial step to the apatite formation) on the outer part of the nanotube and the bottom part of the channel. This behavior is observed in Figure 4.34 (red circles). Additionally, the Q_B decrease could be associated with the growth of the inner passive film [86].

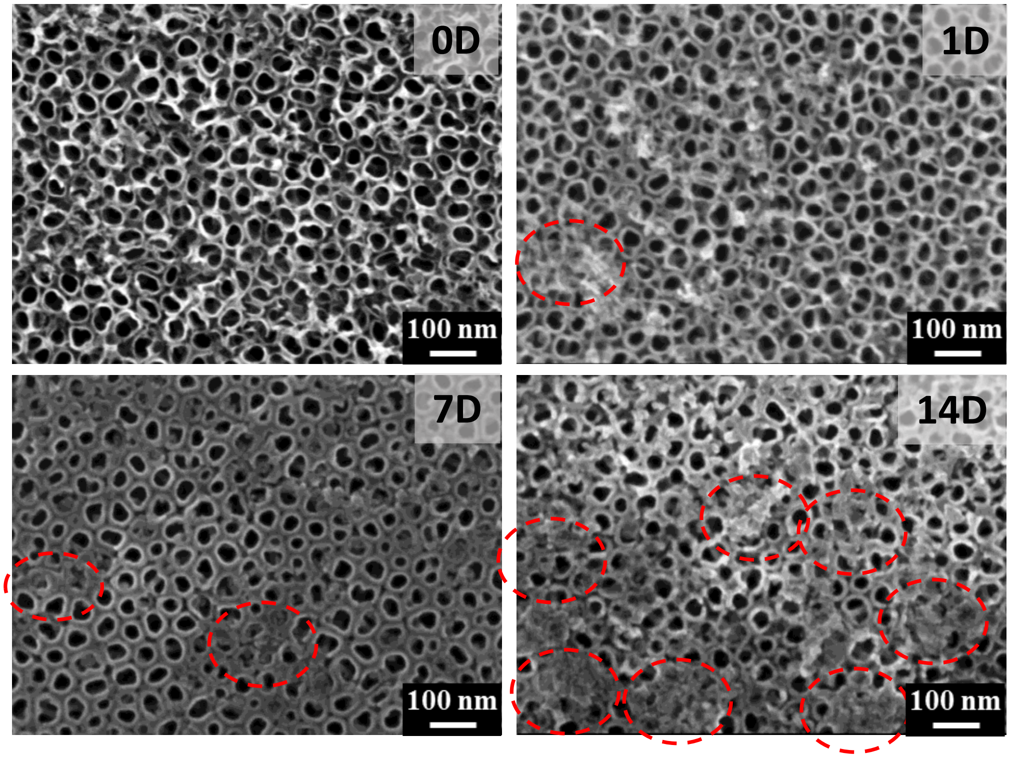

Figure 4.34 Apatite formation over nanotubes samples after different immersion periods in SBF (0, 1, 7 and 14 days).

Table 4.5 shows the electrochemical impedance parameters obtained by adjusting the experimental results of nanopores samples for the different immersion days. Similar to the adjustment for the nanotubes samples, an average value was chosen of L ($2x10^{-5}$ cm) for the nanopores samples. This value was used in the fitting model.

Table 4.5 Electrical impedance parameters obtained by adjusting the experimental results of NP samples.

Days	**X1**	**X2**			**ζ**		**ZA**	**ZB**		**L (cm)**	**ωc (Hz)**	***X* (%)**
	R_1 (Ω.cm)	**R_2 (Ω.cm^2)**	**Q_2 (Ωs^{-e}.cm^2)**	**e**	**Q_3 (Ωs^{-b}.cm)**	**b**	**R_A (Ω.cm^2)**	**Q_B (Ωs^{-n}.cm^2)**	**n**			
0	559	203	8.52 E-07	0.60	7.73 E-05	0.96	1.40 E+06	5.32 E-06	0.90	2.0E-05	0.003	0.60
1	826	207	9.24 E-07	0.64	7.52 E-05	0.97	2.00 E+05	1.15.E-05	0 82	2.0E-05	0.004	0.97
7	787	209	6.06 E-07	0.96	8.68 E-05	0.97	8.83 E+07	9.18 E-06	0.92	2.0E-05	0.004	0.43
14	936	218	6.88 E-07	0.60	7.60 E-05	0.97	4.90 E+08	5.59 E-06	0.89	2.0E-05	0.003	1.00

For nanopore samples, the pseudocapacitance Q_3 values are lower compared to nanotubes and remain almost constant regardless of the immersion time, due to the stable behavior of the interfacial impedance (ζ), even in the first immersion days. Besides, the coefficient b is close to one showing homogeneity and stability of the pore walls.

Figure 4.35 shows the endpoints parameters represented by resistance and capacitance of R_A and Q_B, respectively. These values were graphed to understand the behavior of the transmission line endpoints (Z_A and Z_B) during the immersion days. The values of R_A and Q_B were obtained from Table 4.5.

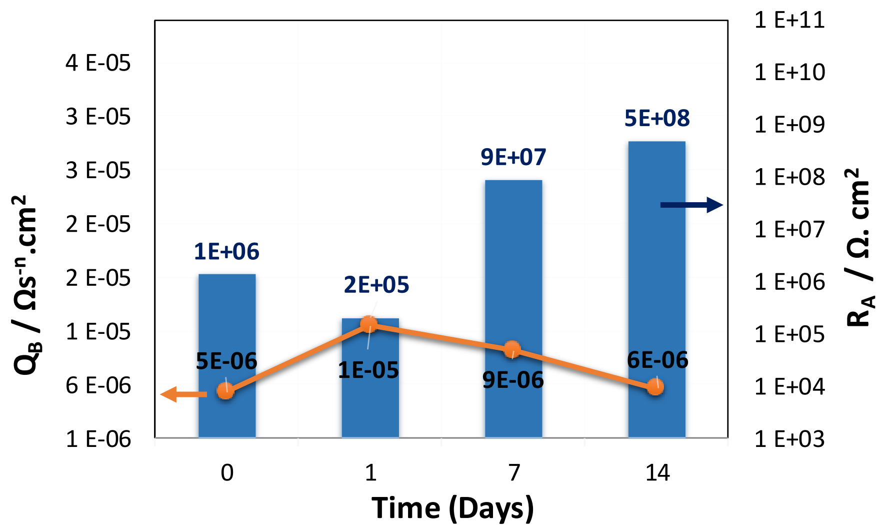

Figure 4.35 Endpoints parameters, R_A and Q_B, obtained from the transmission line model used in nanopores samples after different immersion periods in SBF.

During the immersion time in SBF, the resistance R_A gradually increases. This behavior could be associated with the possible nucleation and growth of hydrated silica gel and amorphous calcium phosphate on the outer and inner parts of the nanopores, both predecessors for the apatite formation [126]. This behavior could be observed in Figure 4.36 (red circles). Moreover, the Q_B values were low and constant indicating a stable and protective behavior of the inner passive film during the entire time analyzed.

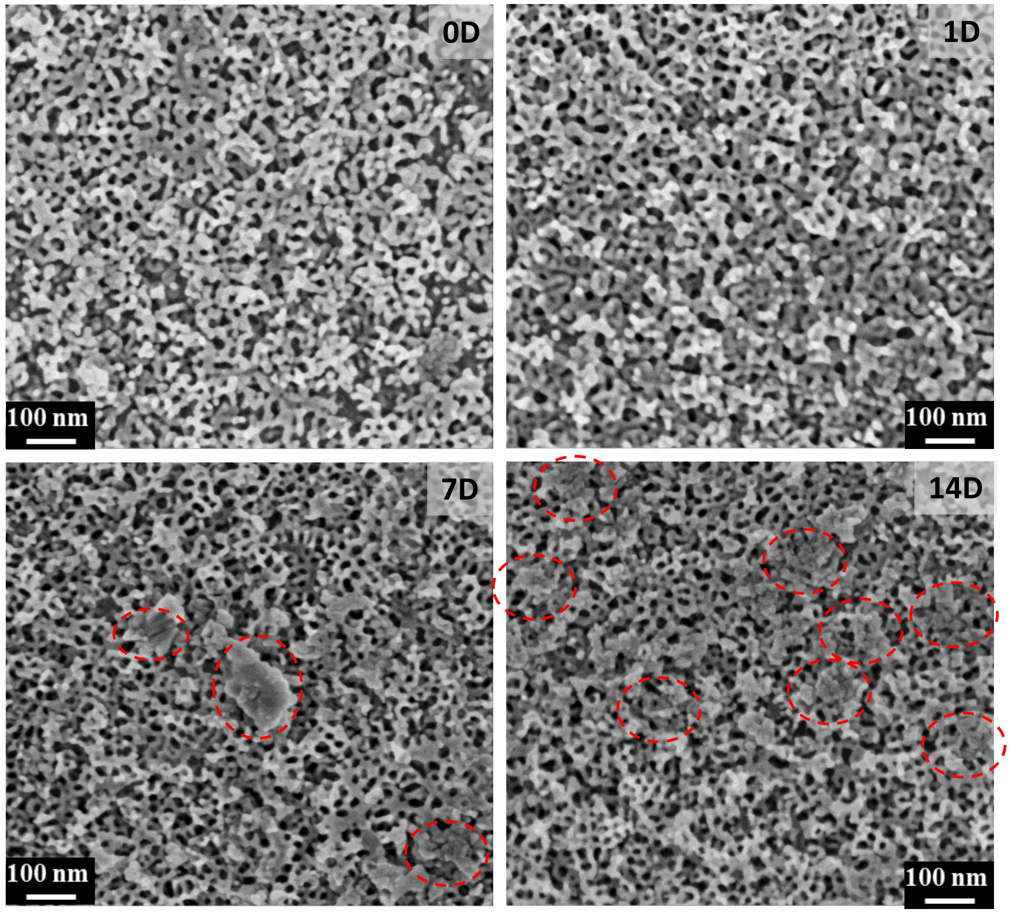

Figure 4.36 Apatite formation over nanopores samples after different immersion periods in SBF (0, 1, 7 and 14 days).

As it was indicated in the transport process in channel 2 (X_2), it is represented by a different model termed as “anomalous transport model” (parallel connection of a Constant-Phase-Element, Q_2, and a resistance, R_2), since the charge carrier transport mechanism depends on the frequency (Equation 4.12). For both anodizing conditions, nanotubes and nanopores, ω_c was between 0.003 to 0.035 Hz. These low values indicated a low charge transfer through the channel 2 in the frequency regime studied in this work (10^{-2} - 10^{4} Hz).

Figure 4.37, summarize the corrosion response and the bioactivity after 14 days of immersion in SBF of the different surface conditions studied in this work; the barrier resistance values (R_B or R_A for the anodized samples) associated with the corrosion resistance obtained from the impedance data, the I_{pass} obtained from the polarization curves and the bioactivity through the mass gain.

Untreated samples showed a good corrosion response indicated by a high resistance value and acceptable I_{pass}, lower than 2 μA.cm^{-2}; however, in this surface condition was not detected HAp formation.

Samples treated with HCl and NaOH contrary to untreated samples, showed excellent bioactivity with the highest mass gain value, around 1.8 mg after 14 days of immersion in SBF. Still, their corrosion resistance was deficient, proved by the lowest R_B and the highest I_{pass} values.

Finally, the anodized samples showed the best corrosion resistance corroborated by the highest and lowest values of R_A and I_{pass}, respectively. On the other hand, specimens with nanotubes and nanopores exhibited low and moderated values of HAp formation after 14 days in SBF.

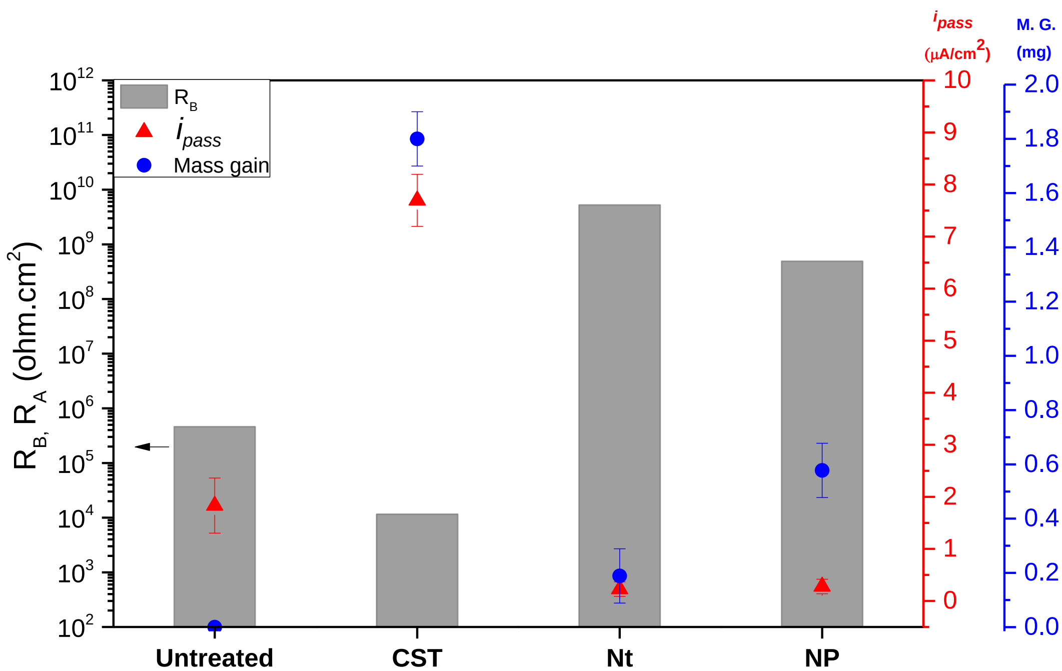

Figure 4.37 Corrosion response and bioactivity of untreated, CST, nanotubes, and nanopores samples after 14 days of immersion in SBF at 37 °C. Barrier resistance (R_B or R_A for the anodized samples) obtained from the impedance data, passivation current (I_{pass}) from the polarization curves, and bioactivity through the mass gain.

Impedance behavior of the four different treated surface samples has been successfully studied and the conclusions are summarized in the following paragraphs:

- Nyquist and Bode plots for untreated TMZF samples showed a pseudocapacitive behavior due to their very protective passive layer.
- The continuous increase of the impedance modulus |Z| in the untreated samples suggests that the corrosion resistance enhances with the immersion time.

- Bode representation corrected for ohmic resistance as a primary approach, and followed by the graphical representation of α_{eff} were successfully employed to determine the more accurate EEC.
- The EEC for the untreated sample was composed of a bi-layered microstructure, an outer porous oxide layer, and an inner barrier layer.
- The inner barrier layer grew through the immersion periods, indicating that the corrosion protection increase was mainly due to the effect of this barrier.
- Through the Nyquist and Bode plots, the CST samples showed a more reactive behavior compared with the untreated samples, independently of the immersion time in SBF.
- The impedance results for the CST samples after 14 days of immersion, corroborated the presence of the apatite layer over the surface.
- Alpha effective plots for CST samples indicated an extra relaxation process at low frequency, associated with diffusion phenomena occurring through the outer porous layers.
- TMZF samples after CST showed a thinner passive layer compare with untreated samples. It was associated with the dissolution of the oxide layer during the HCl attack.
- Impedance measurements of anodized samples in SBF showed a peculiar behavior that could not be modeled by the traditional equivalent circuits. It resembled the behavior of a porous electrode. Thus, it was proposed a two-channel transmission line model for analyzing the impedance results.
- Nyquist diagrams for nanotubes and nanopores samples reveal a capacitive or at least pseudocapacitive behavior. This means that the electrochemical reactions on the surface were very limited.
- Bode representations for the anodized samples independent of the soaking time showed a characteristic response of capacitive surface films.
- The impedance ζ, between the solution and the porous walls was purely pseudo-capacitive. This interface is almost not reactive, and the CPE behavior results from surface heterogeneities.
- During the immersion time in SBF, the resistance R_A gradually increased and the capacitance Q_B decreased. It could be associated with the initial steps to the apatite formation on the outer and inner parts of the anodized layers.
- The described models led to the successful fitting of EIS data measurements of the four different surface morphologies on TMZF samples, with meaningful fitting parameter values and low error between the experimental points and the simulation.

A final observation concerns the fact that these results illustrate the difficulty of extracting reliable parameters from the fitting of EIS through traditional EEC and TL models. This is a widely used procedure that must be carried out very carefully.

4.3 Fatigue behavior of the different surface treatments

Surface topography in titanium alloys applied in orthopedic and dental implants is essential because it will determine the level of cell adhesion and growth on them. Thus, those processes as anodizing and chemical surface treatments with HCl and NaOH that modify surfaces for better osseointegration may also cause changes in fatigue life behavior.

The fatigue performance analysis of metallic materials is mainly based on two phenomena, the first is the crack nucleation process, and the second is the process of propagation of these cracks, both due to cyclic solicitations.

Surface alteration processes, such as those used in this project, could lead to the formation of notches of considerable sizes, becoming cracks nucleation sites and therefore reducing the fatigue resistance of the material.

Additionally, during some stages of these modification processes, hydrogen gas is produced, and due to the affinity of the titanium β phase for the hydrogen, it could be absorbed in sufficient quantity causing embrittlement problems of the material, which could directly affect the propagation process of fatigue cracks.

In this way, the fatigue response of untreated samples (polished surface), treated with HCl and NaOH (CST) and anodized samples (nanopores) was evaluated. The fatigue resistance was determined through the staircase tests, and then the fracture surfaces were analyzed to assess the evidence of embrittlement mechanisms.

4.3.1 Fatigue resistance of TMZF samples untreated and treated with CST, and nanopores

Microstructure, chemical composition and tensile mechanical properties of the employed material followed the requirements of ASTM F1813-13. Table 4. shows the mechanical properties of the TMZF alloy used in this work compared to the standard minimal requirements.

Table 4.6 Mechanical properties of the TMZF titanium alloy used in this study.

Material	Yield strength 0.2% (MPa)	Tensile strength (MPa)	Elongation (%)
TMZF used	1060 ±19	1071±14	17±2
ASTM F1813-13	931	897	12

Orthopedic implants are subjected to cyclical loads due to the mechanical demands of the human body, submitting these components to high cycle fatigue conditions (HCF). High cycle fatigue tests ($N = 5 \times 10^6$ cycles) were performed using the staircase method to evaluate the fatigue performance of the different surfaces studied in this work.

As it was mentioned in section 2.2.1, untreated samples were grinded and polished, aiming to minimize the influence of surface defects induced by machining on the fatigue properties. Figure 4.38 displays the results of the staircase method for untreated samples. A maximum stress of 750 MPa was selected as the initial value based on the tensile test results (~70% of the yield strength) shown in Table 4.6

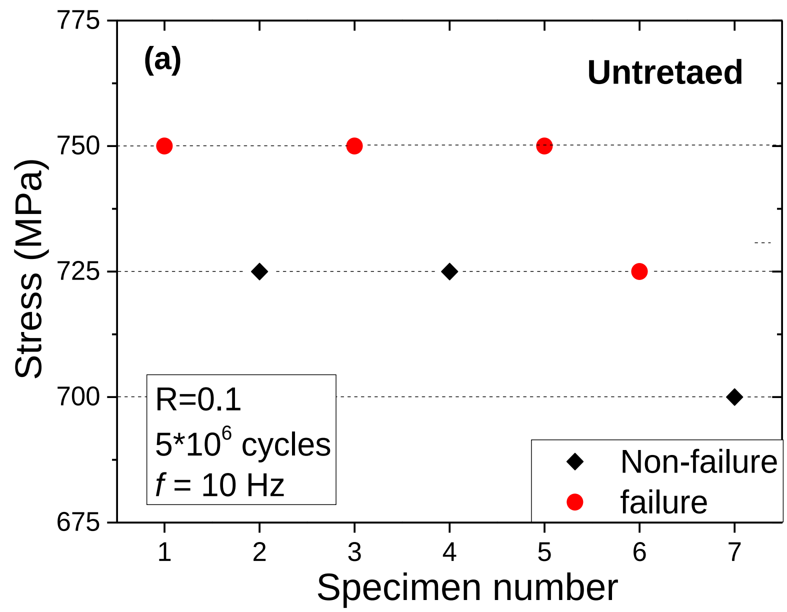

Figure 4.38 Staircase fatigue diagram for untreated samples. "●" Means failure and "♦" means survival to the run-out.

The data plotted in Figure 4.38 was rearranged and put in Table 4.7 to count the frequencies of failures and non-failures of the specimens tested at different stress levels. This procedure serves as a guide for the statistical calculation using the method of Dixon and Mood [4]. This statistical analysis has to be used for the events with the least number of observations between "failure" and "non-failure."

Table 4.7 Analysis of staircase method data for untreated TMZF alloy.

Non-failure				
Stress (MPa)	**Level** i	$\boldsymbol{n_i}$	$\boldsymbol{i * n_i}$	$\boldsymbol{i^2 * n_i}$
750	2	0	0	0
725	1	2	2	4
700	0	1	0	0
Sum	-	3	1	1
		N	**A**	**B**

The following expressions allow the calculation of the fatigue strength (σ_F):

$$\sigma_F = \sigma_0 + d \,. \left(\frac{A}{N} \pm 0{,}5\right) \tag{4.18}$$

Were $N = \sum n_i$

$A = \sum(i \,. n_i)$

$B = \sum(i^2 \,. n_i)$

$i =$ is the number of stress levels used ($i = 0,1,2,3, \ldots i_{máx}$)
$n_i =$ Number of occurrences of the selected event (failure, non-failure) at the level i

$\sigma_0 =$ Minimum tension reached in the test, where no specimen broke.

The sign (+) is used when the selected event is, non-failure and (-) when the event is, failure.

The standard deviation assessment is given as follows:

$$\mu = 1.62 \,. d \,. \left(\frac{N \,. B - A^2}{N^2} + 0.029\right) \tag{4.19}$$

When the ratio is:

$$\left(\frac{N \,. B - A^2}{N^2}\right) \geq 0.3 \tag{4.20}$$

Or equal to:

$$\mu = 0.53 \,. d \tag{4.21}$$

When the ratio is:

$$\left(\frac{N.B- A^2}{N^2}\right) < 0.3 \tag{4.22}$$

The fatigue limit in terms of maximum stress and the standard deviation calculated with the Dixon-Mood statistical approach are respectively 730 and 13 MPa.

Figure 4.39. shows the fracture surface of the untreated specimens to examine and determine the fracture characteristic after the fatigue tests. Crack nucleation on the surface (region 1) has been the leading initiation site for untreated samples. The zone of stable crack propagation or region 2 occupies around 50% of the entire surface and is characterized by well-defined fatigue striations and river patterns. The remaining area comprises a transition zone of unstable crack propagation.

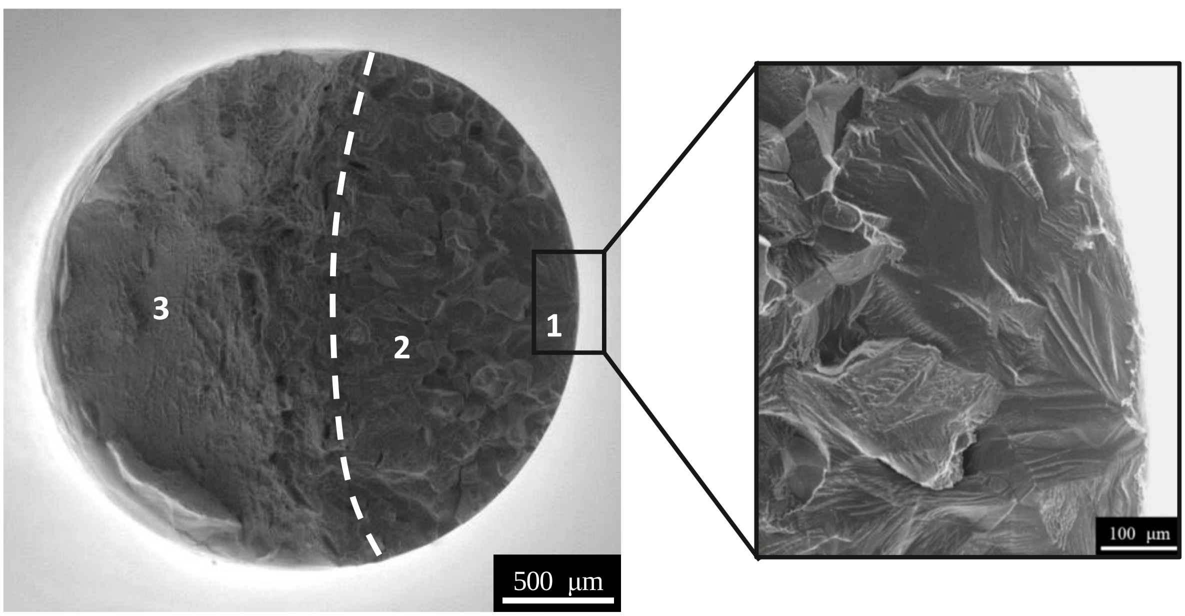

Figure 4.39 Fractography of untreated sample, the dash line designates the approximate transition between the stable and unstable crack propagation regions and the square indicates the magnified region on the right side, pointing out the crack initiation site.

With the aid of a laser scanning confocal microscope, topographic characteristics were obtained, such as roughness and morphology of the different treatments studied.

Table 4.8 reports the average roughness values (R_a) and peak-to-valley roughness (R_z) with the standard deviation values for each of the treatments. Untreated samples were polished to obtain a homogeneous and smooth surface, as it can be seen in Figure 4.40(a). The polishing process eliminates the risks arising from the machining process, which is corroborated by the low values of R_a and R_z roughness. This flat surface prevents or delays the nucleation of superficial fatigue cracks and is used as a suitable surface condition to determine the fatigue strength of a metallic material, in an attempt to minimize the effect of previous machining and heat treatment upon fatigue behavior variability [127].

Table 4.8 Topography measurements of R_a and R_z roughness of the untreated, CST and nanopores samples.

	R_a (µm)	**R_z (µm)**
Untreated	<0.100	<0.100
CST	0.443 ± 0.082	3.390 ± 0.841
Nanopores	<0.100	0.313 ± 0.044

Figure 4.40 (b) shows the topography of a representative sample treated with HCl and NaOH. This combined attack produces a surface with formation of generalized micro-pits in an approximate size of 3.40 µm. Higher than the value observed in the polished samples (<0.100 µm).

As it was indicated in section 1.5, roughness scattering (i.e., notches) can lead to considerable differences in the fatigue response of the component. For instance, grooves of approximately 3.50 µm on the Ti-6Al-4V alloy could reduce the fatigue resistance by around 12% [70].

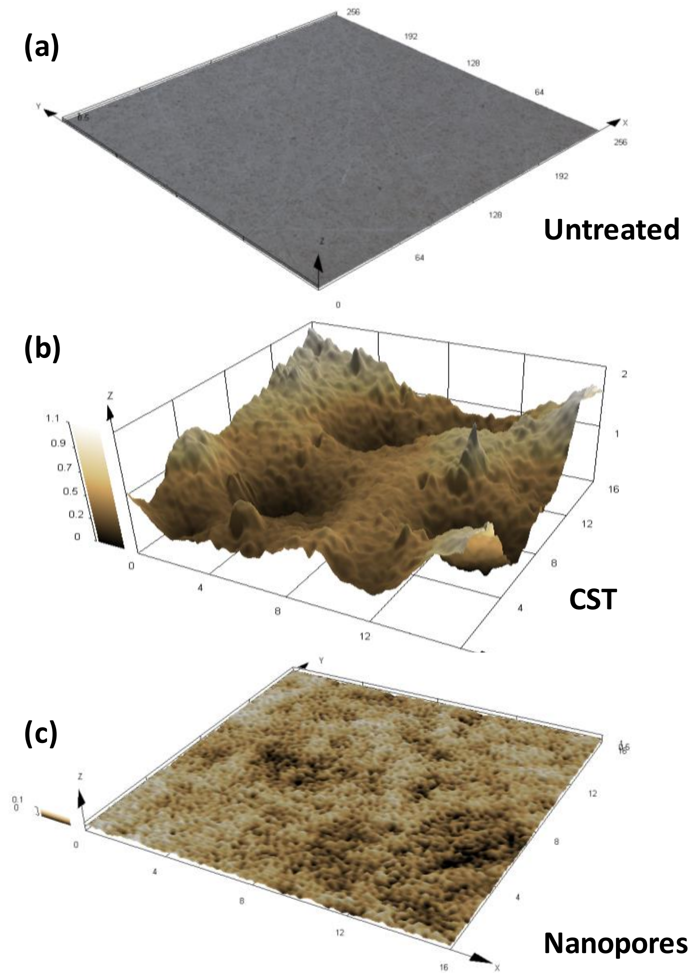

Figure 4.40 Representative 3D-images determined by confocal laser scanning microscopy of: a) untreated, b) CST and c) nanopores samples.

Preliminary fatigue results of CST samples showed a drastic decrease of the fatigue resistance to a value lower than 370 MPa (maximum principal tensile stress for a hip stem geometry [128]). This high reduction of the fatigue strength (~ 50% compared with the untreated samples) indicates the existence of an additional phenomenon to the notch sensitivity that is affecting the fatigue response of the material.

Previous studies employing HCl etching and NaOH treatment over an α+β titanium alloy showed a significant increase in the hydrogen content [129]. Even a slight increase in hydrogen content could cause embrittlement in titanium alloys, producing a reduction in fracture toughness and fatigue resistance [130, 131].

In this way, it was calculated the hydrogen content of the different surface conditions (Table 4.9), showing an increase after the surface treatments compared with the untreated samples. CST samples show the highest values, close to 310 ppm. This high hydrogen content could explain the drastic decrease in fatigue resistance of the CST specimens.

Table 4.9 Hydrogen content results for: Untreated, CST, CST-polished and nanopores.

	H (ppm)
Untreated	99 ± 22
CST not -polished	310 ± 23
CST-polished	261 ± 4
Nanopores	127 ± 23

To determine if there is an alteration of the fatigue performance by the hydrogen absorbed after the chemical treatment, TMZF specimens treated chemically were grinded and polished (using the same protocol employed in untreated samples) to eliminate the micro-pits formed, and thus avoid the notch effect. Then, the specimens were tested through the staircase fatigue method.

Figure 4.41 shows the results of the staircase method for CST-polished samples. Using the previous information of untreated conditions, the stress value of 725 MPa was selected as the initial one. This stress level was very high, and the initial specimens failed prematurely (empty rhombus in Figure 4.41); thus, they were not considered in the analysis of the fatigue resistance. On the other hand, the first specimen employed for the determination of the fatigue resistance failed at 550 MPa.

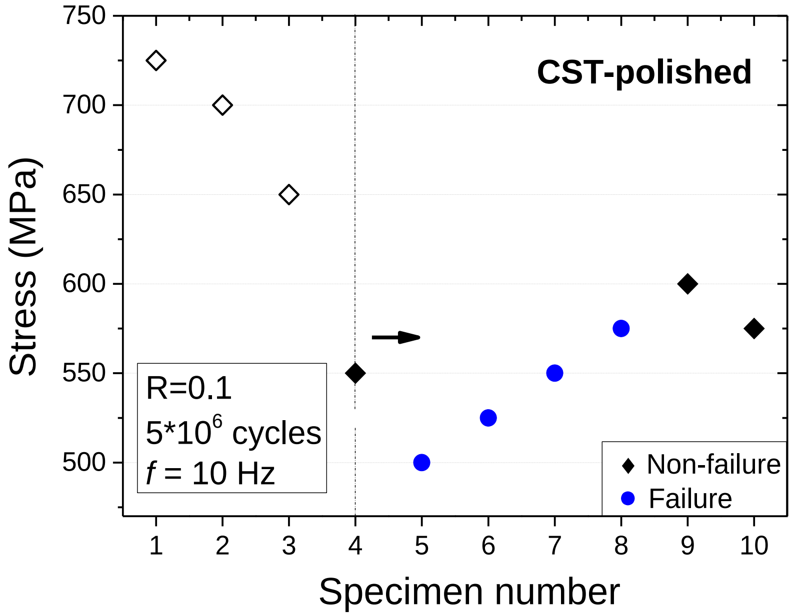

Figure 4.41 Staircase fatigue diagram for CST-polished samples. "●" Means failure, "♦" means survival to the run-out and "◊" specimens not considered in the analysis.

The data obtained from Figure 4.41 was organized and placed in Table 4.10. This information was employed in the Dixon and Mood statistical approach to determine the fatigue strength of the CST-polished samples. Here, the event with the least number of observations was "failure."

Table 4.10 Analysis of staircase method data for CST-polished samples.

Failure				
Stress (MPa)	**Level** i	n_i	$i * n_i$	$i^2 * n_i$
600	2	1	2	4
575	1	1	1	1
550	0	1	0	0
Sum	-	3	3	5
		N	**A**	**B**

The fatigue limit in terms of maximum stress and the standard deviation calculated are respectively 563 and 28 MPa for the samples chemically treated and polished. The reduction of 25% of the fatigue resistance compared with the untreated samples could be associated with the significant increase in the hydrogen content detected in the material even after grinding and polishing the surface of the specimens (Table 4.9).

Figure 4.42 shows the fracture surface of the CST-polished specimens. Here the propagation region is characterized by cleavage steps or river patterns. The branches of these river patterns join in the direction of crack propagation and can be used to establish the local fracture direction and the crack nucleation point, indicated by the black square.

The magnified region in Figure 4.42 shows evidence of secondary cracks formed through the grain boundaries. Generally, this fracture type is associated with hydrogen embrittlement phenomena, such as grain boundary embrittlement or even the repeated formation and rupture of brittle hydride phases close to the grain boundary [63, 132].

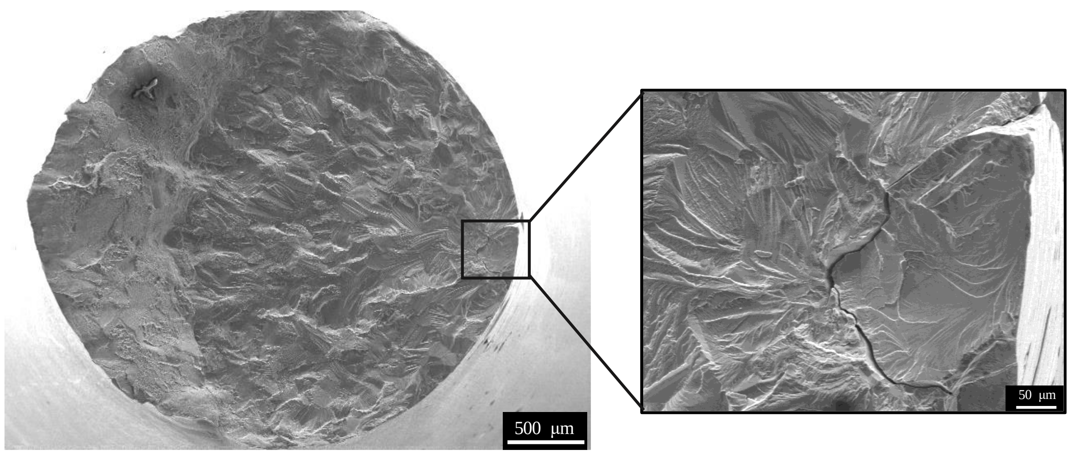

Figure 4.42 Fractography of CST-polished sample, the square indicates the magnified region on the right side, pointing out the crack initiation site.

As observed in Table 4.9, the samples anodized with nanopores presented a slight increase in the hydrogen content, close to 130 ppm. This value is lower than the observed in samples treated with CST. Moreover, from confocal measurements (Table 4.8), nanopores samples displayed a refined surface with low roughness values (R_z = 0.3 μm), avoiding a possible notch effect. These two conditions could indicate better fatigue behavior than the CST specimens.

In this way, fatigue specimens anodized with nanopores were tested. Initially, the maximum axial stress was 725 MPa, similar to the protocol established for CST samples. Contrary to the expected behavior, the specimen failed after few cycles (3258 cycles). Subsequently, new specimens tested at lower stress levels showed a similar behavior, as indicated in Figure 4.43. All of them failed, even the specimen tested at 300 MPa, at stress values lower than the maximum principal tensile stress for a hip stem geometry (370 MPa) [128]. Only the specimen tested at 200 MPa survived to the run-out. Indicating that even avoiding the possibility of notch effect, the anodization process reduced the fatigue resistance, and it could be associated with the hydrogen content in the samples.

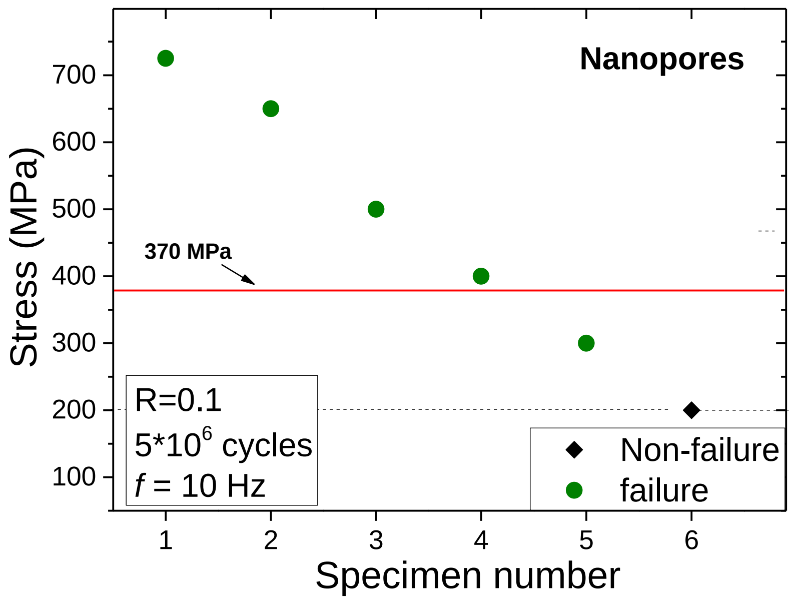

Figure 4.43 Staircase fatigue diagram for nanopores samples. "●" Means failure, "♦" means survival to the run-out and.

The fatigue fracture surface corresponding to the nanopores sample tested at 500 MPa is illustrated in Figure 4.44(a). As it is observed in the region (b), typical features of cyclic fatigue crack growth such as river patterns and cleavage steps appear and become the primary propagation mechanism in this region. This stable propagation zone of the fatigue crack is restricted to a small elliptical region.

The fractographies in Figure 4.44 (c-d) of the samples treated with nanopores and CST show more evidence of brittle fracture. Here an interesting and distinct cleavage pattern called Wallner lines is observed (indicated by black arrows). This arrangement is observed in fracture surfaces of brittle materials, brittle inclusions, or intermetallic compounds. It consists of two sets of parallel cleavage steps that often intersect to produce a crisscross pattern. Wallner lines result from the simultaneous propagation of a crack front and an elastic shock wave in the material [133].

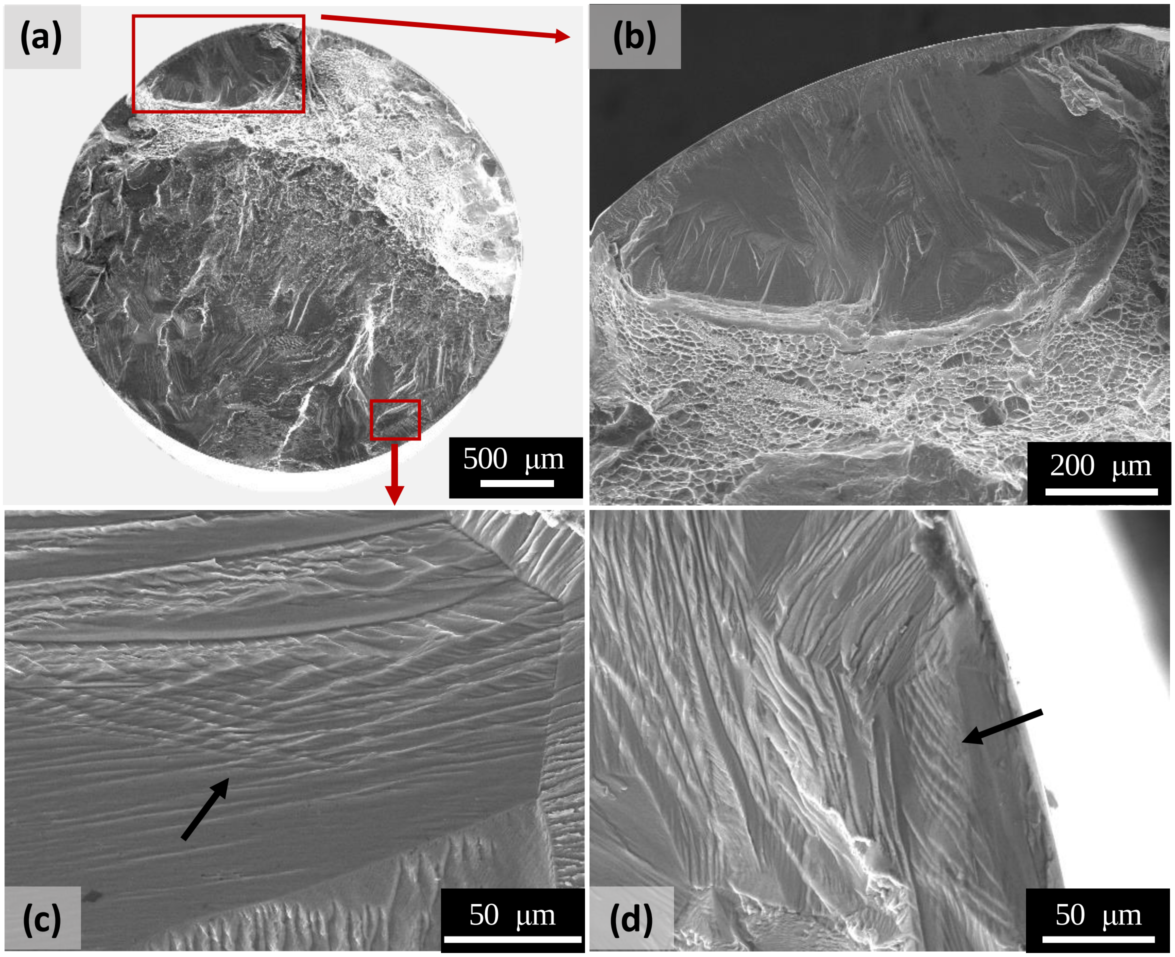

Figure 4.44 a) Fractography of nanopores sample, which was tested at 500 MPa, b) magnified zone indicating a stable crack propagation region, c) magnified region of the nanopores sample indicating Wallner lines and d) magnified region of the CST-polished sample which was fatigue tested at 550 MPa indicating the Wallner lines pattern.

4.3.2 Hydrogen embrittlement

Hydrogen embrittlement (HE) is an interesting but harmful phenomenon, and it could be presented in a wide variety of metals and alloys. HE involves a group of mechanisms associated with reducing the mechanical properties attributed to the hydrogen as the principal actor [63].

It is usually challenging to determine directly how hydrogen influences the behavior of metallic materials due to the difficulty in measuring and observing this element accurately. Therefore, its effects are indirectly deduced from variations in mechanical properties. Moreover, its effect depends on the way it is in the material, either trapped at crystal defects, in solution, or forming hydrides [134, 135].

Atomic hydrogen can be transported easily in titanium alloys by a combination of interstitial and intergranular diffusion, which in turn reduces the ductility and strength of the metal [63, 131, 132]. Different theories have been studied to explain how hydrogen causes embrittlement. However, the fracture mechanism behind this embrittlement in the titanium alloys is not fully understood.

This difficulty is especially true for metastable β titanium alloys where the effect of hydrogen on the mechanical behavior has been explained in terms of: (i) failure due to stress-induced hydride formation [130, 136], (ii) hydrogen-induced decohesion [63, 137, 138] and (iii) hydrogen-enhanced localized plasticity (HELP) [139, 140]. Even in single phase systems, as is the case of the TMZF alloy, the identification of the embrittlement mechanism is complex, and multiple hydrogen-related fracture mechanisms can operate simultaneously [137, 138, 140]. While a number of mechanisms have been proposed to explain hydrogen embrittlement, the aforementioned are considered to be the most applicable to this study.

Embrittlement attributed to hydride-forming is normally associated to the brittle characteristic of the hydride phase and the failure along the fragile hydride/metal interface. The degree of embrittlement should exhibit an inverse strain rate dependence, since hydride formation kinetics is diffusion-controlled, and low strain rates provide more time for the hydrides to form. Moreover, the hydrogen concentration at which this mechanism causes fracture depends on thermodynamic factors, as the local stress intensity, the volume change associated with hydride formation from solid solution, and the attractive H-H interaction [130, 136].

Since β titanium alloys exhibit very high hydrogen solubility, they do not readily form hydrides [141]. However, J. Von Pezold et al. [142]. employed simulations combining density functional theory (DFT) and the semi-empirical embedded atom method (EAM), and showed that it is possible to obtain stress-induced hydride seeds even in samples with hydrogen content lower than 160 ppm, due to an increase in the hydrogen local concentration in the tensile strain field of crystallographic defects [142].

Figure 4.45 shows the analysis by the automated crystal orientation mapping (ACOM-TEM) of the samples treated with CST and then fatigue tested. In addition to the β phase of the matrix, it is observed on the phase map the presence of very fine TiH_2 particles or seeds with a tetragonal lattice. The presence of those brittle hydrides is strong evidence of the effect of hydrogen in reducing the fatigue strength of the material.

These hydrides may result from the increase of the local hydrogen concentration in the tensile strain field of extended lattice defects, such as dislocations. Therefore, it is suggested that, as hydrogen exhibits a considerable solubility in the β phase, and according to the phenomenon known as stress-induced hydride, the localized deformation during the fatigue test induced the segregation of hydrogen [142, 143]. Consequently, TiH_2 precipitation occurred at high-energy grain boundaries, as observed in Figure 4.45b and 4.45c.

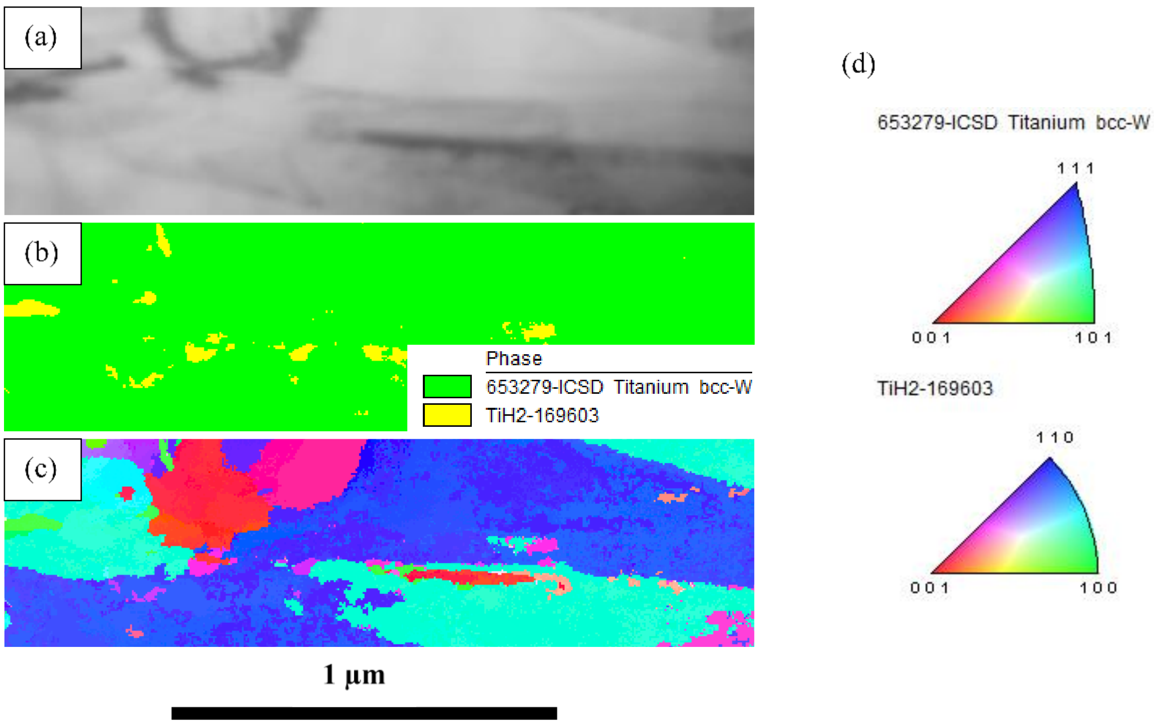

Figure 4.45 Images of the CST-polished sample and fatigue tested generated using the ASTAR system coupled to TEM: (a) virtual bright-field (VBF) image, (b) phase mapping (PM), (c) orientation image mapping (OIM) and (d) inverse pole figure (IPF) from where the colors were used to index orientations in the OIM.

The second HE mechanism inferred from the TMZF specimens studied in this work is the hydrogen-induced decohesion, which associates the fracture stress reduction of the lattice with the decrease of its cohesive energy by the presence of the solute hydrogen into the matrix [137, 139]. Usually, in alloys with low hydrogen content, the supporting evidence is the fracture surface characteristics, define by intergranular failures by decohesion of the grain boundaries [137, 138].

During the crack propagation, the work required to separate the grain boundary into two free surfaces decreases with increasing the hydrogen content [139]. Figure *4.*46 shows evidence of this phenomenon on nanopores samples fractured after fatigue tests at 650 MPa. Here, the hydrogen weakens the bonding to allow the decohesion mechanism with little plasticity. Thus, the high stress intensity (high crack velocities) causes failure of the grain boundaries by intergranular decohesion.

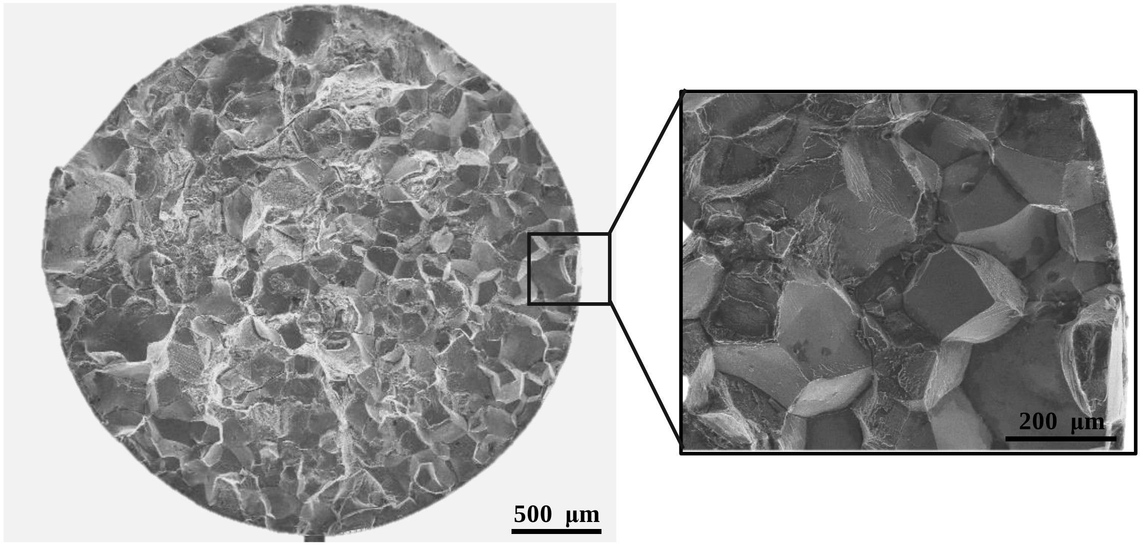

Figure 4.46 Fractography of nanopores sample, which was fatigue tested at 650 MPa, the square indicates the magnified region on the right side.

The third HE mechanism studied in this work is the hydrogen-enhanced localized plasticity (HELP). In this theory, the nucleation and motion of dislocations are favored by the hydrogen content [137, 144]. In this sense, it is expected an increase of deformation and plasticity at the zone with high hydrogen concentration. Thus, evidence justifying the HELP mechanism is observed in fractography with localized ductile crack propagation, contrary to a brittle characteristic ahead of the crack tip [139, 140].

Traditionally, the fatigue crack growth mechanism in metals depend on striations formed by slip at a crack tip [133]. During the crack growth, the crack tip blunt until the saturation level, at the maximum load (Figure 4.47 a). Nevertheless, when the hydrogen is present, it diffuses toward crack tips and concentrates in this zone (Figure 4.47 b-2). Thus, the hydrogenated crack continues growing even after the maximum load. Thereby, the fatigue crack growth rates of hydrogen-charged zones are more favorable than those of non-charged [140].

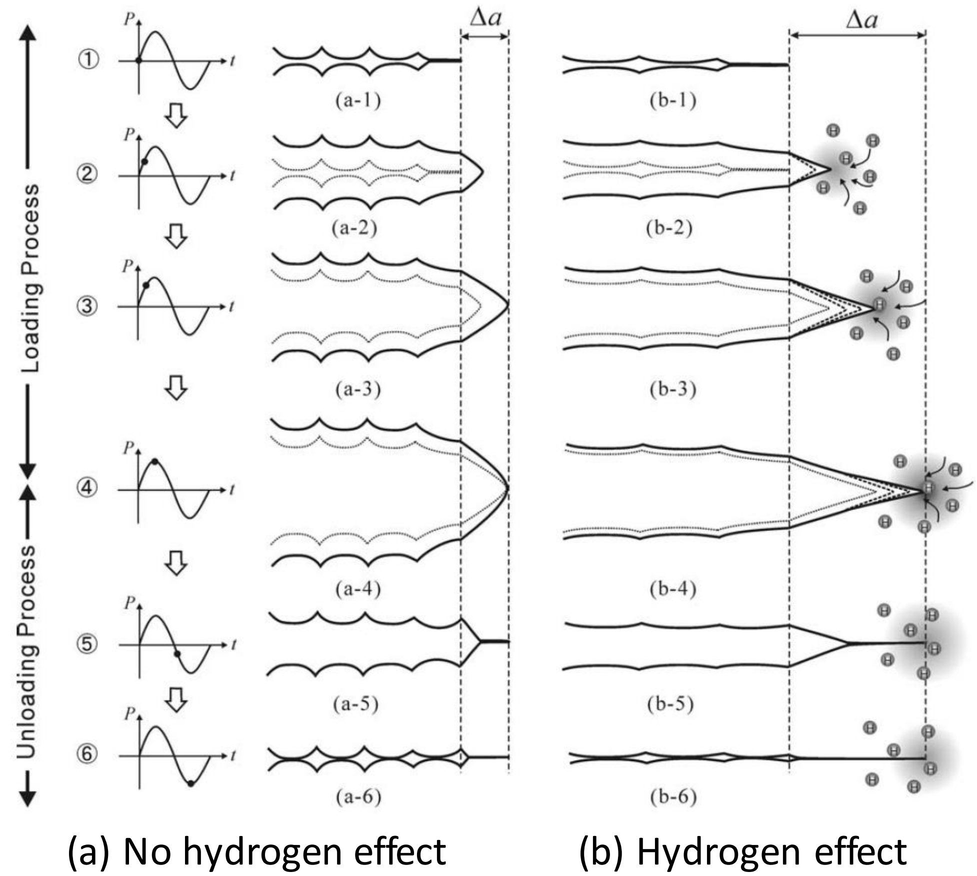

Figure 4.47 Crack tip opening and striation formation mechanism in fatigue: (a) no hydrogen effect, (b) hydrogen effect. Extracted from [144].

As mentioned in Chapter 1, hydrogen is produced during these two treatments (CST and anodized) at the metal/electrolyte interface. Simultaneously, a quantity of this element is absorbed and diffused into the titanium alloy; however, a high quantity is accumulated adjacent to the specimen surface. This condition facilitated the observation of the HELP mechanism acting on the nanopores and CST not-polished samples during the fatigue tests.

Figure 4.48 shows evidence of the HELP mechanism acting on the CST not-polished samples during the fatigue test at 300 MPa. Through the magnified images it is possible to observe a circumferential crack propagating in the round specimen. The propagation of this localized ductile crack is confined within a region of approximately 26 ± 5 μm from the sample surface (Figure 4.48 b-d), favored by an increase in dislocation nucleation and mobility, due to the higher concentration of hydrogen in this subsurface region.

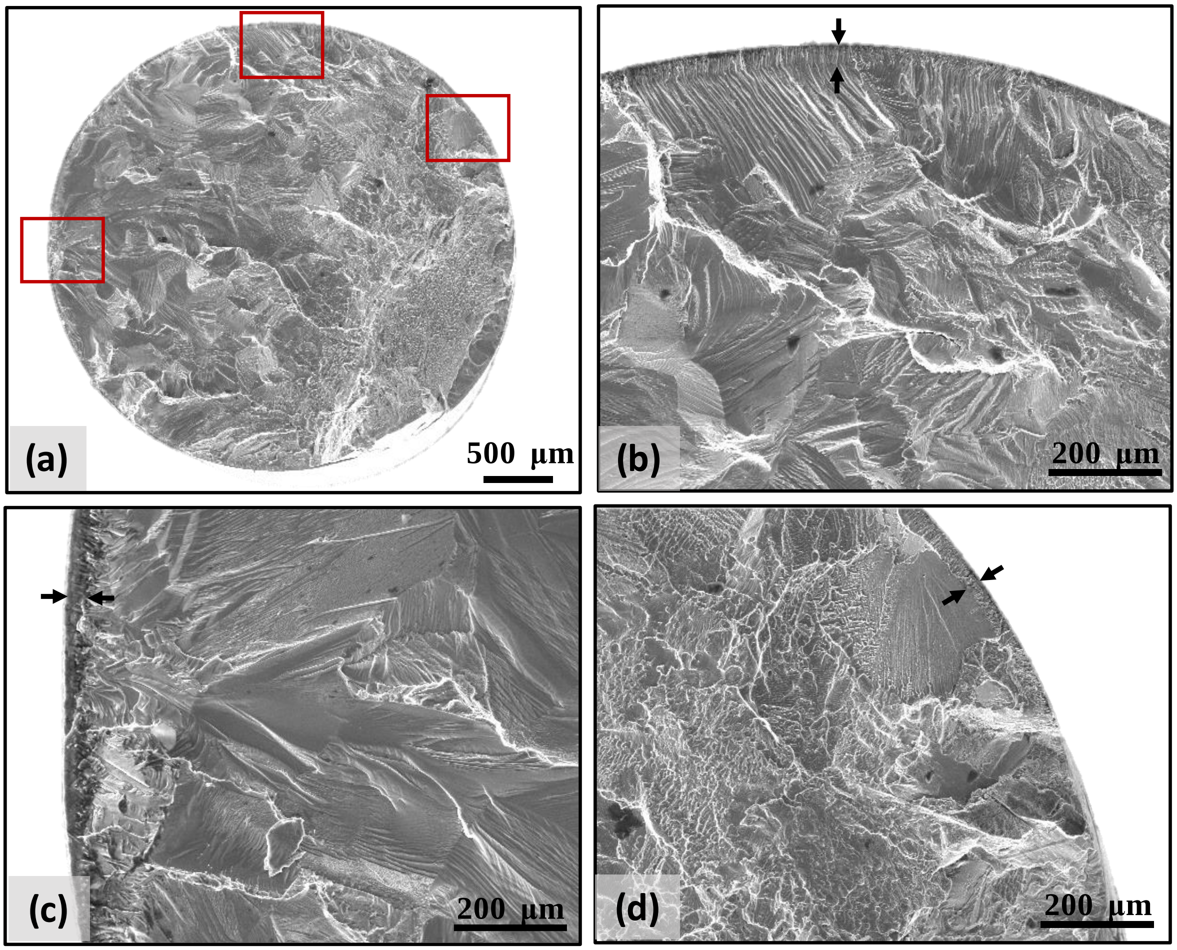

Figure 4.48 a) Fractography of CST not-polished sample, which was fatigue tested at 300 MPa, b), c) and d) magnified zone indicating a stable crack propagation region at the hydrogenated zone indicated by black arrows.

Similar behavior was observed in the nanopores samples fractured after the fatigue tests. Figure 4.49 shows the evidence of a circumferential crack propagating around the specimen. These observations suggest that the values displayed in Table *4.*9, for the samples with nanopores and CST could be higher than indicated, due to the high hydrogen concentration at the sample surface and the experimental difficulties to obtain the accurate concentration in this region.

Here, the confined region of the circunferential crack is a little bit more diffuse due to a lower quantity of hydrogen absorved during the anodizing treatment compared with the quantity absorved by the samples during the CST as it was indicated in Table 4.9.

Figure 4.49 shows that the circumferential surface crack is generated and propagated during the initial cycles. From this, new crack nucleates and then spread radially into the sample on a plane normal to the external load (Figure 4.49 c). Finally, failure happens under overload displaying shallow dimples. As observed in Figure *4.*49, this final failure connects directly with the pre-existence circumferential crack, which corroborates the fracture sequence mentioned.

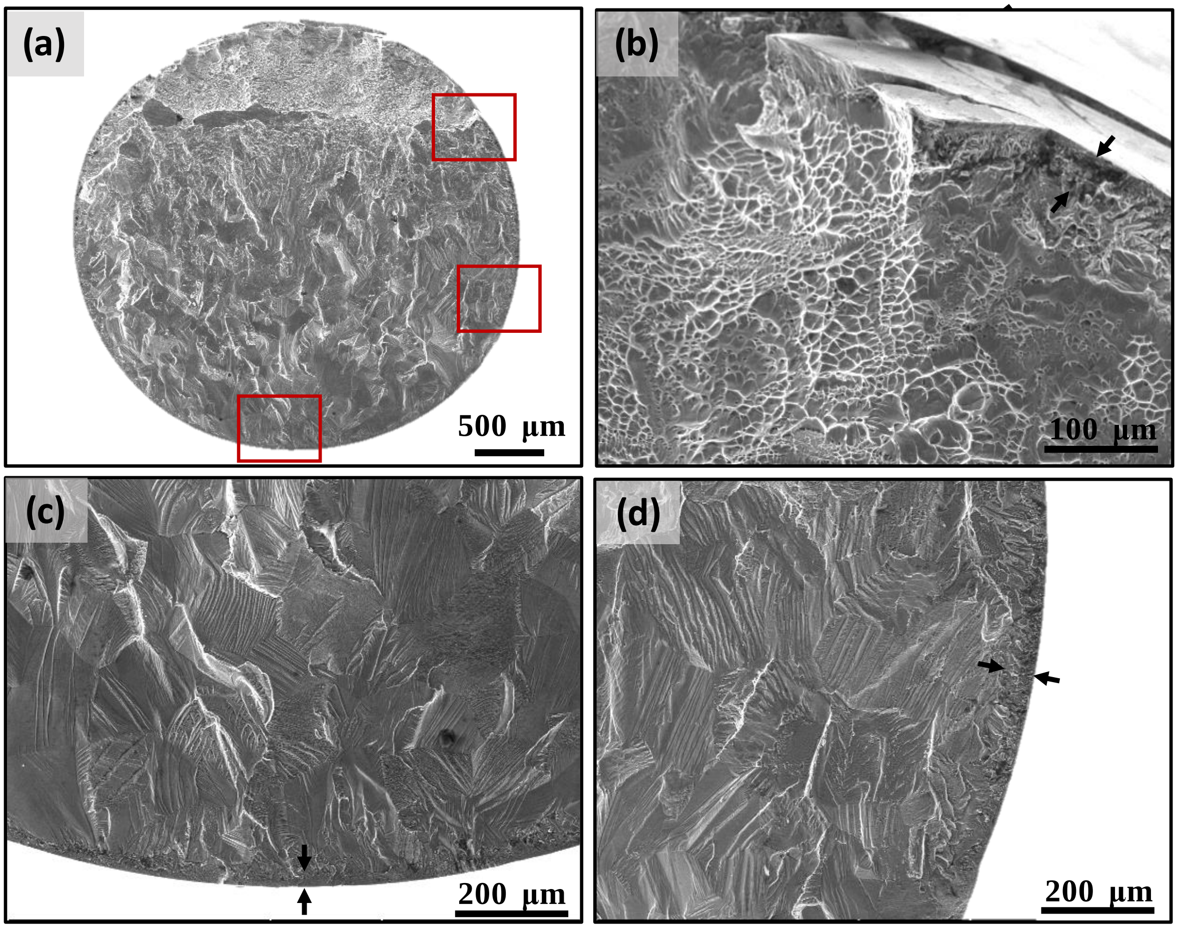

Figure 4.49 a) Fractography of nanopores sample, which was fatigue tested at 300 MPa, b) magnified zone of the final failure, c) and d) zone indicating a stable crack propagation region at the hydrogenated area, indicated by black arrows.

Table 4.11 shows the results of exploratory tensile testing of CST and nanopores specimens, together with the results of the untreated samples to determine if the hydrogen content produces significant changes in the tensile properties. A negligible difference in the yield strength and ultimate tensile strength was observed for the different treatments. Nevertheless, the elongation decreased in both treatments, but it was more evident in the nanopores samples.

Table 4.11 Tensile testing results of untreated, CST and nanopores samples.

	Yield strength 0.2% (MPa)	**Tensile strength (MPa)**	**Elongation (%)**
Untreated	1060 ±19	1071±14	17±2
CST	1059±18	1077±8	14±2
Nanopores	1020±20	1030±10	5±2

Additional to the elongation reduction, the untreated and treated samples showed different fracture characteristics, as observed in Figure 4.50. Untreated samples show a ductile fracture with evidence of plastic deformation and formation of a necking region. The magnified zone of the untreated sample in Figure 4.50 (a) displays deep dimples with conical shape. Unlike the CST and nanopores samples, the dimples become shallower due to the mode of fracture changed to intergranular decohesion in these hydrogen-embrittled samples (Figure 4.50 b and c).

The lateral view of the fractured samples displays more evidence of the hydrogen embrittlement mechanism. In Figure 4.50 b and c it is observed the presence of multiple secondary cracks that propagated in a direction perpendicular to the tensile axis. This peculiar crack grow is favored by the HELP mechanism.

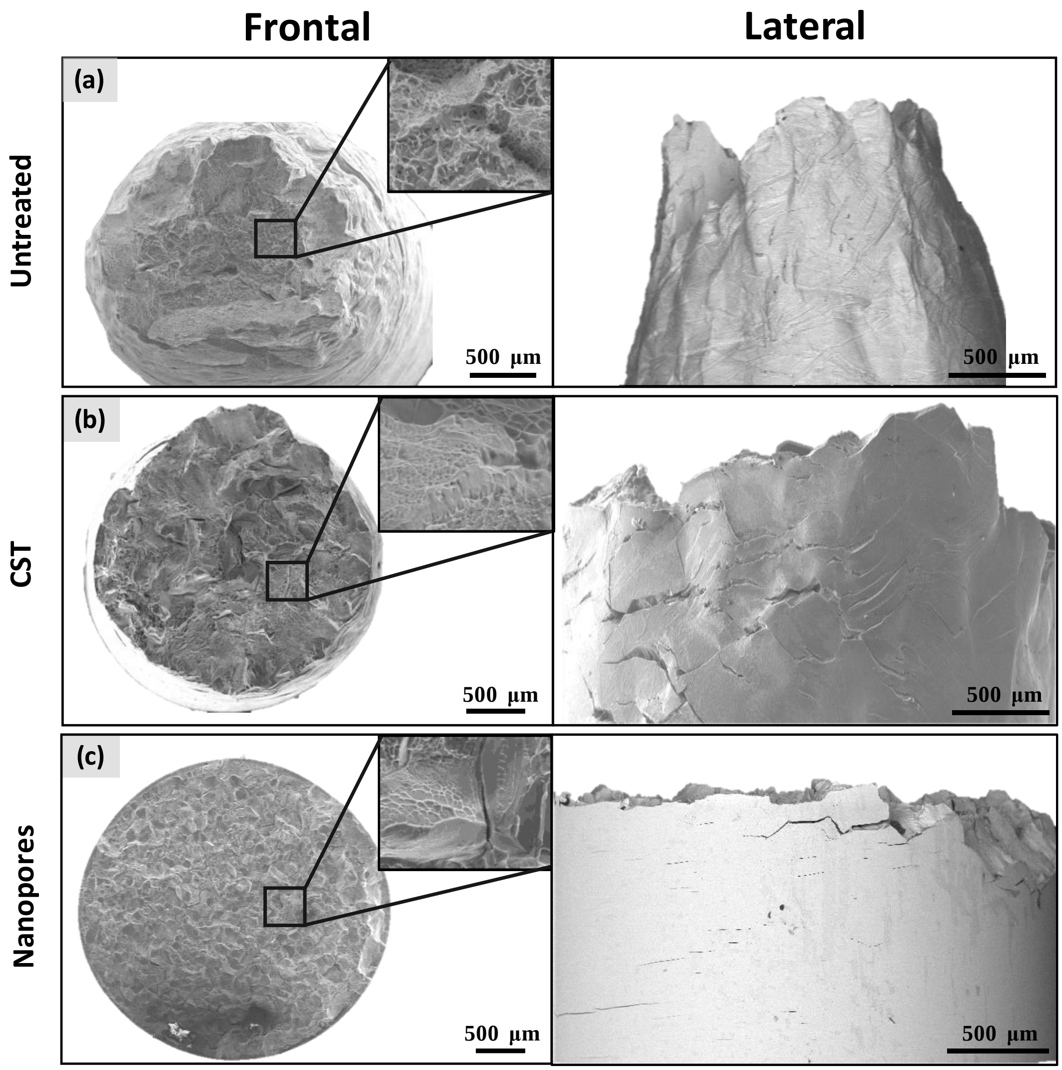

Figure 4.50 Frontal and lateral fractography of: a) untreated, b) CST and c) nanopores samples.

All of this fractographic information evidence the embrittlement processes produced by the hydrogen pick-up during the different surface treatments. Moreover, the drastic fatigue reduction observed in the NP specimens could indicate a higher hydrogen content that was not accurately detected during the measurement.

The explanation for these low hydrogens values is that we used anodized disc-shaped samples for the hydrogen measurements because they could be more easily cut into small pieces without inducing hydrogen desorption. However, in these samples, only one disc face was exposed to the anodization process and therefore to hydrogen diffusion, while the fatigue specimens were totally immersed in the solution during the anodization process, and a larger area was exposed to the hydrogen diffusion.

Table 4.12 summary of the fatigue response for the different surface conditions studied in this work.

	Roughness condition	**Fatigue stress (MPa)**	**Fractographic Observations**
Untreated	Polished surface	730	• Well define fatigue striation and river patterns.
CST not -polished	Roughness	< 300	• Circumferential crack propagation associated with HELP mechanism. • High roughness, possibility of notch effect.
CST-polished	Polished surface	563	• Secondary cracks at the grain boundaries. • Evidence of hydride formation.
Nanopores	Soft	< 300	• Intergranular fracture in samples tested at high stress level and correlated with the hydrogen-induced decohesion mechanism. • Circumferential crack propagation associated with HELP mechanism.

As it was demonstrated in this chapter, hydrogen levels of 150 to 350 ppm could drastically reduce the fatigue strength of the TMZF titanium alloy (Table 4.12). However, some studies as the one developed by Y. Murakami et al. [140, 144] indicate that it is possible to revert this phenomenon through a hydrogen desorption process. They employed a special heat treatment called non diffusible hydrogen desorption-heat treatment (NDH-HT), to remove the hydrogen trapped at the interstitial sites. This process decreases substantially the hydrogen content whereby reduce the fatigue crack growth (Figure 4.51).

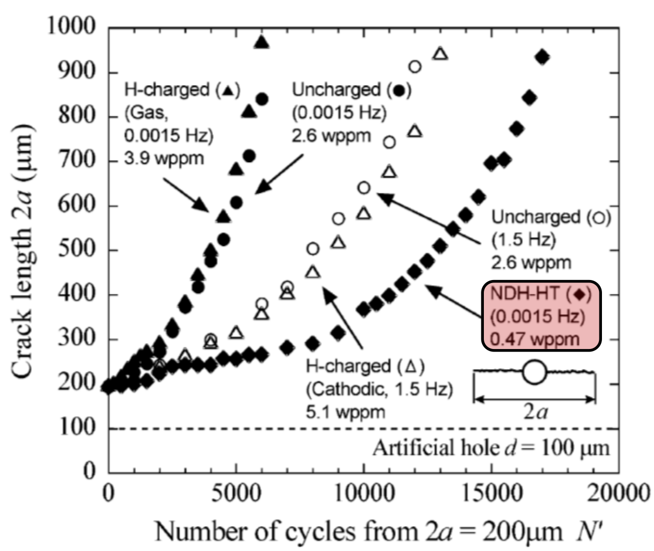

Figure 4.51 effect of the NDH-HT on crack growth rate of type 316L stainless steel (Extracted and edited from [144]).

In this chapter the fatigue response of untreated samples, treated with HCl and NaOH and nanopores samples was studied, and the conclusions are summarized in the following paragraphs:

- Untreated TMZF samples showed a high fatigue limit in terms of maximum stress of 730 MPa.
- Fatigue results of CST samples without subsequent polishing showed a drastic decrease in the fatigue resistance, greater than 50%, compared with the fatigue resistance of the untreated samples.
- CST-polished samples showed better fatigue behavior than the CST not-polished. However, they showed a decrease of 25% of the fatigue resistance compared with the untreated samples.
- Elemental analyses showed a significant increase in the hydrogen content in the samples treated with CST even after grinding and polishing the surface.
- Even with a slight increase in the hydrogen content, nanopores samples showed a dramatic reduction of the fatigue resistance, similar to the fatigue resistance of the CST not-polished.
- Clear evidence of brittle fracture was observed in the fractographies of the CST and nanopores samples called Wallner lines; these patterns are observed on fracture surfaces of brittle materials.
- In this study three principal hydrogen embrittlement mechanisms possibly acted over the treated samples: stress-induced hydride formation, hydrogen-induced decohesion and hydrogen-enhanced localized plasticity.
- Analysis by the automated crystal orientation mapping showed the presence of small TiH2 particles or seeds. These hydrides increase the local dislocation density, favoring the micro-cracks nucleation.
- Evidence of the hydrogen-induced decohesion and HELP mechanisms were observed in the fractography of the nanopores and CST samples fatigue tested; however, more studies are necessary to certify these mechanisms.
- Equally, it was found evidence of the hydrogen embrittlement acting over the treated samples during the tensile testing, reducing the elongation and providing brittle fracture characteristics.
- The fatigue results and the hydrogen embrittlement mechanisms observed in this study point out the risk of well-known methods as cited in this chapter to design the titanium surface for osseointegration improvements.

5 GENERAL CONCLUSIONS

In this thesis it was studied the biocompatibility and corrosion performance of Ti-12Mo-6Zr-2Fe samples with nanotubes, nanopores and CST immersed during 0. 1. 7 and 14 days in SBF, as well as the fatigue resistance variation of untreated samples, treated with CST and nanopores. The conclusions from these analyses are summarized in the following paragraphs:

- Surface treatments as nanotubes, nanopores and CST on β-TMZF alloy were successfully obtained.
- After 14 days of immersion in SBF, nanotubes and nanopores samples showed a lower and moderate HAp formation (respectively). Meanwhile, the CST samples showed the best bioactivity behavior.
- Potentiodynamic polarization curves of nanotubes and nanopores surfaces revealed a more protective behavior against corrosion, placed them in the “Very stable” resistance class.
- Through the electrochemical tests, the CST samples showed a more reactive behavior independently of the immersion time in SBF.
- Impedance curves of the anodized samples revealed a pseudocapacitive behavior, corroborating the protective response of these surface conditions. Additionally, it was observed a particular behavior that could be modeled successfully by a transmission line model.
- Untreated TMZF samples showed a high fatigue limit in terms of maximum stress of 730 MPa.
- Fatigue results of CST samples showed a drastic decrease of the fatigue resistance around to 50% compared with the untreated samples, due to the notch effect and the additional high hydrogen content.
- In order to avoid the notch effect, new CST samples were polished and then fatigue tested. However, they showed a decrease of 25% of the fatigue resistance compared with the untreated samples, which was associated with the hydrogen absorbed during the CST.
- Even with a slight increase in the hydrogen measured, nanopore samples with low surface roughness showed a dramatic reduction in fatigue resistance, similar to the CST not-polished samples. This behavior was associated with the possibility of a high hydrogen concentration at the sample surface.
- In this study was observed evidence of three hydrogen embrittlement mechanisms possibly acting over the treated samples. However, more studies

are necessary to corroborate it.

- These results motivate us to conduct systematic evaluations of mechanical and electrochemical properties when metallic surfaces are modified to improve their osseointegration.

6 FURTHER RESEARCH

- Study alternative anodizing parameters and also complementary treatments above the two anodization processes to improve their HAp formation process.
- Study in more detail the hydrogen embrittlement mechanisms acting in the TMZF alloy.
- Investigate the hydrogen effect on another commercial β titanium alloys treated with CST, nanotubes, and nanopores.
- Investigate the possibility of reverting the hydrogen embrittlement phenomenon through hydrogen desorption processes.

7 REFERENCES

[1] S. Minagar, C. C. Berndt, J. Wang, E. Ivanova, and C. Wen, A review of the application of anodization for the fabrication of nanotubes on metal implant surfaces, Acta Biomater., vol. 8, no. 8, pp. 2875–2888, 2012.

[2] ASTM, F1813 Standard Specification for Wrought Titanium-12Molybdenum-6Zirconium-2Iron Alloy for Surgical Implant (UNS R58120), ASTM Int. Conshohocken, PA, www.astm.org, pp. 1–5, 2013.

[3] T. Kokubo and S. Yamaguchi, Bioactive Metals Prepared by Surface Modification: Preparation and Properties Tadashi, vol. 52. Springer New York, 2011.

[4] C. A. E. Claros and D. P. de Oliveira, Fatigue behavior of Ti–6Al–4V alloy in saline solution with the surface modified at a micro- and nanoscale by chemical treatment, Mater. Sci. Eng. C, vol. 67, pp. 425–432, 2016.

[5] F. Hilario, V. Roche, R. P. Nogueira, and A. M. J. Junior, Influence of morphology and crystalline structure of TiO_2 nanotubes on their electrochemical properties and apatite-forming ability, Electrochim. Acta, vol. 245, pp. 337–349, 2017.

[6] Technical Committee ISO/TC 150, International Standard ISO 23317 : Implants for surgery — In vitro evaluation for apatite-forming ability of implant materials, 2014.

[7] C. Leyens and M. Peters, Titanium and Titanium Alloys. 2003.

[8] Y. Zheng, Nucleation Mechanisms of Refined Alpha Microstructure in Beta Titanium Alloys, no. May 2013, p. 211, 2013.

[9] G. Lütjering and J. C.Williams, Titanium. Berlin, Heidelberg: Springer Berlin Heidelberg, 2007.

[10] C. Leyens and M. Peters, Edited by Handbook of Cellular Metals Phase Transformations in Materials. 2003.

[11] P. I. Branemark, U. Breine, B. Johansson, P. J. Roylance, H. Röckert, and J. M. Yoffey, REGENERATION OF BONE MARROW, Cells Tissues Organs, vol. 59. pp. 1–46, 1964.

[12] International Titanium Association, Titanium today, medical edition. 2017.

[13] R. Del Pozo, Jose, Patel, Infection Associated with Prosthetic Joints, N. Engl. J. Med., vol. 361, no. 8, pp. 787–794, 2009.

[14] Y. Li, C. Yang, H. Zhao, S. Qu, X. Li, and Y. Li, New Developments of Ti-Based

Alloys for Biomedical Applications, Materials (Basel)., vol. 7, no. 3, pp. 1709–1800, 2014.

[15] C. R. Schwartsmann, L. C. Boschin, R. Z. Gonçalves, A. K. Yépez, and L. De Freitas Spinelli, New bearing surfaces in total hip replacement, Rev. Bras. Ortop., vol. 47, no. 2, pp. 154–159, 2012.

[16] A. dos Santos, Comportamento mecânico da liga Ti-6Al-4V com superfície modificada por laser de femtosegundo para uso biomédico, Universidade Federal de São Carlos, 2012.

[17] T. Narushima, New-generation metallic biomaterials, in Metals for Biomedical Devices, Elsevier, 2010, pp. 355–378.

[18] M. Navarro, a Michiardi, O. Castaño, and J. a Planell, Biomaterials in orthopaedics., J. R. Soc. Interface, vol. 5, no. July, pp. 1137–1158, 2008.

[19] Lütjering G. and W. J. C., Titanium. 2007.

[20] Y. Oshida, Bioscience and Bioengineering of Titanium Materials, 1st ed. 2007.

[21] M. Niinomi, Fatigue characteristics of metallic biomaterials, Int. J. Fatigue, vol. 29, pp. 992–1000, 2007.

[22] D. Banerjee and J. C. Williams, Perspectives on titanium science and technology, Acta Mater., vol. 61, no. 3, pp. 844–879, 2013.

[23] L. D. Zardiackas, M. J. Kraay, and H. L. Freese, Titanium, Niobium, Zirconium, and Tantalum for Medical and Surgical. 2005.

[24] F. Technique, R. Metals, R. Metals, T. Alloys, A. Bar, and T. Alloys, Standard Specification for Wrought Titanium-12Molybdenum-6Zirconium-2Iron Alloy for Surgical Implant (UNS R58120) 1, pp. 1–5, 2017.

[25] K. K. Wang, Larry J Gustavson, and J. H. Dumbleton, Microstructure and properties of a new beta titanium alloy, TI-12Mo- 6Zr-2Fe, developed for surgical implants, pp. 76–87, 1996.

[26] X. Liu, P. K. Chu, and C. Ding, Surface modification of titanium, titanium alloys, and related materials for biomedical applications, Mater. Sci. Eng. R Reports, vol. 47, no. 2004, pp. 49–121, 2004.

[27] D. P. De Oliveira, Tratamentos de superfície em Ti-CP , Ti-6Al-4V e Ti-6Al-7Nb visando a osseointegração de implantes : propriedades das superfícies e respostas osteoblásticas Tratamentos de superfície em Ti-CP , Ti-6Al-4V e Ti-6Al-7Nb visando a osseointegração de implantes, Universidade Federal de Sao Carlos, 2013.

[28] R. Brånemark, P. I. Brånemark, B. Rydevik, and R. R. Myers, Osseointegration in skeletal reconstruction and rehabilitation: a review., J. Rehabil. Res. Dev., vol. 38, no. 2, pp. 175–181, 2001.

[29] L. Le Guéhennec, a. Soueidan, P. Layrolle, and Y. Amouriq, Surface treatments of titanium dental implants for rapid osseointegration, Dent. Mater., vol. 23, pp. 844–854, 2007.

[30] L. Jon, Biomimetic apatite formation on chemically treated titanium, vol. 25, pp. 1187–1194, 2004.

[31] L. Jonásová, F. a Müller, A. Helebrant, J. Strnad, and P. Greil, Hydroxyapatite formation on alkali-treated titanium with different content of Na+ in the surface layer., Biomaterials, vol. 23, no. 15, pp. 3095–101, 2002.

[32] H. Takadama, H. Kim, T. Kokubo, and T. Nakamura, An X-ray photoelectron spectroscopy study of the process of apatite formation on bioactive titanium metal, J Biomed Mater Res., vol. 55, pp. 185–193, 2001.

[33] M. Wei, H. M. Kim, T. Kokubo, and J. H. Evans, Optimising the bioactivity of alkaline-treated titanium alloy, Mater. Sci. Eng. C, vol. 20, no. 1–2, pp. 125–134, 2002.

[34] A. Nagaoka, K. Yokoyama, and J. Sakai, Evaluation of hydrogen absorption behaviour during acid etching for surface modification of commercial pure Ti, Ti-6Al-4V and Ni-Ti superelastic alloys, Corros. Sci., vol. 52, no. 4, pp. 1130–1138, 2010.

[35] K. Das, S. Bose, and A. Bandyopadhyay, TiO_2 nanotubes on Ti: Influence of nanoscale morphology on bone cell-materials interaction, J. Biomed. Mater. Res. - Part A, vol. 90, no. 1, pp. 225–237, 2009.

[36] F. Hilario, Synthèse et caractérisations de nanotubes de TiO_2 pour applications biomédicales : propriétés électrochimiques et bioactivité, Université Grenoble Alpes, 2018.

[37] M. Li, M. J. Mondrinos, X. Chen, M. R. Gandhi, F. K. Ko, and P. I. Lelkes, Elastin Blends for Tissue Engineering Scaffolds, J. Biomed. Mater. Res. Part A, vol. 79, no. 4, pp. 963–73, 2006.

[38] J. Park, S. Bauer, K. Von Der Mark, and P. Schmuki, Nanosize and vitality: TiO_2 nanotube diameter directs cell fate, Nano Lett., vol. 7, no. 6, pp. 1686–1691, 2007.

[39] J. Park, S. Bauer, K. A. Schlegel, F. W. Neukam, K. Der Von Mark, and P. Schmuki, TiO_2 nanotube surfaces: 15 nm - an optimal length scale of surface

topography for cell adhesion and differentiation, Small, vol. 5, no. 6, pp. 666–671, 2009.

[40] K. Von Der Mark, S. Bauer, J. Park, and P. Schmuki, Another look at "Stem cell fate dictated solely by altered nanotube dimension," Proc. Natl. Acad. Sci. U. S. A., vol. 106, no. 24, p. 2009, 2009.

[41] Y. Wang, C. Wen, P. Hodgson, and Y. Li, Biocompatibility of TiO_2 nanotubes with different topographies, J. Biomed. Mater. Res. - Part A, vol. 102, no. 3, pp. 743–751, 2014.

[42] A. Jaroenworaluck, D. Regonini, C. R. Bowen, R. Stevens, and D. Allsopp, Macro, micro and nanostructure of TiO_2 anodised films prepared in a fluorine-containing electrolyte, J. Mater. Sci., vol. 42, no. 16, pp. 6729–6734, 2007.

[43] K. Lee, A. Mazare, and P. Schmuki, One-Dimensional Titanium Dioxide Nanomaterials : Nanotubes, 2014.

[44] J. M. Macak, H. Tsuchiya, A. Ghicov, K. Yasuda, R. Hahn, S. Bauer, and P. Schmuki, TiO_2 nanotubes: Self-organized electrochemical formation, properties and applications, Curr. Opin. Solid State Mater. Sci., vol. 11, no. 1–2, pp. 3–18, 2007.

[45] A. Roguska, M. Pisarek, M. Andrzejczuk, M. Dolata, M. Lewandowska, and M. Janik-Czachor, Characterization of a calcium phosphate- TiO_2 nanotube composite layer for biomedical applications, Mater. Sci. Eng. C, vol. 31, no. 5, pp. 906–914, 2011.

[46] N. K. Awad, S. L. Edwards, and Y. S. Morsi, A review of TiO_2 NTs on Ti metal: Electrochemical synthesis, functionalization and potential use as bone implants, Mater. Sci. Eng. C, vol. 76, pp. 1401–1412, 2017.

[47] W. Q. Yu, Y. L. Zhang, X. Q. Jiang, and F. Q. Zhang, In vitro behavior of MC3T3-E1 preosteoblast with different annealing temperature titania nanotubes, Oral Dis., vol. 16, no. 7, pp. 624–630, 2010.

[48] J. Lario, M. Viera, Á. Vicente, A. Igual, and V. Amigó, Corrosion behaviour of Ti6Al4V ELI nanotubes for biomedical applications, J. Mater. Res. Technol., vol. 8, no. 6, pp. 5548–5556, 2019.

[49] M. Niinomi, Metals for biomedical devices. 2010.

[50] Nestor Perez, Electrochemistry and Corrosion Science. 2016.

[51] B. N. Popov, Corrosion Engineering: Principles and Solved Problems. 2015.

[52] S. Hiromoto and T. Hanawa, Corrosion of Implant Metals in the Presence of

Cells, Corros. Rev., vol. 24, no. 5–6, pp. 323–352, 2011.

[53] E. V. Parfenov, L. V. Parfenova, G. S. Dyakonov, K. V. Danilko, V. R. Mukaeva, R. G. Farrakhov, E. S. Lukina, and R. Z. Valiev, Surface functionalization via PEO coating and RGD peptide for nanostructured titanium implants and their in vitro assessment, Surf. Coatings Technol., vol. 357, no. October 2018, pp. 669–683, 2019.

[54] A. C. Alves, F. Wenger, P. Ponthiaux, J. P. Celis, A. M. Pinto, L. A. Rocha, and J. C. S. Fernandes, Corrosion mechanisms in titanium oxide-based films produced by anodic treatment, Electrochim. Acta, vol. 234, pp. 16–27, 2017.

[55] G. Denuault, Electrochimie Physique et Analytique, J. Electroanal. Chem., 2002.

[56] C. Boissy, Transport de matière au sein du film passif - Développement d'une méthodologie sélective corrélant le Point Defect Model et les modèles descriptifs, 2014.

[57] M. E. Orazem and B. Tribollett, Electrochemical Impedance Spectroscopy. 2008.

[58] A. Lasia, Electrochemical impedance spectroscopy and its applications, vol. 9781461489. 2014.

[59] Mark E. Orazem and B. Tribollett, Electrochemical Impedance Spectroscopy, in Agricultural and Food Electroanalysis, Second edi., 2015, pp. 381–419.

[60] P. Córdoba-Torres, N. T. C. Oliveira, C. Bolfarini, V. Roche, and R. P. Nogueira, Electrochemical impedance analysis of TiO_2 nanotube porous layers based on an alternative representation of impedance data, J. Electroanal. Chem., vol. 737, pp. 54–64, 2015.

[61] A. Garcia, J. A. Spim, and C. A. dos Santos, Ensaios dos materiais. 2000.

[62] A. F. Padilha, Materiais de engenharia, p. 349, 1997.

[63] P. P. Milella, Fatigue and Corrosion in Metals. 2013.

[64] M. Long and H. J. Rack, Titanium alloys in total joint replacement--a materials science perspective., Biomaterials, vol. 19, pp. 1621–1639, 1998.

[65] A. Heiskanen and J. Emnéus, Applications of Electrochemistry and Nanotechnology in Biology and Medicine I, vol. 52. 2011.

[66] L. Pazos, P. Corengia, and H. Svoboda, Effect of surface treatments on the fatigue life of titanium for biomedical applications, J. Mech. Behav. Biomed. Mater., vol. 3, no. 6, pp. 416–424, 2010.

[67] C. Leinenbach, B. Schwilling, and D. Eifler, Cyclic deformation behaviour and fatigue induced surface damage of titanium alloys in simulated physiological media, Mater. Sci. Eng. C, vol. 25, no. 3, pp. 321–329, 2005.

[68] C. Leinenbach and D. Eifler, Fatigue and cyclic deformation behaviour of surface-modified titanium alloys in simulated physiological media, Biomaterials, vol. 27, no. 8, pp. 1200–1208, 2006.

[69] I. Apachitei, B. Lonyuk, L. E. Fratila-Apachitei, J. Zhou, and J. Duszczyk, Fatigue response of porous coated titanium biomedical alloys, Scr. Mater., vol. 61, no. 2, pp. 113–116, 2009.

[70] P. S. C. P. da Silva, L. C. Campanelli, C. A. Escobar Claros, T. Ferreira, D. P. Oliveira, and C. Bolfarini, Prediction of the surface finishing roughness effect on the fatigue resistance of Ti-6Al-4V ELI for implants applications, Int. J. Fatigue, vol. 103, pp. 258–263, 2017.

[71] L. C. Campanelli, C. C. Bortolan, P. S. C. P. da Silva, C. Bolfarini, and N. T. C. Oliveira, Effect of an amorphous titania nanotubes coating on the fatigue and corrosion behaviors of the biomedical Ti-6Al-4V and Ti-6Al-7Nb alloys, J. Mech. Behav. Biomed. Mater., vol. 65, pp. 542–551, 2017.

[72] C. Fu, W. Tian, K. Yang, M. Yu, and J. Liu, Effects of sodium tartrate anodizing on fatigue life of TA15 titanium alloy, Chinese J. Aeronaut., vol. 28, no. 4, pp. 1281–1286, 2015.

[73] L. C. Campanelli, P. S. C. P. da Silva, A. M. Jorge, and C. Bolfarini, Effect of hydrogen on the fatigue behavior of the near-β Ti-5Al-5Mo-5V-3Cr alloy, Scr. Mater., vol. 132, pp. 39–43, 2017.

[74] ASTM, Standard Practice for Conducting Force Controlled Constant Amplitude Axial Fatigue Tests of Metallic Materials, Test, vol. 03, pp. 4–8, 2002.

[75] F. Hilario, V. Roche, A. M. Jorge, and R. P. Nogueira, Application of the transmission line model for porous electrodes to analyse the impedance response of TiO_2 nanotubes in physiological environment, Electrochim. Acta, vol. 253, pp. 599–608, 2017.

[76] T. Kokubo and H. Takadama, How useful is SBF in predicting in vivo bone bioactivity?, Biomaterials, vol. 27, no. 15, pp. 2907–2915, 2006.

[77] S. Fletcher*, The two-terminal equivalent network of a three-terminal electrochemical cell, Electrochim. Acta, vol. 55, no. 6, pp. 1907–1911, 2010.

[78] International Organization for Standardization, Metallic materials — Fatigue

testing — Statistical planning and analysis of data 12107:2003, 2003.

[79] H. Takadama, H. M. Kim, T. Kokubo, and T. Nakamura, TEM-EDX study of mechanism of bonelike apatite formation on bioactive titanium metal in simulated body fluid, J. Biomed. Mater. Res., vol. 57, no. 3, pp. 441–448, 2001.

[80] Zahid Amjad, Calcium phosphates in biological and industrial systems, p. 368, 1998.

[81] H. Tsuchiya, J. M. Macak, L. Mu, J. Kunze, F. Mu, and P. Greil, Hydroxyapatite growth on anodic TiO_2 nanotubes, pp. 23–25, 2006.

[82] S. Yamaguchi, H. Hashimoto, R. Nakai, and H. Takadama, Impact of surface potential on apatite formation in Ti alloys subjected to acid and heat treatments, Materials (Basel)., vol. 10, no. 10, 2017.

[83] R. J. Narayan, ASM Handbook, Volume 23 Materials for Medical Devices, 1 st., vol. 23. 2012.

[84] A. K. Shukla, R. Balasubramaniam, and S. Bhargava, Properties of passive film formed on CP titanium, Ti-6Al-4V and Ti-13.4Al-29Nb alloys in simulated human body conditions, Intermetallics, vol. 13, no. 6, pp. 631–637, 2005.

[85] E. Vasilescu, P. Drob, D. Raducanu, I. Cinca, D. Mareci, J. M. Calderon Moreno, M. Popa, C. Vasilescu, and J. C. Mirza Rosca, Effect of thermo-mechanical processing on the corrosion resistance of Ti6Al4V alloys in biofluids, Corros. Sci., vol. 51, no. 12, pp. 2885–2896, 2009.

[86] S. Tamilselvi, V. Raman, and N. Rajendran, Surface modification of titanium by chemical and thermal methods - Electrochemical impedance spectroscopic studies, Corros. Eng. Sci. Technol., vol. 46, no. 4, pp. 585–591, 2011.

[87] S. Y. Kim, Y. K. Kim, Y. S. Jang, I. S. Park, S. J. Lee, J. G. Jeon, and M. H. Lee, Bioactive effect of alkali-heat treated TiO_2 nanotubes by water or acid treatment, Surf. Coatings Technol., vol. 303, pp. 256–267, 2016.

[88] M. L. D. C. R. D. A. Carvalho, Corrosion of copper alloys in natural seawater – Effects of hydrodynamics and pH, UNIVERSITÉ PIERRE ET MARIE CURIE, 2014.

[89] V. Augustyn, P. Simon, and B. Dunn, Pseudocapacitive oxide materials for high-rate electrochemical energy storage, Energy Environ. Sci., vol. 7, no. 5, pp. 1597–1614, 2014.

[90] M. A. Macdonald and H. A. Andreas, Method for equivalent circuit determination for electrochemical impedance spectroscopy data of protein adsorption on solid surfaces, Electrochim. Acta, vol. 129, pp. 290–299, 2014.

[91] H. Luo, C. F. Dong, X. G. Li, and K. Xiao, The electrochemical behaviour of 2205 duplex stainless steel in alkaline solutions with different pH in the presence of chloride, Electrochim. Acta, vol. 64, pp. 211–220, 2012.

[92] N. Ebrahimi, M. Momeni, A. Kosari, M. Zakeri, and M. H. Moayed, A comparative study of critical pitting temperature (CPT) of stainless steels by electrochemical impedance spectroscopy (EIS), potentiodynamic and potentiostatic techniques, Corros. Sci., vol. 59, pp. 96–102, 2012.

[93] D. Q. Martins, W. R. Osório, M. E. P. Souza, R. Caram, and A. Garcia, Effects of Zr content on microstructure and corrosion resistance of Ti-30Nb-Zr casting alloys for biomedical applications, Electrochim. Acta, vol. 53, no. 6, pp. 2809–2817, 2008.

[94] M. E. Orazem, N. Páb̀re, and B. Tribollet, Enhanced graphical representation of electrochemical impedance data, J. Electrochem. Soc., vol. 153, no. 4, pp. 129–136, 2006.

[95] H. Liu, J. Yang, X. Zhao, Y. Sheng, W. Li, C. L. Chang, Q. Zhang, Z. Yu, and X. Wang, Microstructure, mechanical properties and corrosion behaviors of biomedical Ti-Zr-Mo-xMn alloys for dental application, Corros. Sci., vol. 161, no. May, pp. 2–15, 2019.

[96] S. L. De Assis, S. Wolynec, and I. Costa, Corrosion characterization of titanium alloys by electrochemical techniques, Electrochim. Acta, vol. 51, no. 8–9, pp. 1815–1819, 2006.

[97] A. Kocijan, D. K. Merl, and M. Jenko, The corrosion behaviour of austenitic and duplex stainless steels in artificial saliva with the addition of fluoride, Corros. Sci., vol. 53, no. 2, pp. 776–783, 2011.

[98] K. B. Devi, K. Singh, and N. Rajendran, Synthesis and characterization of nanoporous sodium-substituted hydrophilic titania ceramics coated on 316L SS for biomedical applications, J. Coatings Technol. Res., vol. 8, no. 5, pp. 595–604, 2011.

[99] S. Gudi, J. Radoševi, and M. Kliški, Study of passivation of Al and Al-Sn alloys in borate buffer solutions using electrochemical impedance spectroscopy, Electrochim. Acta, vol. 47, no. 18, pp. 3009–3016, 2002.

[100] A. W. E. Hodgson, Y. Mueller, D. Forster, and S. Virtanen, Electrochemical characterisation of passive films on Ti alloys under simulated biological conditions, Electrochim. Acta, vol. 47, no. 12, pp. 1913–1923, 2002.

[101] M. Cai and S. M. Park, Oxidation of zinc in alkaline solutions studied by electrochemical impedance spectroscopy, J. Electrochem. Soc., vol. 143, no.

12, pp. 3895–3902, 1996.

[102] T. Kokubo, F. Miyaji, H.-M. Kim, and T. Nakamura, Spontaneous Formation of Bonelike Apatite Layer on Chemically Treated Titanium Metals, J. Am. Ceram. Soc., vol. 79, pp. 1127–1129, 1996.

[103] H. M. Kim, F. Miyaji, T. Kokubo, and T. Nakamura, Preparation of bioactive Ti and its alloys via simple chemical surface treatment., J. Biomed. Mater. Res., vol. 32, pp. 409–417, 1996.

[104] L. Jonášová, F. a. Müller, A. Helebrant, J. Strnad, and P. Greil, Biomimetic apatite formation on chemically treated titanium, Biomaterials, vol. 25, pp. 1187–1194, 2004.

[105] S. Ban, Y. Iwaya, H. Kono, and H. Sato, Surface modification of titanium by etching in concentrated sulfuric acid, Dent. Mater., vol. 22, pp. 1115–1120, 2006.

[106] J. Bisquert, Influence of the boundaries in the impedance of porous film electrodes, 2000.

[107] M. Schlesinger, Modelling and Numerical Simulations II, vol. 44, no. 4. 2009.

[108] Diego Alfonso Godoy Pérez, Influence Of Surface Treatments on Corrosion Resistance Properties Of Ultrafine Grained Titanium Alloys For Biomedical applications, Universite Grenoble Alpes And Universidade Federal De São Carlos, 2019.

[109] L. Mohan, C. Anandan, and N. Rajendran, Electrochemical behavior and effect of heat treatment on morphology, crystalline structure of self-organized TiO_2 nanotube arrays on Ti–6Al–7Nb for biomedical applications, Mater. Sci. Eng. C, vol. 50, pp. 394–401, 2015.

[110] A. Mazare, M. Dilea, D. Ionita, and I. Demetrescu, Electrochemical behavior in simulated body fluid of TiO_2 nanotubes on TiAlNb alloy elaborated in various anodizing electrolyte, Surf. Interface Anal., vol. 46, no. 3, pp. 186–192, 2014.

[111] C. Liu, Y. Wang, M. Wang, W. Huang, and P. K. Chu, Electrochemical stability of TiO_2 nanotubes with different diameters in artificial saliva, Surf. Coatings Technol., vol. 206, no. 1, pp. 63–67, 2011.

[112] B. Munirathinam and L. Neelakantan, Titania nanotubes from weak organic acid electrolyte: Fabrication, characterization and oxide film properties, Mater. Sci. Eng. C, vol. 49, pp. 567–578, 2015.

[113] B. Munirathinam, H. Pydimukkala, N. Ramaswamy, and L. Neelakantan, Influence of crystallite size and surface morphology on electrochemical

properties of annealed TiO_2 nanotubes, Appl. Surf. Sci., vol. 355, pp. 1245–1253, 2015.

[114] L. V. Taveira, J. M. Macák, H. Tsuchiya, L. F. P. Dick, and P. Schmuki, Initiation and growth of self-organized TiO_2 nanotubes anodically formed in NH4F/(NH4)2SO4 electrolytes, J. Electrochem. Soc., vol. 152, no. 10, pp. 2–8, 2005.

[115] R. de Levie, On porous electrodes in electrolyte solutions*, Electrochim. Acta, vol. 9, no. 9, pp. 1231–1245, 1964.

[116] R. de Levie, On porous electrodes in electrolyte solutions-IV, Electrochim. Acta, vol. 9, no. 9, pp. 1231–1245, 1964.

[117] J. Bisquert, G. Garcia-Belmonte, F. Fabregat-Santiago, N. S. Ferriols, P. Bogdanoff, and E. C. Pereira, Doubling Exponent Models for the Analysis of Porous Film Electrodes by Impedance. Relaxation of TiO_2 Nanoporous in Aqueous Solution, J. Phys. Chem. B, vol. 104, no. 10, pp. 2287–2298, 2000.

[118] S. Gimenez, H. K. Dunn, P. Rodenas, F. Fabregat-Santiago, S. G. Miralles, E. M. Barea, R. Trevisan, A. Guerrero, and J. Bisquert, Carrier density and interfacial kinetics of mesoporous TiO2 in aqueous electrolyte determined by impedance spectroscopy, J. Electroanal. Chem., vol. 668, pp. 119–125, 2012.

[119] H. L. Yao, G. J. Yang, C. X. Li, and C. J. Li, Influence of TiO_2 film/substrate contact on photovoltaic performance and improved efficiency in dye-sensitized solar cells, J. Nanosci. Nanotechnol., vol. 16, no. 7, pp. 7395–7403, 2016.

[120] M. Mahbuburrahman, N. Chandradebnath, and J. J. Lee, Electrochemical Impedance Spectroscopic Analysis of Sensitization-Based Solar Cells, Isr. J. Chem., vol. 55, no. 9, pp. 990–1001, 2015.

[121] R. de Levie, Electrochemical Responses of Porous and Rough Electrodes,” in Advances in Electrochemistry and Electrochemical Engineering, vol. 6, pp. 329–397, 1967.

[122] P. Roy, S. Berger, and P. Schmuki, TiO_2 nanotubes: Synthesis and applications, Angew. Chemie - Int. Ed., vol. 50, no. 13, pp. 2904–2939, 2011.

[123] G. Garcia-Belmonte, J. Bisquert, E. C. Pereira, and F. Fabregat-Santiago, Switching behaviour in lightly doped polymeric porous film electrodes. Improving distributed impedance models for mixed conduction conditions, J. Electroanal. Chem., vol. 508, no. 1–2, pp. 48–58, 2001.

[124] G. Láng and K. E. Heusler, Remarks on the energetics of interfaces exhibiting constant phase element behaviour, J. Electroanal. Chem., vol. 457, no. 1–2,

pp. 257–260, 1998.

[125] T. Pajkossy, Impedance of rough capacitive electrodes, J. Electroanal. Chem., vol. 364, no. 1–2, pp. 111–125, 1994.

[126] C. Shuai, H. Sun, P. Wu, C. Gao, Y. Yang, W. Guo, D. Yang, F. Xu, P. Feng, and S. Peng, Biosilicate scaffolds for bone regeneration: Influence of introducing SrO, RSC Adv., vol. 7, no. 35, pp. 21749–21757, 2017.

[127] ASTM, Standard Practice for Conducting Force Controlled Constant Amplitude Axial Fatigue Tests of Metallic Materials - E466-15, Test, vol. 03, pp. 4–8, 2015.

[128] B. J. S. de Oliveira, L. C. Campanelli, D. P. Oliveira, A. P. de Bribean Guerra, and C. Bolfarini, Surface characterization and fatigue performance of a chemical-etched Ti-6Al-4V femoral stem for cementless hip arthroplasty, Surf. Coatings Technol., vol. 309, pp. 1126–1134, 2017.

[129] C. A. Escobar Claros, Estudo da resistência à fadiga da liga Ti-6Al-4V com superfície modificada por tratamento químico, Universidad de Sao carlos, 2016.

[130] V. Madina and I. Azkarate, Compatibility of materials with hydrogen. Particular case: Hydrogen embrittlement of titanium alloys, Int. J. Hydrogen Energy, vol. 34, no. 14, pp. 5976–5980, 2009.

[131] L. C. Campanelli, P. S. C. P. da Silva, A. M. Jorge, and C. Bolfarini, Effect of hydrogen on the fatigue behavior of the near-β Ti-5Al-5Mo-5V-3Cr alloy, Scr. Mater., vol. 132, pp. 39–43, 2017.

[132] ASM International. Handbook, ASM Handbook: Volume 12: Fractography, Met. Handb., vol. 2, p. 857, 1998.

[133] ASM, ASM Handbook Volume 12: Fractography, vol. 2. 1987.

[134] L. C. Campanelli, P. S. C. P. da Silva, and C. Bolfarini, High cycle fatigue and fracture behavior of Ti-5Al-5Mo-5V-3Cr alloy with BASCA and double aging treatments, Mater. Sci. Eng. A, vol. 658, pp. 203–209, 2016.

[135] Y. Chang, A. J. Breen, Z. Tarzimoghadam, P. Kürnsteiner, H. Gardner, A. Ackerman, A. Radecka, P. A. J. Bagot, W. Lu, T. Li, E. A. Jägle, M. Herbig, L. T. Stephenson, M. P. Moody, D. Rugg, D. Dye, D. Ponge, D. Raabe, and B. Gault, Characterizing solute hydrogen and hydrides in pure and alloyed titanium at the atomic scale, Acta Mater., vol. 150, pp. 273–280, 2018.

[136] P. D. Nezhadfar, A. S. Johnson, and N. Shamsaei, Fatigue Behavior and Microstructural Evolution of Additively Manufactured Inconel 718 under Cyclic

Loading at Elevated Temperature, Int. J. Fatigue, p. 105598, 2020.

[137] D. F. Teter, I. M. Robertson, and H. K. Birnbaum, The effects of hydrogen on the deformation and fracture of β-titanium, Acta Mater., vol. 49, no. 20, pp. 4313–4323, 2001.

[138] A. M. Alvarez, I. M. Robertson, and H. K. Birnbaum, Hydrogen embrittlement of a metastable β-titanium alloy, Acta Mater., vol. 52, no. 14, pp. 4161–4175, 2004.

[139] W. Barrows, R. Dingreville, and D. Spearot, Traction-separation relationships for hydrogen induced grain boundary embrittlement in nickel via molecular dynamics simulations, Mater. Sci. Eng. A, vol. 650, pp. 354–364, 2016.

[140] Y. Murakami, J. Yamabe, and H. Matsunaga, Microscopic mechanism of hydrogen embrittlement in fatigue and fracture, Key Eng. Mater., vol. 592–593, pp. 3–13, 2014.

[141] E. Tal-Gutelmacher and D. Eliezer, Hydrogen-assisted degradation of titanium based alloys, Mater. Trans., vol. 45, no. 5, pp. 1594–1600, 2004.

[142] J. Von Pezold, L. Lymperakis, and J. Neugebeauer, Hydrogen-enhanced local plasticity at dilute bulk H concentrations: The role of H-H interactions and the formation of local hydrides, Acta Mater., vol. 59, no. 8, pp. 2969–2980, 2011.

[143] P. J. Ferreira, I. M. Robertson, and H. K. Birnbaum, Hydrogen effects on the character of dislocations in high-purity aluminum, Acta Mater., vol. 47, no. 10, pp. 2991–2998, 1999.

[144] Y. Murakami, T. Kanezaki, Y. Mine, and S. Matsuoka, Hydrogen embrittlement mechanism in fatigue of austenitic stainless steels, Metall. Mater. Trans. A Phys. Metall. Mater. Sci., vol. 39 A, no. 6, pp. 1327–1339, 2008.